Attitude and Angular Momentum Control for Starlab

Aerodynamic Torque Modeling and $\mathcal{H}_\infty$ Control Design

Carolina Baltazar Mendes

TU Delft

Attitude and Angular Momentum Control for Starlab

Aerodynamic Torque Modeling and $\mathcal{H}_\infty$ Control Design

Thesis report

by

Carolina Baltazar Mendes

to obtain the degree of Master of Science
at the Delft University of Technology
to be defended publicly on December 1, 2025 at 10:00

Thesis committee:

Chair:	Dr.ir. E. Smeur
Supervisors:	Dr.ir. E. van Kampen
	Dr.-Ing. R. Geshnizjani
External examiner:	Dr.ir. D. Dirkx
Place:	Faculty of Aerospace Engineering, Delft
Project Duration:	March, 2025 - December, 2025
Student number:	5957044

An electronic version of this thesis is available at `https://repository.tudelft.nl`.

Faculty of Aerospace Engineering · Delft University of Technology

Preface

It still feels a bit surreal to say that I got to work on a space station for my master's thesis. I know that's not something many students get to say, and I'm incredibly grateful for it. What made it even more special was that the project itself was evolving at the same time as I was — both of us figuring things out as we went.

My journey at Airbus actually started before this thesis, during my internship. I want to thank Alejandro Menendez and Sergi Lopez for opening the doors to Airbus, for making me feel like I belonged from the very beginning, and for still keeping in touch and being part of my life. That first experience made it clear to me that this was the environment where I wanted to continue growing — and it eventually led me to Starlab.

First of all, I want to thank Federico Passarin and Ramin Geshnizjani for giving me the opportunity to work on this project in the first place. I owe a special thanks to Ramin, my daily supervisor, who spent countless hours guiding me and, above all, challenging me. His technical knowledge and dedication made a huge difference throughout this thesis. Now that he is moving on to become a professor, I feel lucky to have been one of his "prototype" students — and I'm sure his future students will be just as lucky.

From TU Delft, I was lucky to have Professor Erik-Jan van Kampen as my supervisor. He trusted both me and the project from day one and gave me full freedom to explore, while also providing guidance every step of the way. That balance of independence and support was more than I could have hoped for.

Then there is the whole Starlab team and the AOCS department at Airbus — thank you all for welcoming me and accompanying me throughout these seven months. Any small contribution I managed to make to the project makes me genuinely happy.

I also owe a lot to my friends — both from university and the ones I made at Airbus — for making over two years away from home go by so fast. And finally, to my family and Sérgio [1]: thank you for sitting through the countless video calls, rants, and random space-related monologues. You made the distance feel a lot smaller.

Carolina Baltazar Mendes
Delft, November 2025

[1] (and Guilherme)

Contents

List of Figures

Nomenclature

Abbreviations

ACMM	Attitude Control and Momentum Management
ADRC	Active Disturbance Rejection Control
ANN	Artificial Neural Network
CMG	Control Moment Gyroscope
ECI	Earth-Centered Inertial
EKF	Extended Kalman Filter
ESO	Extended State Observer
ISS	International Space Station
LEO	Low Earth Orbit
LESO	Linear Extended State Observer
LQR	Linear Quadratic Regulator
LS	Least Squares
LTAN	Local Time at Ascending Node
LVLH	Local Vertical Local Horizontal
MED	Momentum Exchange Device
MIMO	Multiple-Input Multiple-Output
RAAN	Right Ascension of the Ascending Node
RLS	Recursive Least Squares
SDRE	State-Dependent Riccati Equation
TEA	Torque Equilibrium Attitude

Symbols

$[(\cdot)\times]$	skew symmetric matrix of the vector $(\cdot)$

Greek Letters

ω_0	Orbital rate	[rad/s]
ϕ	Roll angle	[rad]
ψ	Yaw angle	[rad]
τ	Torque	[N.m]

θ	Pitch angle	[rad]
$\varphi_{X/Y}$	Attitude vector defined from frame Y to frame X	[rad]
${}_Z\omega_{X/Y}$	Angular rate of frame X with respect to frame Y, in frame Z	[rad/s]

Latin Letters

F	Force	[N]
H	Angular momentum	[N.m.s]
I	3-by-3 identity matrix	[-]
J	Moment of inertia of the spacecraft	[kg.m^2]
$T_{X/Y}$	Direction cosine matrix from frame Y to frame X	[-]

Subscripts and Superscripts

$*$	Linerization operating point
a	Aerodynamic
B	Body frame
c	Control
d	Disturbance
g	Gravity gradient
I	Inertial reference frame
N	Local vertical local horizontal (LVLH) frame

1

Introduction

As one of the most ambitious projects in the space industry, space stations are essential platforms for long-term scientific research, technology development, and deep space mission preparation. The first space station, Salyut 1, launched by the Soviet Union in 1971, demonstrated the feasibility of long-duration crewed missions in Low Earth Orbit (LEO) [1]. Skylab, launched by NASA in 1973, introduced larger pressurized modules and advanced life-support systems, allowing for longer stays and extensive onboard experimentation [2]. Mir, operated by the Soviet Union and later Russia from 1986 to 2001, implemented a modular architecture, which allowed for progressive in-orbit assembly and expansion of the station [3]. International Space Station (ISS), inhabited since 2000, was built upon these achievements and has enabled a continuous human presence in LEO for more than two decades, underscoring the importance of international collaboration for continuous growth and evolution of the aerospace field [4]. With the scheduled decommissioning of the ISS by 2030, Starlab has emerged as a US-led project, jointly with Airbus Defence and Space, which aims to succeed ISS in providing long-term access to orbital experimentation [5].

Space stations such as Starlab are characterized by their large size, modular configuration, and continuous operation, which impose different constraints on their attitude control systems. Maintaining precise attitude pointing is essential for thermal management, communications, docking, and scientific payloads. The actuators typically used for attitude control – Control Moment Gyroscopes (CMGs) – generate torques by redistributing angular momentum within the spacecraft. However, because the spacecraft is subjected to persistent environmental torques the total stored angular momentum in the CMGs accumulates over time. If the stored momentum increases beyond operational limits, the system can no longer generate sufficient control torque, leading to actuator saturation and loss of control authority.

This interaction between attitude dynamics and actuator momentum defines the Attitude Control and Momentum Management (ACMM) problem. In space station operations, ACMM is inherently coupled due to the strong influence of environmental torques. The large inertia and extensive surface area of the space station make it more susceptible to high-magnitude environmental disturbances, which continuously increase the stored angular momentum of the CMGs. To mitigate this effect, attitude is intentionally offset such that the total contribution of the external torques is reduced, preventing actuator saturation. In this way, ACMM is addressed by achieving an acceptable trade-off between attitude tracking accuracy and the deviation of the CMG angular momentum from its nominal (zero-momentum) value, while ensuring compliance with the storage limits.

To better define the problem at hand, it is essential to identify and characterize the disturbances acting on the system. As depicted in Figure 1.1, for LEO, at an altitude of 400 km, the most preponderant environmental disturbances are the aerodynamic drag – resulting from the interaction between the space station and Earth's atmosphere– and the gravity gradient gradient torque – arising from the differential gravitational pull along the spacecraft's structure [6].

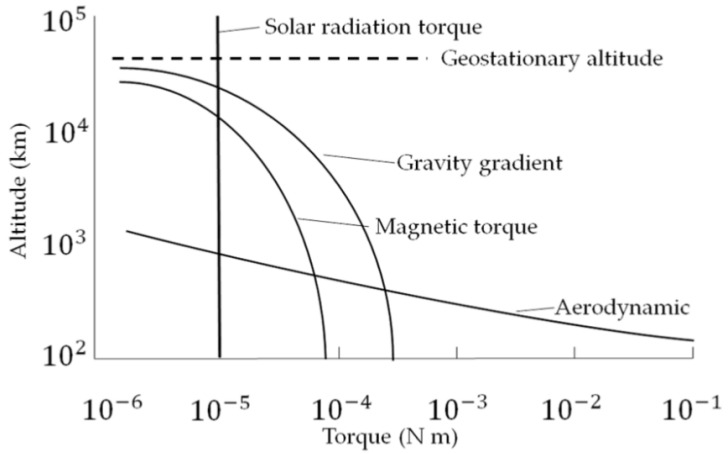

Figure 1.1: External environmental torques as a function of altitude [7]

To understand the impact of these environmental torques on Starlab, it is necessary to consider the individual contributions of its structural and functional components (Figure 1.2) to the overall system disturbances and uncertainties [8]:

Habitat, Laboratory and Service Module This module corresponds to the astronauts' living quarters, research facilities and propulsion segment. Its large cross section area – with a diameter of approximately 8 meters – interacts with the atmosphere causing high-magnitude drag disturbances to act on the spacecraft.

Docking Node The docking node facilitates the attachment of potential additional modules. These modules alter the space station configuration in terms of inertia, mass distribution, and area, altering both gravity gradient and aerodynamic torque contributions.

Robotic Arm Similarly to the Canadarm from the ISS, the robotic arm is responsible for servicing cargo, and providing maintenance assistance. Its movement causes a shift in the mass distribution of the space station therefore introducing inertia uncertainties in the overall system.

Solar Arrays and Thermal Radiators These structures extend from the main body, ensuring power generation and thermal control, respectively. These appendages introduce flexible structural modes that can interact with the control system. Additionally, the solar arrays track the Sun to maximize energy retrieval, introducing harmonic frequencies of the orbital rate in the aerodynamic torque due to area and inertia variations.

Figure 1.2: Starlab [9]

In addition to the spacecraft's configuration and structure, there are several specific constraints imposed in the ACMM problem arising from the characteristics of Starlab's nominal operational mode. In this configuration, it is assumed that the space station follows an approximately circular orbit at an altitude of 400 km and that it should deviate as little as possible from nadir-pointing. In other words, the body

frame should ideally be aligned with the Local Vertical Local Horizontal (LVLH) reference frame, such that all nominal operations, such as communication with ground stations, is ensured throughout the entirety of this mode. Therefore, the nominal mode excludes aggressive maneuvers such as reconfiguration, large slews, or docking operations, and attitude control is exclusively performed through momentum exchange devices. The long-duration nature of this mode and the fact that it is performed in LEO amplify the effects of persistent environmental torques on momentum accumulation. In this context, external torques are mostly predictable in nature. However, potential inertia variations namely due to internal motion emphasize the need for robust control strategies, that are able to maintain precise attitude tracking while preventing saturation of the available actuators.

1.1. Research Objectives & Questions

ACMM has been extensively studied and a wide range of techniques have been successfully applied in missions such as the ISS. These solutions have demonstrated that the ACMM must be treated as a coupled problem, due to the large magnitudes of the environmental torques that act on large spacecraft in LEO. Nevertheless, further refinement of the environmental disturbance modeling remains essential to improve control design in the context of space stations.

Among the environmental torques, the aerodynamic torque is the most complex and least accurately represented in literature. Unlike the gravity gradient torque, which can be described analytically from mechanics, the aerodynamic torque cannot be captured as easily, as it depends on complex interactions involving the spacecraft geometry, attitude, and atmospheric conditions. In previous studies, this contribution has been defined based on the same simplified assumptions on the torque's profile as stated by Wie et al. in [10]. In fact, most research work often omit the attitude-dependent component of the aerodynamic torque from the system dynamics used in control synthesis. In order to optimize the trade-off between attitude and momentum error minimization, it is essential to include this information for control design. This simplification further increases the mismatch between the physical environment experienced by the spacecraft and the mathematical model used for controller synthesis. Consequently, the robustness of the designed controller may be overestimated.

To address this gap, this thesis focuses on two main aspects: the development of an aerodynamic torque model that captures its dependency on the spacecraft's attitude, enabling its use in control design, and the selection and implementation of a control strategy suitable for Starlab's operational constraints. The control method must balance three main requirements – disturbance rejection, robustness to model uncertainties, and real-time computational feasibility – while ensuring efficient momentum management and minimal use of thrusters during nominal operations.

Based on these considerations, the research objectives of this work are defined as follows:

Research Objective 1

To characterize the dominant environmental disturbances – gravity gradient and aerodynamic torque – such that they can be integrated into the framework for controller synthesis.

Research Objective 2

To design and implement a robust control strategy for spacecraft attitude control and momentum management (ACMM) in the context of the Starlab space station's nominal mode.

Research Objective 3

To evaluate the robustness, performance, and limitations of the proposed control strategy using a high-fidelity Starlab simulator.

After defining the research objectives, the following research questions can be defined:

Research Question 1

How can the mission requirements for Starlab together with the physical constraints of the ACMM problem be translated into concrete control-design requirements?

1.1 What are the primary control objectives and how are they prioritized?
1.2 Which measurable performance metrics represent those objectives?
1.3 How can the spacecraft's physical constraints be represented in the control design?
1.4 How should environmental disturbances be characterized for robust control design?
1.5 Which control architecture best incorporates these requirements and constraints?

Research Question 2

How do modeling assumptions affect the fidelity and validity of the spacecraft model used for control design?

2.1 What are the main simplifying assumptions adopted to formulate a model of the spacecraft for control design?
2.2 How do these assumptions influence the accuracy and applicability of the model in nominal conditions?
2.3 Within which operational boundaries does the model remain valid for control design?

Research Question 3

How can the robustness and performance of the synthesized control system be validated across different configurations, orbital conditions, and environmental variations?

3.1 How can the controller's performance be evaluated under nominal conditions?
3.2 How can the controller's performance be validated across different orbital conditions?
3.3 How can the overall robustness envelope established and verified?

The research objectives and questions are refined in Chapter 4 following an extensive literature review. This review helps clarify the scope and direction of the study through a trade-off analysis of existing state-of-the-art solutions.

1.2. Thesis outline

The structure of the report is organized as follows. The first part of the thesis is dedicated to the definition of the research problem, and a comprehensive literature review. Firstly, Chapter 2 introduces the fundamentals of the ACMM problem. It defines the most relevant reference frames, attitude representation, the equations of motion of the spacecraft, the dominant environmental disturbances in LEO, and the CMG dynamics. Secondly, Chapter 3 includes a detailed description of the state-of-the-art solutions for the ACMM problem, by categorizing them into different groups of control approaches, and identifying their main advantages and limitations. In Chapter 4, the research gap, objectives, questions and planning of the thesis project are discussed. The following chapter (Chapter 5) presents the linearized formulation of the equations of motion, which serves as the basis for control synthesis. This is followed by Chapter 6, where the fundamentals of the chosen control design framework are presented. The second part of the report is allocated to the Scientific Article, which stands as the core of the thesis, and presents the main research developments, methodology and results of the conducted work. The third part includes additional results that complement the main analysis, particularly the identification and validation of an aerodynamic torque model that captures both attitude and solar array angle dependencies. The fourth and final part of the report comprises the concluding remarks of the project. In Chapter 8 the previously defined research

questions are revisited and answered, and the implications of the obtained results and conclusions for Starlab and other space stations are discussed. Finally, Chapter 9 provides a set of recommendations for future work based on the findings of this thesis.

Part I

Research Definition & Literature Review

2

Definition of the ACMM Problem

This chapter presents the mathematical formulation of the ACMM problem for a spacecraft operating in LEO. The objective is to establish the fundamental equations that describe the dynamics and kinematics of the space station, which serve as foundation for subsequent control design. This being the case, firstly, all relevant reference frames are defined in Section 2.1 from which attitude is defined in Section 2.2. After this, it is possible to derive the kinematics (Section 2.3) and dynamics equations (Section 2.4) that define the system to be controlled. Finally, in Section 2.5, the two main disturbance torques – gravity gradient and aerodynamic torques – acting on a LEO spacecraft are modeled.

2.1. Reference Frames

In order to derive Starlab's equations of motion, it is necessary to define reference frames. The choice of these reference frames directly influences the mathematical derivation of the spacecraft's dynamics and kinematics equations. Therefore, it is extremely important that the reference frames are consistent with the control objectives and the environmental interactions of the spacecraft.

This being the case, the following reference frames can be defined:

Earth-Centered Inertial (ECI) frame (Figure 2.1) This reference frame has its origin at the center of the Earth and does not rotate with the planet. Its Z_{ECI} axis is located along the Earth's spin axis, pointing to the North, while X_{ECI} points toward the first point of Aries. Lastly, Y_{ECI} is defined such that the right-hand reference frame is completed. In this frame, all Newtonian laws of motion are valid.

Local Vertical Local Horizontal (LVLH) frame (Figure 2.1, Figure 2.2) The LVLH frame has its origin at the center of mass of the spacecraft and therefore follows its movement along the orbit. Its three axes are defined along the orbit direction (x_{LVLH}), perpendicularly to the orbit plane (y_{LVLH}), and towards the center of the Earth (z_{LVLH}).

Body frame (Figure 2.2) The origin of this reference frame is located in the center of mass of the spacecraft. Its x_B axis points towards the front of the spacecraft, y_B points towards the right side of the spacecraft, and z_B is defined such that the right-hand frame is completed. As mentioned in the following section, the attitude of the spacecraft can be defined by the difference in orientation of this frame and the LVLH frame. In its normal operation mode, the space station's body frame should be aligned with the LVLH frame.

Principal axes of inertia frame This reference frame is centered at the spacecraft's center of mass with its axes aligned along the principal directions of the spacecraft's inertia tensor. In this frame, the inertia tensor is diagonal, and aligning its axes with the LVLH frame – placing the largest moment of inertia along the local vertical – minimizes the gravity gradient torque.

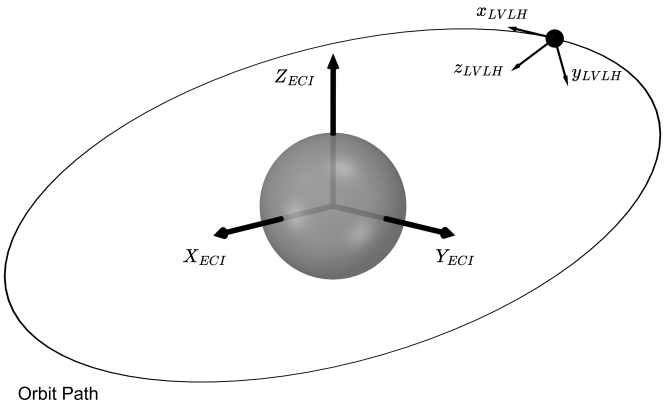

Figure 2.1: ECI and LVLH reference frame representation

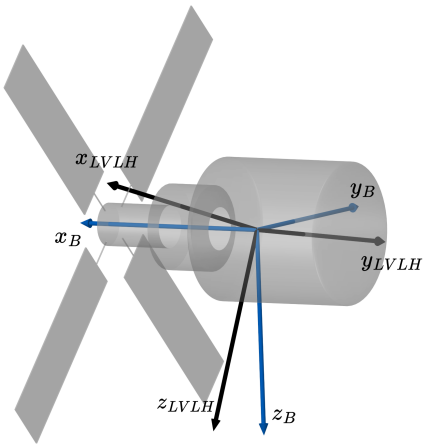

Figure 2.2: Body and LVLH reference frame representation

2.2. Attitude Representation – Euler Angles

After carefully defining the relevant reference frames, attitude can be represented in different ways [10]. This section delves into the Euler angle attitude definition. In this representation, three Euler angles – roll(ϕ), pitch (θ), and yaw (ψ) – can be defined by the difference in orientation of the spacecraft in the body and LVLH reference frames. These angles are defined by sequential rotations between the previous reference frame and the new reference frame, resulting from the rotation. This being the case, it is crucial to establish an order of rotation, since changing this sequence will result in different Euler angle definitions. In this project, a roll-pitch-yaw (1-2-3) rotation was considered, starting from the original reference frame N – the LVLH frame – and ending with the final reference frame B – the Body frame. These rotations ($N \rightarrow N' \rightarrow N'' \rightarrow B$) can be defined as follows:

$$\begin{bmatrix} b_1 \\ b_2 \\ b_3 \end{bmatrix} = T_{B/N''}(\psi) \begin{bmatrix} n_1'' \\ n_2'' \\ n_3'' \end{bmatrix} = T_{B/N''}(\psi) T_{N''/N'}(\theta) \begin{bmatrix} n_1' \\ n_2' \\ n_3' \end{bmatrix} = T_{B/N''}(\psi) T_{N''/N'}(\theta) T_{N'/N}(\phi) \begin{bmatrix} n_1 \\ n_2 \\ n_3 \end{bmatrix} \tag{2.1}$$

$$T_{N'/N}(\phi) = \begin{bmatrix} 1 & 0 & 0 \\ 0 & \cos(\phi) & \sin(\phi) \\ 0 & -\sin(\phi) & \cos(\phi) \end{bmatrix} \tag{2.2}$$

$$T_{N''/N'}(\theta) = \begin{bmatrix} \cos(\theta) & 0 & -\sin(\theta) \\ 0 & 1 & 0 \\ \sin(\theta) & 0 & \cos(\theta) \end{bmatrix} \tag{2.3}$$

$$T_{B/N''}(\psi) = \begin{bmatrix} \cos(\psi) & \sin(\psi) & 0 \\ -\sin(\psi) & \cos(\psi) & 0 \\ 0 & 0 & 1 \end{bmatrix} \tag{2.4}$$

where b_i corresponds to a unit basis vector of the body frame, n_i corresponds to a unit basis vector of the LVLH frame, and N' and N'' are the two intermediary frames that result from the successive rotations.

Thus, the final direction cosine matrix corresponds to:

$$\begin{aligned} T_{B/N} = T_{B/N''}(\psi)T_{N''/N'}(\theta)T_{N'/N}(\phi) &= \begin{bmatrix} T_{1,1} & T_{1,2} & T_{1,3} \\ T_{2,1} & T_{2,2} & T_{2,3} \\ T_{3,1} & T_{3,2} & T_{3,3} \end{bmatrix} \\ &= \begin{bmatrix} \cos\psi\cos\theta & \cos\phi\sin\psi + \cos\psi\sin\phi\sin\theta & \sin\phi\sin\psi - \cos\phi\cos\psi\sin\theta \\ -\cos\theta\sin\psi & \cos\phi\cos\psi - \sin\phi\sin\psi\sin\theta & \cos\psi\sin\phi + \cos\phi\sin\psi\sin\theta \\ \sin\theta & -\cos\theta\sin\phi & \cos\phi\cos\theta \end{bmatrix} \end{aligned} \tag{2.5}$$

Although Euler angles are one of the most intuitive attitude representation, this definition has some disadvantages. Firstly, it has expensive transformation matrices due to the trigonometric functions, as can be seen in the previously presented equations. Besides this, ϕ and ψ are interchangeable at $\theta = 90^\circ$, and there are numerical precision complications around $\theta = 90^\circ$. During nominal operations, the spacecraft attitude is expected to remain close to its reference orientation. In such case, attitudes for which these singularities arise are avoided. For this reason, this attitude representation is appropriate for ACMM control design.

2.3. Formulation of the Kinematic Equations

In this section, the kinematic equations are derived from the chosen attitude definition [10]. These equations describe the relationship between the variation over time of the attitude parameters as a function of these same parameters as well as the angular velocity.

Firstly, the angular velocity of the Body frame (B) with respect to the Inertial frame (I) is given by the sum of the angular velocity of the Body frame (B) with respect to the LVLH frame (N) and the angular velocity of the LVLH frame (N) with respect to the Inertial frame (I):

$$ {}_B\omega_{B/I} = {}_B\omega_{B/N} + {}_B\omega_{N/I} \tag{2.6}$$

where all angular rates are expressed in the Body frame (B), as indicated by the pre-subscript notation.

The angular velocity of the Body frame (B) with respect to the LVLH frame (N) can be computed by taking the time derivative of the direction cosine matrix, $T_{B/N}$:

$$\dot{T}_{B/N} + \left[{}_B\omega_{B/N}\times\right] \cdot T_{B/N} = 0 \implies \left[{}_B\omega_{B/N}\times\right] = -\dot{T}_{B/N} \cdot T_{B/N}^T \tag{2.7}$$

This being considered, ${}_B\omega_{B/N}$ is given by:

$$ {}_B\omega_{B/N} = \begin{bmatrix} \dot{T}_{2,1}\cdot T_{3,1} + \dot{T}_{2,2}\cdot T_{3,2} + \dot{T}_{2,3}\cdot T_{3,3} \\ \dot{T}_{3,1}\cdot T_{1,1} + \dot{T}_{3,2}\cdot T_{1,2} + \dot{T}_{3,3}\cdot T_{1,3} \\ \dot{T}_{1,1}\cdot T_{2,1} + \dot{T}_{1,2}\cdot T_{2,2} + \dot{T}_{1,3}\cdot T_{2,3} \end{bmatrix} \tag{2.8}$$

Subsequently, considering that the spacecraft follows a circular orbit around Earth, the angular velocity of the LVLH frame (N) with respect to the inertial frame (I) is given by a rotation around the y axis of the LVLH frame:

$$ {}_N\omega_{N/I} = -\omega_0 \cdot \begin{bmatrix} 0 \\ 1 \\ 0 \end{bmatrix} \implies {}_B\omega_{N/I} = T_{B/N} \cdot {}_N\omega_{N/I} = -\omega_0 \cdot \begin{bmatrix} T_{1,2} \\ T_{2,2} \\ T_{3,2} \end{bmatrix} \tag{2.9}$$

where ω_0 is the constant orbital rate.

After defining each component of the angular velocity of the body frame with respect to the inertial frame, the final kinematics expression can be derived by substituting Equations (2.8) and (2.9) into Equation (2.6) and solving the latter with respect to the derivative of the Euler angles:

$$\dot{\varphi}_{B/N} = \begin{bmatrix} \frac{\cos\psi}{\cos\theta} & -\frac{\sin\psi}{\cos\theta} & 0 \\ \sin\psi & \cos\psi & 0 \\ -\cos\psi\tan\theta & \sin\psi\tan\theta & 1 \end{bmatrix} {}_B\omega_{B/I} + \omega_0 \begin{bmatrix} \sin\phi\tan\theta \\ \cos\phi \\ -\frac{\sin\phi}{\cos\theta} \end{bmatrix} \tag{2.10}$$

in which $\varphi_{B/N} = \begin{bmatrix} \phi & \theta & \psi \end{bmatrix}^T$.

2.4. Formulation of the Rigid-Body Dynamic Equations

In this section, the dynamic equations are derived from the principle of conservation of the angular momentum. Considering a rigid body that is rotating with respect to an inertial frame (I) with an angular velocity ${}_B\omega$, the rotational equation about an arbitrary point is given by:

$$\int r \times \ddot{R}\, dm = \tau \tag{2.11}$$

where r is the vector between the origin of the rotating reference frame and the infinitesimal mass element dm, R is the vector between the origin of the inertial reference frame and the infinitesimal mass element dm, and τ is the total torque around the origin of the rotating reference frame (Figure 2.3).

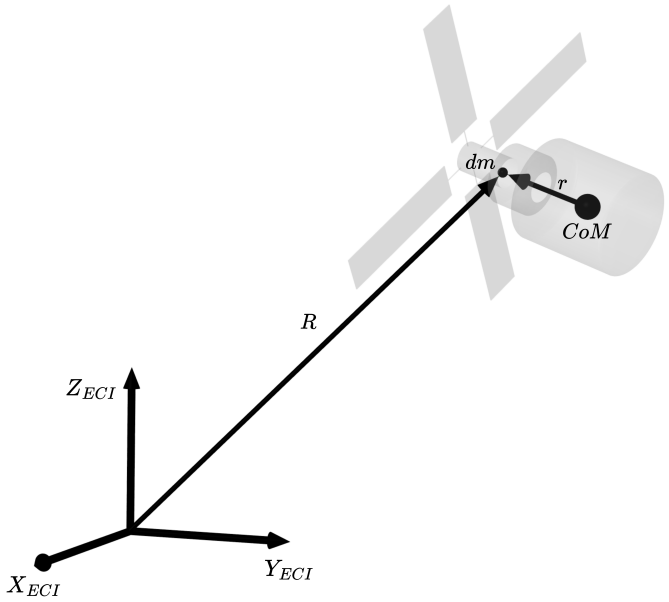

Figure 2.3: Spacecraft motion relative to the ECI reference frame

On the other hand, the absolute angular momentum about the origin of the rotating frame is given by:

$$H = \int r \times \dot{R}\, dm \tag{2.12}$$

If the reference point about which the torque, τ, and the angular momentum, H, is defined as the center of mass of the rigid body, then:

$${}_I\dot{H} = \tau \tag{2.13}$$

Keeping the same assumption in mind and expressing all variables in the body frame, the expression of the angular momentum of a rigid body about its center of mass can further be expanded (Equation (2.14)).

$$ {}_{B}H = \int r \times \dot{R}\, dm = \int r \times {}_{B}\omega \times r\, dm = {}_{B}J \cdot {}_{B}\omega \tag{2.14} $$

where ${}_{B}J$ is the symmetric inertia matrix:

$$ {}_{B}J = \begin{bmatrix} \int (r_y^2 + r_z^2)\, dm & -\int r_x \cdot r_y\, dm & -\int r_x \cdot r_z\, dm \\ -\int r_x \cdot r_y\, dm & \int (r_x^2 + r_z^2)\, dm & -\int r_y \cdot r_z\, dm \\ -\int r_x \cdot r_z\, dm & -\int r_y \cdot r_z\, dm & \int (r_x^2 + r_y^2)\, dm \end{bmatrix} \tag{2.15} $$

From the transport theorem, the final rotation equation of motion can be transformed into the Body frame:

$$ {}_{I}\dot{H} \xrightarrow{\text{Transport theorem}} {}_{B}\dot{H} + {}_{B}\omega_{B/I} \times {}_{B}H = {}_{B}\tau \tag{2.16} $$

where ${}_{B}H = {}_{B}J \cdot {}_{B}\omega_{B/I}$.

Finally, rewriting the previous equation (Equation (2.16)) expressed in the Body frame with respect to ${}_{B}\omega_{B/I}$ yields the following expression:

$$ {}_{B}\dot{\omega}_{B/I} = -[{}_{B}J]^{-1}[{}_{B}\omega_{B/I}\times] \cdot {}_{B}J \cdot {}_{B}\omega_{B/I} + [{}_{B}J]^{-1}{}_{B}\tau \tag{2.17} $$

where ${}_{B}\tau$ corresponds to the sum of the external torques acting on the spacecraft – control torque, ${}_{B}\tau_c$, gravity gradient torque, ${}_{B}\tau_g$, and the aerodynamic torque ${}_{B}\tau_a$.

2.5. LEO Disturbance Modeling

As mentioned in Chapter 1, in LEO, the most significant sources of external torque are the gravity gradient torque and the aerodynamic torque. In this section, the mathematical models for the these two environmental torques are presented [10].

2.5.1. Gravity Gradient Torque

The gravity gradient torque about a spacecraft's center of mass can be defined as:

$$ \tau_g = \int r \times dF_g \tag{2.18} $$

where dF_g corresponds to the gravitational force acting on an infinitesimal mass element dm and is given by the following expression:

$$ dF_g = -\mu \frac{R}{\|R\|^3}\, dm = -\mu \frac{R_{Earth} + r}{\|R_{Earth} + r\|^3}\, dm \tag{2.19} $$

Since the distance from the spacecraft's to Earth's center of mass, R_{Earth}, is much greater than the distance between the infinitesimal mass element and the center of mass of the spacecraft, r, and taking the first order term of the binomial expansion, the following approximation can be made:

$$ \|R_{Earth} + r\|^{-3} \approx \|R_{Earth}\|^{-3} \left[1 - \frac{3 \cdot (R_{Earth} \cdot r)}{\|R_{Earth}\|^2}\right] \tag{2.20} $$

Considering the previous approximation and that the spacecraft follows a circular orbit, the final gravity gradient torque is given by:

$$ \tau_g = 3\omega_0^2 n \times J \cdot n \tag{2.21} $$

in which $\omega_0 = \frac{\mu}{\|R_{Earth}\|^3}$ is the orbital rate, and n corresponds to a unit Nadir pointing vector. Therefore, in the LVLH reference frame, the gravity gradient torque can be expressed as:

$$ {}_B\tau_g = 3\omega_0^2 \begin{bmatrix} 0 & -T_{3,3} & T_{2,3} \\ T_{3,3} & 0 & -T_{1,3} \\ -T_{2,3} & T_{1,3} & 0 \end{bmatrix} \cdot {}_BJ \cdot \begin{bmatrix} T_{1,3} \\ T_{2,3} \\ T_{3,3} \end{bmatrix} \tag{2.22} $$

2.5.2. Aerodynamic Torque

In LEO, the remaining atmosphere brings about non-negligible forces and torques to act on the space station. For a spacecraft surface element dA, the atmospheric force can be defined as:

$$ dF_a = -\frac{1}{2}\rho V V^T n C_D \, dA \tag{2.23} $$

where V is the flight velocity of the spacecraft with respect to the atmosphere, ρ is the density of the atmosphere, n is the surface's normal vector, and C_D is the drag coefficient. Integrating this expression over the total area, A, yields the following result:

$$ F_a = -\frac{1}{2}\rho V V^T n C_D A \tag{2.24} $$

From Equation (2.24), it is possible to observe that the magnitude of the aerodynamic force is proportional to the projected surface area of the spacecraft, A, in the direction of the velocity vector, V.

Finally, the aerodynamic torque expression can be derived as the cross product between the vector defined between the aerodynamic center of pressure and the center of mass of the spacecraft, r_{CoP}, and the aerodynamic force, F_a:

$$ \tau_a = r_{CoP} \times F_a \tag{2.25} $$

2.6. CMG Dynamics

For actuation, Control Moment Gyroscopes are considered. Their dynamics can be defined as follows:

$$ {}_B\dot{H}_c = -[{}_B\omega_{B/I}\times] \cdot {}_BH_c - {}_B\tau_c \tag{2.26} $$

where ${}_BH_c$ corresponds to the angular momentum of the CMGs.

3

State-of-the-art ACMM Approaches

In this chapter, an in-depth review of the state-of-the-art solutions for the ACMM problem is presented. These strategies are critically analyzed, and their respective advantages and limitations are discussed in terms of their applicability to Starlab, in order to motivate the selection of the control strategy to be implemented for Starlab's ACMM.

To date, ACMM research has primarily focused on five categories: classical linear control strategies, robust control methods, adaptive techniques, observer-based and disturbance estimation strategies, and learning-based controllers. The current section discusses several concrete contributions from each of these categories.

3.1. Classical Linear Control Strategies

Early approaches to the ACMM problem consisted of classical linear control strategies, which typically rely on the use and derivation of linearized spacecraft models. In most cases, small-angle approximations are assumed and fixed control gains are designed around nominal operating points, using well-established state-space techniques such as Linear Quadratic Regulator (LQR). One of the main benefits of these strategies is their simplicity in implementation.

In 1988, Woo et al. [11] proposed a periodic and continuous momentum management method for ACMM for a dual-keel space station, assuming decoupled pitch and roll/yaw dynamics. While the periodic momentum management updates the Torque Equilibrium Attitude (TEA) once per orbit to balance external torques (Figure 3.1), the continuous momentum management integrates momentum control with attitude control (Figure 3.2). In the periodic strategy, the gains are computed based on momentum derivatives, whereas in the continuous method an LQR is used. Stability and robustness were further investigated by analyzing the resulting system in the frequency domain using singular-value response methods. In the end, it was concluded that the continuous method outperformed the periodic method, since it provided better overall performance in attitude tracking and momentum accumulation, as well as robustness to disturbances and system uncertainties.

In 1992, Harduvel [12] developed a frequency-weighted LQR control method for continuous momentum management for a three-axes coupled Earth-oriented spacecraft by using environmental torques as the main actuation source. By including disturbance rejection filter states tuned to harmonics of the orbital frequency, it becomes possible to suppress combinations of attitude and momentum components by frequency and axis. Additionally, the conditions for the existence of a dynamic TEA – attitude motion which requires null control torque – are defined. This operating mode ensures zero steady-state momentum error under specified conditions. Overall the architecture of the proposed strategy allows the designer to select the attitude and momentum states for which to suppress the effects of the considered disturbance. Results showed that both attitude and angular momentum errors were kept within adequate bounds.

Dang et al. [13] proposed a multistage angular momentum framework in 2018. Similarly to the continuous approach presented by Woo et al., the proposed strategy combines TEA-based attitude maneuvers and closed-loop angular momentum feedback. This method switches between an open-loop TEA tracking phase, executed through pre-planned large-angle maneuvers, and a feedback stabilization phase using an LQR controller. For control design, the same three-axes coupled linearized model as the one proposed by Harduvel [12] was considered.

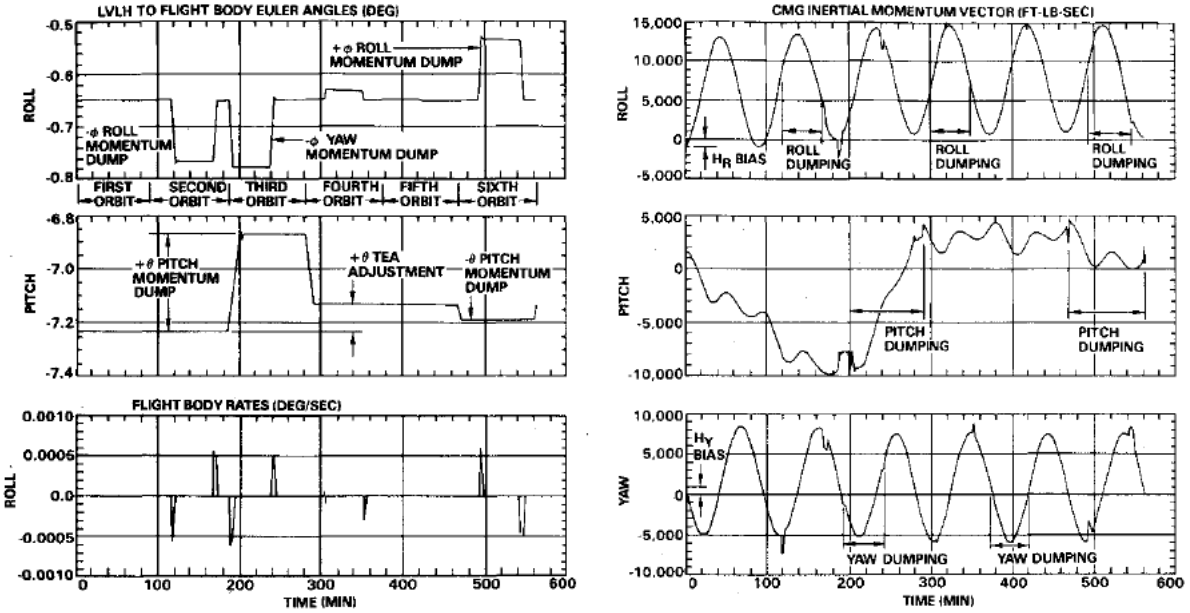

Figure 3.1: Attitude, attitude rate, and momentum for periodic method [11]

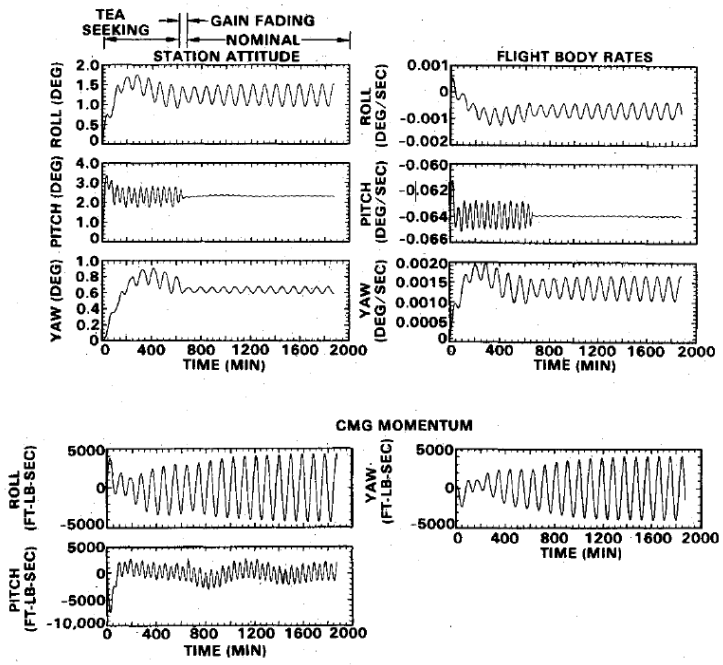

Figure 3.2: Stable response achieved and CMG system momentum bounded and centered after TEA seeking [11]

Overall, although the straightforwardness of the discussed approaches make them an appealing choice for ACMM, their effectiveness for Starlab may be limited by different factors. Firstly, pitch and roll/yaw dynamics are coupled for Starlab, which invalidates the use of simplified, decoupled systems for control design as the one proposed in Woo et al.[11]. Secondly, all of the mentioned strategies rely on the assumption of a very well defined disturbance profile as proposed in [10]. While Harduvel [12] and Dang et al. [13] consider an attitude dependent component within the disturbance, Woo et al. [11] completely disregard this contribution. The mismatch between the real environmental torque and the modeled one significantly deteriorates the performance and robustness of these linear control strategies, accentuating the need to improve environmental torque modeling. Finally, LQR tuning does not allow the designer to explicitly prioritize disturbance rejection for a continuous range of frequencies where the environmental torques are expected. Additionally, the process of optimizing the choice of the weighting matrices for LQR definition is not always clear, especially for a high-order system. Dang et al. [13] attempt to address this issue by using a pole placement algorithm. In this case, the tuning effort is shifted to understanding what poles best capture the desired system behavior.

3.2. Linear Robust Control Methods

Robust control aims to guarantee stability and performance in the presence of system uncertainties, such as variations in inertia and external disturbance modeling errors. Unlike adaptive strategies, which make real-time parameter modifications, robust control methods ensure a predefined level of performance in the presence of uncertainties.

In 1992, Elgersma et al. [14] presented two different methodologies for controller design. Firstly, an H_∞ optimization design is proposed where the trade-offs between attitude and momentum error minimization are outlined. As a second approach, the authors build a simplified, classical controller that breaks the problem into separate inner and outer loops for ACMM. This simpler design has comparable performance when compared to the H_∞ synthesized controller as well as a significantly lower order. To validate both designs, a structured singular value analysis is conducted, confirming controller stability under system uncertainties.

Five years later, Byun et al. [15] introduced a mixed H_2/H_∞ control design with structured uncertainties. While H_2 control design allows nominal performance optimization, H_∞ control design ensures guaranteed robustness margins. The resulting suboptimal controller is capable of handling mass property variations, atmospheric density changes, and sensor noise. The resulting design was tested using a full multibody model of the ISS with articulating appendages. In fact, a significant part of the paper's contribution revolves around the derivation of the linearized dynamics for a spacecraft with multiple appendages. The results demonstrate that the designed controller maintains both attitude and CMG momentum within the required bound despite the introduced model uncertainties.

Wang et al. [16] used the gravity gradient and aerodynamic torques to perform momentum unloading. The paper proposes a control strategy based on a linearized time-invariant model, and a weighted-state H_∞ controller, which defines the trade-off between attitude tracking and momentum management. Additionally, the use of solar array rotations was explored as a way to assist in momentum unloading by allowing control over the aerodynamic torque acting on the spacecraft. Simulation results showed that the weighted-state H_∞ controller stabilized the station's attitude after four orbits, decreasing the required control torque and solar panel adjustments when compared to a standard H_∞ controller.

More recently, in 2014, Han et al. [17] proposed a robust two-step approach to ACMM. Firstly, to isolate uncertain parameters in the inertia matrix, the proposed strategy used the maximum rank decomposition method. Secondly, an optimal H_∞ controller is designed via linear matrix inequalities. This methodology is able to handle both constant and cyclic disturbances and ensures adequate transient behavior. The integration of an internal model of orbital disturbances in the controller structure supports the rejection of sinusoidal environmental torques. Simulations showed that both bounded angular momentum and attitude oscillations were achieved under multiple uncertainty scenarios.

All in all, one of the main advantages of the H_∞ framework is the minimization of the peak gain of the system transfer across all frequencies, ensuring a predetermined level of performance. However, similarly to the approaches that were analyzed in Section 3.1, the above mentioned strategies also rely on the assumption that the aerodynamic torque model can be approximated by the profile described in [10].

Additionally, the high order of the resulting controllers frequently requires an additional step of controller order reduction, to prevent having overly complex controllers which can be computationally expensive to implement.

3.3. Adaptive Techniques

Adaptive control strategies are suitable for dynamic systems with parameter uncertainties. Unlike robust controllers, which guarantee stability and robustness for bounded uncertainties, adaptive controllers learn and adjust to system variations over time. In the scope of Starlab, adaptive control is an appealing strategy to handle time-varying inertia, unknown external disturbances, as well as sensor or actuator changes.

In 1997, Paynter et al. [18] proposed an indirect adaptive nonlinear controller using nonlinear feedback linearization and an Extended Kalman Filter (EKF) for mass property estimation. The method consists of transforming the full nonlinear spacecraft dynamics into a canonical form so that linear control laws can be applied to the transformed system. The EKF is able to update the mass property estimates in real time and probing signals are used to improve the observability of the mass properties. The proposed controller was tested for configuration changes of the ISS, showcasing its robustness in handling ACMM, without small-angle approximations or inertia symmetry assumptions. All in all, adaptive control eliminates the need of gain scheduling, which makes this strategy very suitable for reconfigurable platforms such as Starlab. However, it is important to highlight that implementation complexity, the need for continuous excitation for identifiability, and sensitivity to sensor noise in EKF-based estimation may challenge the applicability of this control technique.

In 2013, Zhu et al. [19] introduced a State-Dependent Riccati Equation (SDRE) controller for spacecraft momentum management, using the θ-D technique to approximate the SDRE solution while decreasing the computational load. The design of this controller was based on a three-axis coupled model, including full moment of inertia, in addition to the gravity gradient torque and cyclic aerodynamic disturbances. By manipulating the nonlinear system into a state-dependent linear form, they designed optimal feedback gains that are able to adapt online. Simulations showed that this method successfully drove the system to TEAs while keeping actuator momentum bounded. Additionally, it was shown that disturbances along the roll axis cannot be fully filtered out, which is an inherent property of the system. Overall, at the cost of real-time computational effort due to onboard gain computation, this method showcases the advantages of adaptability, by preserving adequate performance under significant inertia variations and products of inertia.

Sainudeen et al. [20] presented a simpler adaptive control strategy for ACMM using a two-loop architecture where attitude control is handled as the outer loop and momentum management as the inner loop. The control system uses model reference adaptive control as well as Lyapunov's direct method for stability analysis. Additionally, the paper introduces a dead zone in the momentum management loop to improve the system's efficiency, by reducing unnecessary control activity near equilibrium, therefore preventing actuator saturation. The proposed method's performance was compared against linear controllers, and it was shown that the presented control strategy offered better tracking and momentum regulation, particularly under parameter uncertainty. This method allows the controller to adapt without estimation of uncertain parameters, unlike Paynter et al. [18] who explicitly estimate mass properties. However, the stability guarantees are based on the linearized model, making it less suitable for highly nonlinear regimes.

In conclusion, adaptive techniques offer flexibility to model uncertainties in the scope of the ACMM problem. The first and main advantage to these approaches is that the designer's effort shifts from gain tuning to specification of adaptation factors. Secondly, the adaptability of the strategies augments the operational region of the control loop when comparing to classical linear methods. However, these advantages come with challenges, including high computational complexity, sensitivity to sensor noise, need for continuous excitation for estimation.

3.4. Observer-based and disturbance estimation techniques

Observers play a critical role in full-state feedback unavailability or when external disturbances must be estimated in real time. In the context of Starlab, where only attitude measurements are provided, and where persistent environmental torques (e.g. gravity gradient, aerodynamic drag) must be managed without using thrusters, observers are particularly relevant. By estimating unmeasured states and lumped

disturbances, observer-based approaches have the ability to extend controllability.

Liu et al. [21] presented an ACMM approach using partial state feedback. The method combines Active Disturbance Rejection Control (ADRC) with LQR, using Recursive Least Squares (RLS) algorithms to address system uncertainties, and a compensator that targets non-accumulating disturbances. The unavailability of full-state knowledge is handled with an extended state observer (ESO). The proposed technique was able to maintain momentum within adequate bounds, while relying only on attitude measurements. When designing the observer, it is assumed that aerodynamic torque follows the model proposed in [10].

In 2018, Liu et al. [22] proposed a control strategy to address the continuous momentum management problem for velocity-free spacecraft, without direct angular velocity measurements. The approach includes a Linear Extended State Observer (LESO) to estimate angular velocities and high-order cyclic disturbance torques with an LQR controller. Similarly to the previous strategy, this approach proposes the introduction of a non-accumulated compensation strategy, which filters out low-frequency or constant disturbance components estimated with the LESO. This prevents long-term momentum accumulation which is typically associated with continuous disturbance rejection. A control effort limiter is also included to avoid actuator saturation. The conducted simulations showcase robust attitude tracking, bounded momentum evolution, and disturbance rejection under sensor noise and inertia variations.

In 2021, Liu et. al [23] extended the above approaches by proposing a Hierarchical Compensation-based ADRC strategy, which combines an Extended State Observer (ESO), RLS algorithm, and an LQR controller (Figure 3.3). In this framework, the ESO estimates the system's states as well as total disturbances, and the RLS algorithm estimates the parameters that characterize the constant and sinusoidal components of the disturbance in real time. The hierarchical compensation structure is applied to suppress matched and mismatched uncertainties separately, improving both control performance and momentum management. To validate this method, a 9-degree-of-freedom semi-physical model was used, confirming the effectiveness of this solution under more realistic dynamics.

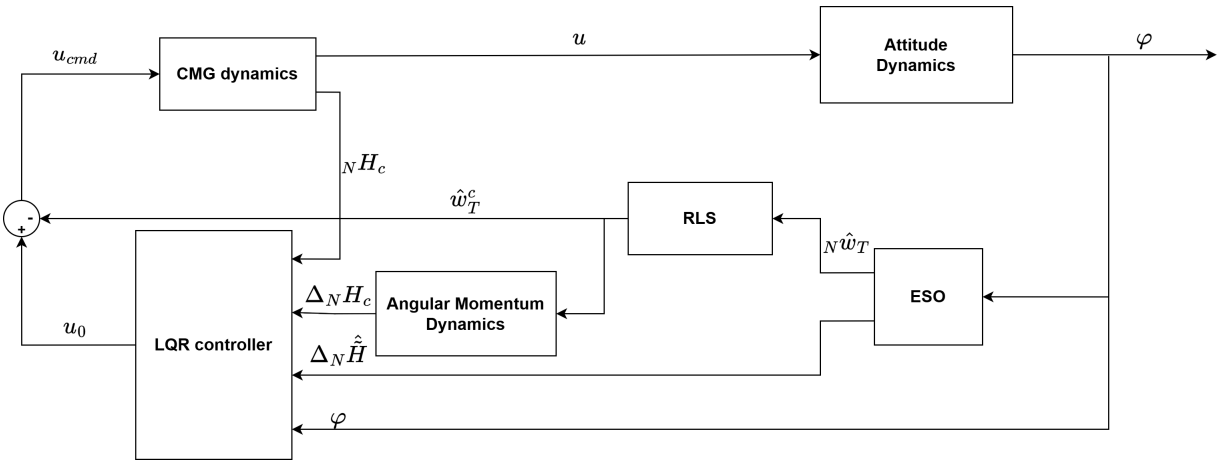

Figure 3.3: Hierarchical ADRC architecture [23]

To sum up, observer-based control techniques are extremely suitable for systems where not all states are measured. Furthermore, the aforementioned methods explicitly account for both modeled and unmodeled disturbances. However, there are several disadvantages to these methods. Firstly, an attitude-dependent aerodynamic torque contribution is not included in the linear model used for LQR controller design. Secondly, the introduction of an observer in the control loop introduces additional tuning parameters and sensitivity to sensor noise. Finally, cascading an observer with an RLS estimator can lead to an amplification of the parameter estimation errors.

3.5. Learning-based controllers

With an increasing demand for high adaptability in long-duration space missions and the emergence of data-driven algorithms, learning-based techniques can be potential alternatives to traditional model-based

designs. Their ability to adapt to complex dynamics, actuator uncertainties, and unmodeled disturbances make them an appealing choice for spacecraft such as Starlab.

In 2000, Choi et al. [24] proposed a new approach for the ACMM problem, by combining Artificial Neural Networks (ANNs) with a linear PD controller (Figure 3.4). The ANN is trained online to compensate for unknown dynamics and disturbance torques with weight adaptation guided by a Lyapunov-based learning law to ensure system stability. Simulations demonstrated that the controller was able to perform successful attitude tracking, while preventing momentum buildup under inertia uncertainty conditions.

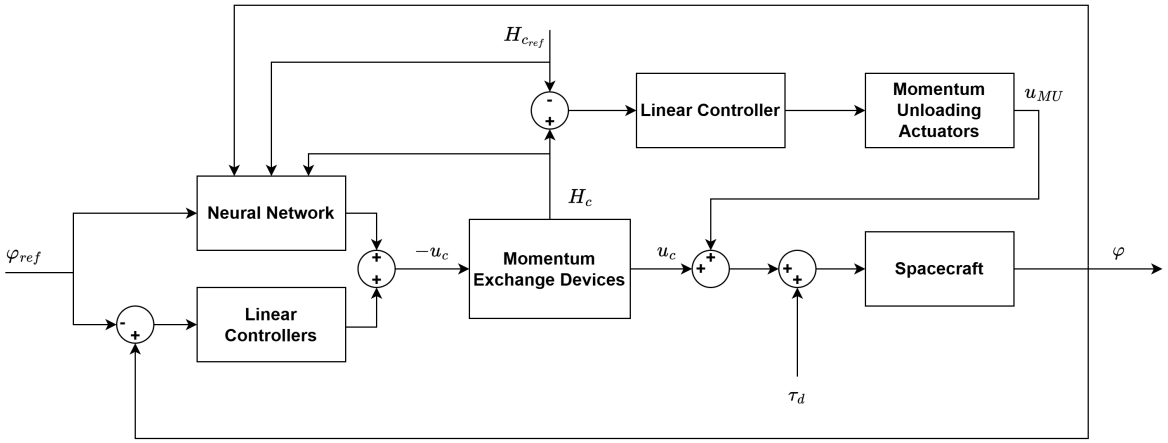

Figure 3.4: Neural network-based approach architecture [24]

One of the main benefits of using real-time learning algorithms is that the system is able to slowly adjust to varying conditions, reducing reliance on extremely accurate models for control design. However, there is still some reluctance by the industry to use learning-based methods due to several reasons. Firstly, the learning performance and stability heavily depend on the tuning of adaptation rates and are sensitive to sensor noise and transient behavior. Secondly, and most importantly, there are no formal robustness guarantees for these methods, and their high computational demands for real-time adaptation may limit their applicability.

3.6. Summary and Discussion

This chapter has discussed and analyzed the state-of-the-art control strategies for ACMM, separating them into five distinct categories: classical linear control, robust control methods, adaptive techniques, observer-based and disturbance estimation strategies, and learning-based controllers. The analysis reveals that each category presents a specific balance between implementation complexity, performance guarantees, and applicability to Starlab's specific operational requirements.

When considering classical approaches such as LQR-based techniques, the primary advantage lies in their straightforward implementation. However, these methods may present non-intuitive tuning for high-order systems. The $\mathcal{H}_\infty$ framework offers a frequency-domain perspective that directly translates performance requirements into closed-loop transfer function specifications, while simultaneously providing explicit bounds on system behavior under uncertainty. Adaptive control strategies are characterized by real-time parameter adaptation, therefore increasing the operational region of the controller at the expense of increased computational effort. By estimating states that cannot be directly measured as well as disturbance contributions, observer-based strategies enhance control capability. The inclusion of an observer, however, causes increased sensitivity to noisy measurements and increase the set of parameters requiring tuning. Finally, learning-based methods offer flexibility in uncertain environments but increase the on-board computational load, while introducing interpretability challenges and lacking the formal performance guarantees required for deployment in safety-critical applications.

All of these methodologies, although fundamentally different, converge in the fact that the aerodynamic torque is consistently oversimplified, by frequently omitting the relationship between spacecraft attitude and the resulting disturbance. The disturbance torque concentrates energy from DC through frequencies

up to eight times the orbital period, making the suppression of low-frequency components essential for preventing actuator saturation through momentum buildup. Simultaneously, control effort must be prevented at higher frequencies to avoid exciting structural modes. All in all, these requirements suggest that an $\mathcal{H}_\infty$ formulation would be well-suited for the problem at hand, as it directly minimizes the peak closed-loop gain from disturbances to errors across the relevant frequency band. Nevertheless, it is important to note that the effectiveness of this control design depends on the accuracy of the considered plant model. In this way, the aerodynamic disturbance must first be characterized in a way that captures its variation with attitude, such that it can be integrated into the linear dynamics used for controller synthesis.

4

Research Proposal

The previous chapter presented an extensive review of the state-of-the-art approaches to ACMM, highlighting their theoretical foundations, practical implementations, and limitations in the context of Starlab. Building on the insights gained from this literature study, Section 4.1 highlights the remaining research gaps that motivate further investigation and clarifies the rationale behind the selected control strategy. From the identified gap, the research questions are presented in Section 4.2.

4.1. Research Gap

As previously discussed, the ACMM problem of large, long-duration spacecraft such as Starlab presents several already-established challenges. These include minimizing both attitude and CMG angular momentum errors, in the presence of environmental torques. Their competing nature requires that a trade-off is achieved, since it is physically infeasible to eliminate attitude and momentum errors simultaneously. The overall goal is therefore to mitigate momentum accumulation such that momentum-dumping by thruster use is minimized, since the latter disrupts the microgravity environment to be maintained inside the station, and severely increases mission operational costs. Revisiting these challenges in the light of Starlab's mission context highlights the need for a control strategy capable of ensuring both robustness and long-term momentum stability.

In the previous chapter, the review of the state-of-the-art control methods for ACMM revealed a wide range of approaches, each with distinct advantages and limitations. Classical linear control strategies, such as LQR-based designs, offer simplicity and ease of implementation, but the tuning of the weighting matrices is not always clear, especially for high order systems. Robust control techniques provide guaranteed stability margins under uncertainty but their validity is confined to the envelope region surrounding the operating point used for system linearization. Adaptive controllers increase this envelope by adjusting their parameters in real time to cope with unknown or changing system properties. However, this adaptability can compromise stability guarantees and increase computational demands. Observer-based and disturbance estimation strategies improve control performance by estimating non-measurable states and disturbance contributions in real-time. The inclusion of an observer makes the system more vulnerable to sensor noise and increases the tuning parameters of the problem. Finally, learning-based controllers have shown promise in handling highly nonlinear and uncertain environments through data-driven optimization. However, their on-board feasibility, interpretability and reliability remain unappealing for safety-critical missions such as Starlab. Despite these methodological differences, all of these approaches share a reliance on simplifying assumptions, particularly the use of aerodynamic torque models that many times neglect the linear dependence of attitude effects on the spacecraft attitude.

In the case of Starlab, the operational constraints and disturbance characteristics can be conveniently analyzed in the frequency domain. The dominant disturbance frequencies range from DC to eight times the orbital rate, and the most critical performance indicators include the maximum allowable steady-state attitude error and the accumulation of the CMG persistent momentum component. Since the oscillatory part of the response is a secondary concern, the main objective becomes the attenuation of steady-state and low-frequency disturbance components. Simultaneously, the controller must avoid exciting the structural flexible modes, whose frequencies are known and lie above the range of the dominant disturbances. This motivates the use of an $\mathcal{H}_\infty$ synthesis framework, which is particularly well suited for minimizing worst-case disturbance effects and enduring robust performance across the relevant frequency range.

To enable this formulation, a model identification process must first be performed to characterize the aerodynamic torque and estimate its linear dependence on attitude variables. This identified contribution can then be incorporated into the linearized dynamic model used for the design of the $\mathcal{H}_\infty$ controller. Within this framework, the control problem can be addressed in a robustness-oriented manner, while fulfilling the frequency-domain requirements specific to Starlab' operational scenario.

4.2. Research Objectives & Questions

After having precisely determined where the research gap lies, the previously stated research objectives and questions from Chapter 1 can be refined according to the chosen methodology.

Research Objective 1

To characterize the dominant environmental disturbances – gravity gradient and aerodynamic torque – such that they can be integrated into the $\mathcal{H}_\infty$ controller synthesis framework.

Research Objective 2

To design and implement an $\mathcal{H}_\infty$-based control strategy, focusing on disturbance rejection, for spacecraft Attitude Control and Momentum Management (ACMM) in the context of the Starlab space station's nominal mode.

Research Objective 3

To evaluate the robustness, performance, and limitations of the $\mathcal{H}_\infty$ controller using a high-fidelity Starlab simulator.

From the previously defined research objectives, several research questions and sub-questions can be defined to better motivate, structure and guide the proposed project.

Research Question 1

How can the mission requirements for Starlab (continuous nadir pointing, minimal thruster usage, and long-term operational efficiency) together with the physical constraints of the ACMM problem (actuator momentum capacity, mass distribution, flexible modes, and environment-induced disturbances) be translated into concrete control-design requirements?

1.1 What are the primary control objectives (performance goals) and how are they prioritized?
1.2 Which measurable performance metrics represent those objectives?
1.3 How can the spacecraft's physical constraints be represented in the $\mathcal{H}_\infty$ control design?
1.4 How should environmental disturbances be characterized for robust control design?
1.5 Which control architecture best incorporates these requirements and constraints?

Research Question 2

How do modeling assumptions affect the fidelity and validity of the spacecraft model used for $\mathcal{H}_\infty$ control design?

2.1 What are the main simplifying assumptions adopted to formulate a model of the spacecraft for $\mathcal{H}_\infty$ control design?

2.2 How do these assumptions influence the accuracy and applicability of the model in nominal conditions?

2.3 Within which operational boundaries does the linearized model remain valid for robust control design?

Research Question 3

How can the robustness and performance of the synthesized control system be validated across different configurations, orbital conditions, and environmental variations?

3.1 How can the controller's performance be evaluated under nominal conditions?

3.2 How can the controller's performance be validated across different orbital conditions?

3.3 How can the overall robustness envelope established and verified?

4.3. Planning

After clearly defining a research proposal for the project to conduct, it is crucial to structure the latter into well-defined work packages for an overview of the tasks and subtasks, as well as the main milestones and timeline of the thesis. Over the course of the project, the original plan can sometimes be subjected to changes due to delays, improved understanding of the problem at hand and new insights based on preliminary results. The final followed timeline is represented in the form of a Gantt chart in Chapter A.

5

Linearized Dynamics

Although the complete nonlinear equations of motion of the space station have been established in Chapter 2, a linearized model is required to apply the $\mathcal{H}_\infty$ synthesis framework adopted in this project. Considering this, the present chapter focuses on the derivation and formulation of this linearized system. The objective is to obtain a state-space representation which is valid in the expected operational region. This model will then provide the basis for both the control design and the assessment of the system's robustness.

The process of linearization consists of approximating a nonlinear function by its first-order Taylor expansion around a given operating point. For a generic function f, depending on x, the linearized form around the point x^* is expressed as [25]:

$$f(x) \approx f(x^*) + \frac{\partial f}{\partial x}\Big|_{x=x^*} \cdot (x - x^*) \tag{5.1}$$

Following this procedure, the linearized equations of motions and dynamics of the CMG will be derived in the following sections.

5.1. Operating Point

As already established, the linearization is performed around a specific operating point. In this case, it was considered that $x^* = [\varphi^*_{B/N} \quad {}_B\omega^*_{B/I} \quad {}_BH^*_c]^T$, with

$$\begin{aligned} \varphi^*_{B/N} &= \begin{bmatrix} 0 & \theta^* & 0 \end{bmatrix}^T \\ {}_B\omega^*_{B/I} = {}_B\omega_{N/I} &\xrightarrow{\varphi_{B/N}=\varphi^*_{B/N}} {}_B\omega^*_{B/I} = \begin{bmatrix} 0 & -\omega_0 & 0 \end{bmatrix}^T \\ {}_BH^*_c &= \begin{bmatrix} 0 & 0 & 0 \end{bmatrix}^T \end{aligned} \tag{5.2}$$

The operating point selected for linearization corresponds to a nominal attitude in which the roll and yaw angles are zeros, while the pitch angle assumes an arbitrary value θ^*. This choice reflects the operational configurations of Starlab, for which the equilibrium pitch attitude can vary depending on the station's geometry. In particular, certain configurations lead to steady-state pitch angles of significant magnitudes, where the accuracy of conventional small angle approximations might be degraded. Additionally, the reference angular rate of the body frame with respect to the inertial frame is taken as the angular rate of the LVLH frame with respect to the inertial frame, which translates the nominal orbital motion of the spacecraft. Finally, the CMG angular momentum is assumed to be zero at the operating point, since the goal is to minimize the magnitude of the momentum. These definitions ensure that the linearized model remains consistent with the physical and operational constraints of the system.

5.2. Linearization of the Kinematic Equations

To derive the linearized kinematic equations, the previously derived equation in Chapter 2 is taken as the starting point:

$$\dot{\varphi}_{B/N} = \begin{bmatrix} \frac{\cos\psi}{\cos\theta} & -\frac{\sin\psi}{\cos\theta} & 0 \\ \sin\psi & \cos\psi & 0 \\ -\cos\psi\tan\theta & \sin\psi\tan\theta & 1 \end{bmatrix} {}_B\omega_{B/I} + \omega_0 \begin{bmatrix} \sin\phi\tan\theta \\ \cos\phi \\ -\frac{\sin\phi}{\cos\theta} \end{bmatrix} \tag{2.10}$$

Firstly, the equation must be evaluated at the operating point:

$$\dot{\varphi}_{B/N}(x^*) = \begin{bmatrix} \frac{1}{\cos\theta^*} & 0 & 0 \\ 0 & 1 & 0 \\ -\tan\theta^* & 0 & 1 \end{bmatrix} \begin{bmatrix} 0 \\ -\omega_0 \\ 0 \end{bmatrix} + \omega_0 \begin{bmatrix} 0 \\ 1 \\ 0 \end{bmatrix} = \begin{bmatrix} 0 \\ 0 \\ 0 \end{bmatrix} \tag{5.3}$$

Secondly, the Jacobian matrices are computed with respect to each state and evaluated at the operating point:

$$\frac{\partial\dot{\varphi}_{B/N}}{\partial\phi} \Big|_{x=x^*} = \omega_0 \begin{bmatrix} \tan\theta^* \\ 0 \\ -\frac{1}{\cos\theta^*} \end{bmatrix} \tag{5.4}$$

$$\frac{\partial\dot{\varphi}_{B/N}}{\partial\theta} \Big|_{x=x^*} = \begin{bmatrix} \frac{\sin\theta^*}{\cos^2\theta^*} & 0 & 0 \\ 0 & 0 & 0 \\ -\frac{1}{\cos^2\theta^*} & 0 & 0 \end{bmatrix} \begin{bmatrix} 0 \\ -\omega_0 \\ 0 \end{bmatrix} + \omega_0 \begin{bmatrix} 0 \\ 0 \\ 0 \end{bmatrix} = \begin{bmatrix} 0 \\ 0 \\ 0 \end{bmatrix} \tag{5.5}$$

$$\frac{\partial\dot{\varphi}_{B/N}}{\partial\psi} \Big|_{x=x^*} = \begin{bmatrix} 0 & -\frac{1}{\cos\theta^*} & 0 \\ 1 & 0 & 0 \\ 0 & \tan\theta^* & 0 \end{bmatrix} \begin{bmatrix} 0 \\ -\omega_0 \\ 0 \end{bmatrix} = \omega_0 \begin{bmatrix} \frac{1}{\cos\theta^*} \\ 0 \\ -\tan\theta^* \end{bmatrix} \tag{5.6}$$

$$\frac{\partial\dot{\varphi}_{B/N}}{\partial {}_B\omega_{B/I}} \Big|_{x=x^*} = \begin{bmatrix} \frac{1}{\cos\theta^*} & 0 & 0 \\ 0 & 1 & 0 \\ -\tan\theta^* & 0 & 1 \end{bmatrix} \tag{5.7}$$

In this way, the final linearized kinematic equations can be defined as follows:

$$\dot{\varphi}_{B/N} = \underbrace{\omega_0 \begin{bmatrix} \tan\theta^* & 0 & \frac{1}{\cos\theta^*} \\ 0 & 0 & 0 \\ -\frac{1}{\cos\theta^*} & 0 & -\tan\theta^* \end{bmatrix}}_{A_{\varphi\varphi}} \Delta\varphi + \underbrace{\begin{bmatrix} \frac{1}{\cos\theta^*} & 0 & 0 \\ 0 & 1 & 0 \\ -\tan\theta^* & 0 & 1 \end{bmatrix}}_{A_{\varphi\omega}} \Delta\omega \tag{5.8}$$

with $\Delta\varphi = \varphi_{B/N} - \varphi^*_{B/N}$ and $\Delta\omega = {}_B\omega_{B/I} - {}_B\omega_{N/I} = {}_B\omega_{B/N}$.

5.3. Linearization of the Dynamic Equations

In this section, the linearization is carried out for the spacecraft's dynamic equations. The total external torque, which includes contributions from the gravity gradient and aerodynamic torques is not explicitly linearized at this stage. Following the same process as before, the previously derived dynamics equation in Chapter 2 is taken as the starting point:

$${}_B\dot{\omega}_{B/I} = -[{}_BJ]^{-1}[{}_B\omega_{B/I}\times] \cdot {}_BJ \cdot {}_B\omega_{B/I} + [{}_BJ]^{-1}{}_B\tau \tag{2.17}$$

Evaluating the previous equation in the operating point yields:

$${}_B\dot{\omega}_{B/I} \Big|_{x=x^*} = -[{}_BJ]^{-1}[{}_B\omega_{N/I}\times] \cdot {}_BJ \cdot {}_B\omega_{N/I} + [{}_BJ]^{-1}{}_B\tau|_{x=x^*} \tag{5.9}$$

After this, the Jacobian matrices were computed with respect to each state and evaluated at the operating point:

$$\frac{\partial_B \dot{\omega}_{B/I}}{\partial \varphi} \mid_{x=x^*} = [{}_B J]^{-1} \frac{\partial_B \tau}{\partial \varphi} \mid_{x=x^*} \tag{5.10}$$

$$\frac{\partial_B \dot{\omega}_{B/I}}{\partial_B \omega_{B/I}} \mid_{x=x^*} = [{}_B J]^{-1}[({}_B J \cdot {}_B \omega_{N/I})\times] - [{}_B J]^{-1}[{}_B \omega_{N/I}\times] \cdot {}_B J \tag{5.11}$$

Considering this, the final linearized dynamic equation can be defined as:

$$\begin{aligned} \Delta\dot{\omega} = \underbrace{(\frac{\partial_B \tau_g}{\partial \varphi} \mid_{x=x^*} + \frac{\partial_B \tau_a}{\partial \varphi} \mid_{x=x^*})}_{A_{\omega\varphi}} \Delta\varphi + \underbrace{\left([{}_B J]^{-1}[({}_B J \cdot {}_B \omega_{N/I})\times] - [{}_B J]^{-1}[{}_B \omega_{N/I}\times] \cdot {}_B J\right)}_{A_{\omega\omega}} \Delta\omega \\ + [{}_B J]^{-1}\, {}_B \tau_c + [{}_B J]^{-1}\, {}_B \tau_{g,\text{rest}} + [{}_B J]^{-1}\, {}_B \tau_{a,\text{rest}} - [{}_B J]^{-1}[{}_B \omega_{N/I}\times] \cdot {}_B J \cdot {}_B \omega_{N/I} \end{aligned} \tag{5.12}$$

5.4. LEO Disturbance Linearization

This section presents the linearization of the environmental torques – gravity gradient and aerodynamic torque. While the gravity gradient torque is linearized analytically, as its expression depends only on the spacecraft inertia properties, attitude and orbit geometry, the aerodynamic torque will only be addressed conceptually, since its detailed linear model identification is presented in Part II.

5.4.1. Gravity Gradient Torque

The previously derived expression for the gravity gradient torque is first recalled and serves as basis for the subsequent linearization:

$${}_B \tau_g = 3\omega_0^2 \begin{bmatrix} 0 & -T_{3,3} & T_{2,3} \\ T_{3,3} & 0 & -T_{1,3} \\ -T_{2,3} & T_{1,3} & 0 \end{bmatrix} \cdot {}_B J \cdot \begin{bmatrix} T_{1,3} \\ T_{2,3} \\ T_{3,3} \end{bmatrix} \tag{2.22}$$

Writing the previous equation explicitly in terms of Euler angles yields the following expression:

$$\begin{aligned} {}_B \tau_g = 3\omega_0^2 \begin{bmatrix} 0 & -\cos\phi\cos\theta & \cos\psi\sin\phi + \cos\phi\sin\psi\sin\theta \\ \cos\phi\cos\theta & 0 & -\sin\phi\sin\psi + \cos\phi\cos\psi\sin\theta \\ -\cos\psi\sin\phi - \cos\phi\sin\psi\sin\theta & \sin\phi\sin\psi - \cos\phi\cos\psi\sin\theta & 0 \end{bmatrix} \cdot \\ \cdot {}_B J \cdot \begin{bmatrix} \sin\phi\sin\psi - \cos\phi\cos\psi\sin\theta \\ \cos\psi\sin\phi + \cos\phi\sin\psi\sin\theta \\ \cos\phi\cos\theta \end{bmatrix} \end{aligned} \tag{5.13}$$

The previous equation must be evaluated at the operating point, resulting in the following expression:

$${}_B \tau_g \mid_{x=x^*} = 3\omega_0^2 \begin{bmatrix} \sin\theta^*\cos\theta^* J_{2,1} - \cos^2\theta^* J_{2,3} \\ \sin\theta^*\cos\theta^*(J_{3,3} - J_{1,1}) + \cos^2\theta^* J_{1,3} \\ \sin^2\theta^* J_{2,1} - \sin\theta^*\cos\theta^* J_{2,3} \end{bmatrix} \tag{5.14}$$

The Jacobian matrices with respect to the Euler angles are given by:

$$\frac{\partial_B \tau_g}{\partial \phi} \mid_{x=x^*} = 3\omega_0^2 \begin{bmatrix} (J_{3,3} - J_{2,2}) \cos\theta^* - J_{3,1} \sin\theta^* \\ J_{1,2} \cos\theta^* + J_{3,2} \sin\theta^* \\ -J_{1,3} \cos\theta^* + (J_{1,1} - J_{2,2}) \sin\theta^* \end{bmatrix} \tag{5.15}$$

$$\frac{\partial_B \tau_g}{\partial \theta} \mid_{x=x^*} = 3\omega_0^2 \begin{bmatrix} \sin 2\theta^* J_{2,3} + \cos 2\theta^* J_{2,1} \\ -2 \sin 2\theta^* J_{3,1} + \cos 2\theta^* (J_{3,3} - J_{1,1}) \\ -\cos 2\theta^* J_{2,3} + \sin 2\theta^* J_{2,1} \end{bmatrix} \tag{5.16}$$

$$\frac{\partial_B \tau_g}{\partial \psi} \mid_{x=x^*} = 3\omega_0^2 \begin{bmatrix} -\sin^2\theta^* J_{3,1} + \sin\theta^* \cos\theta^* (J_{3,3} - J_{2,2}) \\ \sin\theta^* \cos\theta^* J_{1,2} + \sin^2\theta^* J_{3,2} \\ -\sin\theta^* \cos\theta^* J_{1,3} + \sin^2\theta^* (J_{1,1} - J_{2,2}) \end{bmatrix} \tag{5.17}$$

Finally, the gravity gradient torque can be approximated by the following linear expression:

$$\begin{aligned} {}_B\tau_g = {} & 3\omega_0^2 \begin{bmatrix} (J_{3,3} - J_{2,2}) \cos\theta^* - J_{3,1} \sin\theta^* \\ J_{1,2} \cos\theta^* + J_{3,2} \sin\theta^* \\ -J_{1,3} \cos\theta^* + (J_{1,1} - J_{2,2}) \sin\theta^* \end{bmatrix} \Delta\phi \\ & + 3\omega_0^2 \begin{bmatrix} \sin 2\theta^* J_{2,3} + \cos 2\theta^* J_{2,1} \\ -2 \sin 2\theta^* J_{3,1} + \cos 2\theta^* (J_{3,3} - J_{1,1}) \\ -\cos 2\theta^* J_{2,3} + \sin 2\theta^* J_{2,1} \end{bmatrix} \Delta\theta \\ & + 3\omega_0^2 \begin{bmatrix} -\sin^2\theta^* J_{3,1} + \sin\theta^* \cos\theta^* (J_{3,3} - J_{2,2}) \\ \sin\theta^* \cos\theta^* J_{1,2} + \sin^2\theta^* J_{3,2} \\ -\sin\theta^* \cos\theta^* J_{1,3} + \sin^2\theta^* (J_{1,1} - J_{2,2}) \end{bmatrix} \Delta\psi \\ & \underbrace{+ 3\omega_0^2 \begin{bmatrix} \sin\theta^* \cos\theta^* J_{2,1} - \cos^2\theta^* J_{2,3} \\ \sin\theta^* \cos\theta^* (J_{3,3} - J_{1,1}) + \cos^2\theta^* J_{1,3} \\ \sin^2\theta^* J_{2,1} - \sin\theta^* \cos\theta^* J_{2,3} \end{bmatrix}}_{{}_B\tau_{g,\text{rest}}} \end{aligned} \tag{5.18}$$

5.4.2. Aerodynamic Torque

The aerodynamic torque arises from the interaction between the residual atmosphere and the spacecraft's surface geometry and orientation. Its dependence on the spacecraft attitude is nonlinear and configuration specific. The derivation of the linear aerodynamic model will be presented and analyzed in Part II. For now, the torque can be represented as:

$${}_B\tau_a = \frac{\partial_B \tau_a}{\partial \varphi_{B/N}} \mid_{x=x^*} \Delta\varphi + {}_B\tau_{a,\text{rest}} \tag{5.19}$$

5.5. CMG Linearized Dynamic Equations

As presented in Chapter 2, the CMG dynamic equation are given by

$${}_B\dot{H}_c = -[{}_B\omega_{B/I}\times] \cdot {}_BH_c - {}_B\tau_c \tag{??}$$

Since these equations are already linear with respect to the states and input, and considering the previously defined operating point, the linearized equation is simply expressed as

$$\Delta_B\dot{H}_c = -[{}_B\omega_{N/I}\times] \cdot \Delta_BH_c - {}_B\tau_c \tag{5.20}$$

5.6. Linearized System

Considering that $\Delta\omega = {}_B\omega_{B/N}$ and $\Delta_B H_c = {}_B H_c$, the complete linear system of equations can be expressed as follows:

$$\begin{aligned}\begin{bmatrix} \Delta\dot{\varphi} \\ {}_B\dot{\omega}_{B/N} \\ {}_B\dot{H}_c \end{bmatrix} &= \begin{bmatrix} A_{\varphi\varphi} & A_{\varphi\omega} & 0 \\ A_{\omega\varphi} & A_{\omega\omega} & 0 \\ 0 & 0 & -[{}_B\omega_{N/I}\times] \end{bmatrix} \begin{bmatrix} \Delta\varphi \\ {}_B\omega_{B/N} \\ {}_B H_c \end{bmatrix} \\ &+ \begin{bmatrix} 0 \\ [{}_B J]^{-1} \\ -I \end{bmatrix} {}_B\tau_c + \begin{bmatrix} 0 \\ [{}_B J]^{-1} \\ 0 \end{bmatrix} \left({}_B\tau_{g,rest} + {}_B\tau_{a,rest}(t) + \omega_0^2 \begin{bmatrix} -{}_B J_{2,3} \\ 0 \\ {}_B J_{1,2} \end{bmatrix} \right)\end{aligned} \tag{5.21}$$

In particular, when $\theta^* = 0$, $\Delta\varphi = \varphi_{B/N}$, and the system of equations is simplified to:

$$\begin{aligned}\begin{bmatrix} \dot{\varphi}_{B/N} \\ {}_B\dot{\omega}_{B/N} \\ {}_B\dot{H}_c \end{bmatrix} &= \begin{bmatrix} -[{}_B\omega_{N/I}\times] & I & 0 \\ A_{\omega\varphi} & [{}_B J]^{-1}\left([({}_B J \cdot {}_B\omega_{N/I})\times] - [{}_B\omega_{N/I}\times]{}_B J\right) & 0 \\ 0 & 0 & -[{}_B\omega_{N/I}\times] \end{bmatrix} \begin{bmatrix} \varphi_{B/N} \\ {}_B\omega_{B/N} \\ {}_B H_c \end{bmatrix} \\ &+ \begin{bmatrix} 0 \\ [{}_B J]^{-1} \\ -I \end{bmatrix} {}_B\tau_c + \begin{bmatrix} 0 \\ [{}_B J]^{-1} \\ 0 \end{bmatrix} \left({}_B\tau_{a,rest}(t) + \omega_0^2 \begin{bmatrix} -4 \cdot {}_B J_{2,3} \\ 3 \cdot {}_B J_{1,3} \\ {}_B J_{1,2} \end{bmatrix} \right)\end{aligned} \tag{5.22}$$

6

$\mathcal{H}_\infty$ Control Framework

The linearized dynamic model derived in the previous chapter provides the foundation required to formulate the control problem within the $\mathcal{H}_\infty$ synthesis framework. Building upon this model, the present chapter introduces the theoretical background necessary to understand and apply $\mathcal{H}_\infty$ control to the Starlab's ACMM problem. The objective is to present the main concepts and formulations underlying this robust control approach, which was selected for its ability to explicitly handle worst-case transfer gain, while addressing frequency-domain performance requirements. The chapter begins by reflecting on the motivation and origins of $\mathcal{H}_\infty$ control (Section 6.1), followed by some fundamental principles namely the definition of singular values and system norms (Section 6.2), before introducing the standard mixed-sensitivity formulation that will later be applied to the controller design (Section 6.4). Finally, in Section 6.5, the concept of stability margins is introduced as a means to assess closed-loop robustness of the system obtained through $\mathcal{H}_\infty$ synthesis. All of these considerations are presented under the scope of a general disturbance rejection problem.

6.1. Introduction to $\mathcal{H}_\infty$ Control

The concept of $\mathcal{H}_\infty$ control emerged in the early 1980s with the goal of providing peformance guarantees in the presence of model uncertainty. Classical time-domain methods such as Linear Quadratic Gaussian (LQG) control theoretically offered optimal performance, whereas in real scenarios performance was degraded. In this way, robust control rose as means to consider plant uncertainty and the gain from disturbance to error outputs in the process of controller design.

A major step in the development of $\mathcal{H}_\infty$ control was first made by Zames et al. [26], who introduced frequency-domain formulations linking sensitivity and robustness. Several methods unfolded from $\mathcal{H}_\infty$ control [27], including $\mathcal{H}_\infty$ loop shaping, $H_2/\mathcal{H}_\infty$ control, and mixed sensitivity control.

The main principle behind this control method is the $\mathcal{H}_\infty$ norm, which corresponds to the peak value of the largest singular value of a system's transfer function over frequency. The goal is to minimize this norm, therefore minimizing the energy of the worst-case output signal.

6.2. Fundamental Principles of $\mathcal{H}_\infty$ Control

To define the $\mathcal{H}_\infty$ control framework in a precise manner, two main concepts need to be established: singular values and $\mathcal{H}_\infty$ system norms. This section will briefly present their definitions and physical interpretation, and it primarily follows the formulation in [28].

6.2.1. Singular Values

The singular value decomposition of a given matrix, G, is defined as

$$G = U\Sigma V^H \tag{6.1}$$

where Σ is a diagonal matrix where the singular values are arranged across its main diagonal in descending order, and U and V are the unitary matrices of the output and input singular vectors, respectively.

The singular values of G can be computed as

$$\sigma_i(G) = \sqrt{\lambda_i\left(G^H G\right)} \tag{6.2}$$

In particular, it is important to highlight that the maximum ($\bar{\sigma}$) and minimum ($\underline{\sigma}$) singular values correspond to the largest and smallest gain for any given input direction, respectively. In other words, the gain of $G(j\omega)$ will be bounded between the maximum and minimum singular values at frequency ω.

6.2.2. $\mathcal{H}_\infty$ System Norms

For a stable linear time-invariant system with transfer function $G(s)$, the $\mathcal{H}_\infty$ norm is defined as

$$\|G\|_\infty = \max_\omega \bar{\sigma}(G(j\omega)) \tag{6.3}$$

6.3. $\mathcal{H}_\infty$ Control Problem Formulation

To set up the control problem within this framework, a generalized plant P is considered, which captures the dynamics from the exogenous input, d, and control input, u, to the performance output p and the measured output, y:

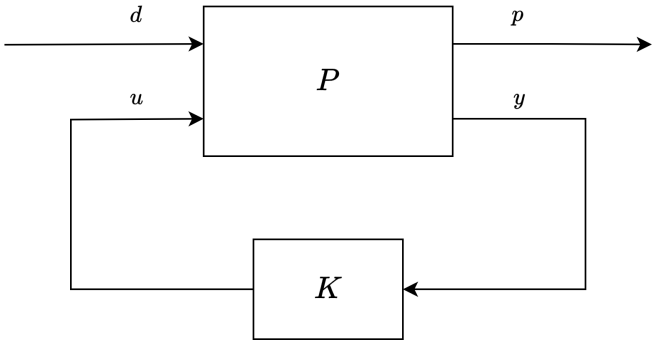

Figure 6.1: Generalized plant P for controller synthesis

Assuming that the measured output corresponds to the real output of the system, plant P can be described in the following state-space form:

$$P = \begin{cases} \dot{x} = Ax + B_1 d + B_2 u \\ p = C_1 x + D_{11} d + D_{12} u \\ y = C_2 x + D_{21} d + D_{22} u \end{cases} \tag{6.4}$$

Having defined the plant to be controlled, the $\mathcal{H}_\infty$ optimization problem can be formulated as the synthesis of a stabilizing controller K that minimizes the $\mathcal{H}_\infty$ norm of the closed loop transfer function, $T_{d\to p}$, from the exogenous input, d, to the controlled output, p:

$$\begin{array}{ll} \text{minimize} & \|T_{d\to p}\|_\infty \\ \text{subject to} & K \text{ stabilizes } P \end{array} \tag{6.5}$$

6.4. $\mathcal{H}_\infty$ Mixed-Sensitivity

The concept of $\mathcal{H}_\infty$ mixed-sensitivity is based on shaping the closed-loop transfer functions to satisfy given design requirements. In order to accomplish this, the singular values of the transfer functions are shaped throughout frequency by weighting filters.

Firstly, the plant in Figure 6.1 can be extended as the one depicted in Figure 6.2, assuming that the exogenous input, d, corresponds to a disturbance input that affects the system through the path modeled by $G_d(s)$.

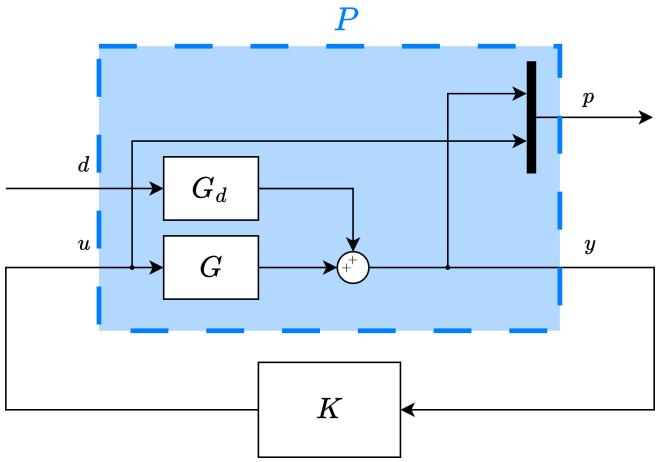

Figure 6.2: Generalized plant P with the positive feedback controller K

In this formulation, $G(s)$ denotes the nominal plant to be controlled and corresponds to the part of P that maps the control input u to the output y. In this feedback loop, three closed-loop transfer functions characterize the system's behavior:

$$L = GK, \quad S = (I + GK)^{-1}, \quad T = GK(I + GK)^{-1} \tag{6.6}$$

where L is the open loop transfer function, S is the sensitivity function, and T corresponds to the complementary sensitivity function. Considering this, the closed-loop transfer functions can be defined as

$$p = \begin{bmatrix} y \\ u \end{bmatrix} = \begin{bmatrix} SG_d \\ KSG_d \end{bmatrix} d \tag{6.7}$$

To incorporate the design requirements, weighting filters are introduced as shown in Figure 6.3.

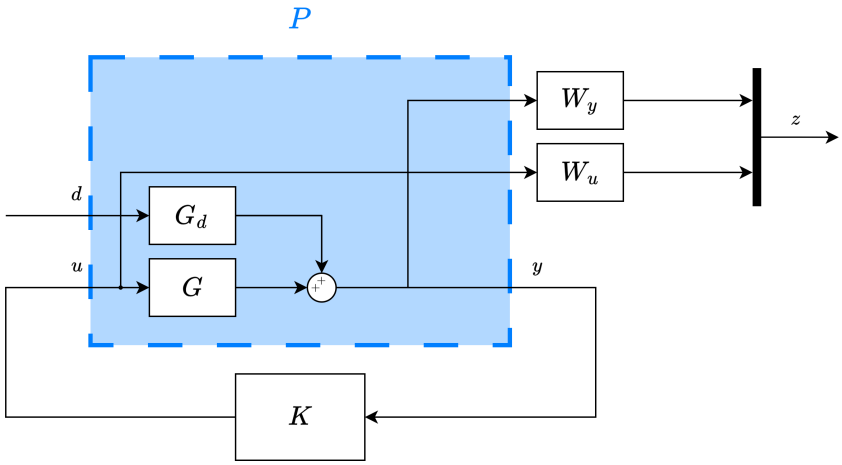

Figure 6.3: Weighted closed-loop system for control design

The mixed-sensitivity design problem is then formulated as finding a stabilizing controller K that minimizes the $\mathcal{H}_\infty$ norm of the weighted transfer functions:

$$\min_K \left\| \begin{bmatrix} W_y S \\ W_u K S \end{bmatrix} \right\|_\infty \tag{6.8}$$

In this configuration, the weighting filters define the upper bounds on the magnitude of the corresponding closed-loop transfer functions. In this way, while W_y enforces good low-frequency performance in order to reject disturbances, W_u limits the control signal magnitude to avoid excitation of flexible modes the allowed control effort along frequency.

An inherent limitation in feedback design is captured by the Bode sensitivity integral, which quantifies the trade-off between disturbance rejection and robustness. For a stable plant, the sensitivity function satisfies the following relation

$$\int_0^\infty \ln|S(j\omega)|\, d\omega = 0 \tag{6.9}$$

This expression implies that reductions of $|S(j\omega)|$ at some frequencies – in order to improve disturbance rejection or reference tracking – must be compensated by increases at some other frequencies. This effect is often referred to as the *waterbed effect* and it illustrates that the closed-loop performance can only be optimized locally in frequency. In the mixed-sensitivity framework, the definition of the weighting filters has to be tuned while complying with this fundamental constraint by attenuating sensitivity at frequencies were the disturbance is concentrated and tolerating higher amplifications at higher frequencies.

6.5. Stability Margins

In practical control design, it is essential to assess the system's closed-loop stability. No mathematical model can perfectly represent a real system, and deviations in parameters, unmodeled high-frequency dynamics and even actuator nonlinearities can all degrade performance, potentially leading to instability. Therefore, quantifying the stability margins of a control system provides a measure of how much uncertainty the closed loop can tolerate before becoming unstable.

6.5.1. Classical Gain and Phase Margins

In classical single-input single-output control theory, robustness is typically assessed using the gain and phase margins. These margins describe how much the open-loop gain or phase can vary before the closed loop reaches instability.

Intuitively, the gain margin indicates how much the open-loop gain can be increased or decreased, while the phase margin represents how much additional phase lag can be introduced before instability occurs. In practice, larger margins correspond to a more robust system that can tolerate greater modeling errors or time delays.

Although these margins provide an intuitive frequency-domain measure of robustness for Single-Input Single-Output (SISO) systems, they do not directly extend to Multiple-Input Multiple-Output (MIMO) systems, where interactions between channels can affect stability.

6.5.2. Disk Gain and Phase Margins

To overcome the limitations of classical margins in CMG systems, the disk margin concept was introduced [29]. The disk margin is able to describe simultaneous gain and phase margin variation in all feedback channels. It defines the largest amount of uncertainty – represented geometrically as a disk in the complex plane – that can be tolerated without causing instability.

Physically, disk margins define the region in the complex plane in which combined uncertainties of all feedback channels can vary without the risk of instability. A larger disk corresponds to a system that can tolerate more uncertainty, whether it arises from modeling errors or delays. In this way, disk margins generalize the classical gain and phase margins to multivariable systems while maintaining an intuitive, geometric interpretation of robustness.

Part II

Scientific Article

Attitude and Angular Momentum Control for Starlab

Carolina Baltazar Mendes *†
Delft University of Technology, 2600GB Delft, The Netherlands

Attitude Control and Momentum Management are inherently coupled in the context of a space station that relies on Momentum Exchange Devices (MEDs) for attitude control. By exploiting environmental torques, attitude deviation can be minimized while limiting the saturation of the MEDs. Existing studies often simplify the aerodynamic torque contribution or omit it from controller design. In this work, a linear mean aerodynamic torque model was identified for a Right Ascension of the Ascending Node (RAAN) corresponding to the maximum aerodynamic torque magnitude, using a least-squares approach. An $\mathcal{H}_\infty$ controller was designed for disturbance rejection for different space station configurations, where flexible-body effects were considered by reducing controller authority at high frequencies. The main findings of this work indicate that the nominal configuration of the space station lacks gravity gradient control authority for aerodynamic torque compensation, resulting in an increased attitude/momentum trade-off. The control approach was validated for a more asymmetric configuration through time-domain simulations using the derived linear model – perturbed with a representative disturbance profile constructed from data reflecting the station geometry and orbital environment – and a high-fidelity simulator. These simulations showed that the controller achieves stable performance, small attitude deviations and bounded MED momentum. Additionally, simulations were performed by varying the RAANs around the design point to identify the controller's validity region.

Nomenclature

$A, B_1, B_2, C_1, C_2, D_{11}, D_{12}, D_{21}, D_{22}$	=	state space matrices for the generalized plant P	–
H	=	angular momentum	[N m s]
I	=	3-by-3 identity matrix	–
J	=	moment of inertia of the spacecraft	[kg m^2]
$T_{X/Y}$	=	direction cosine matrix from frame Y to frame X	–
ω_0	=	orbital rate	[rad/s]
${}_Z\omega_{X/Y}$	=	angular rate of frame X with respect to frame Y, in frame Z	[rad/s]
ϕ	=	roll angle	[rad]
ψ	=	yaw angle	[rad]
τ	=	torque	[N m]
θ	=	pitch angle	[rad]
$\varphi_{X/Y}$	=	attitude vector defined from frame Y to frame X	[rad]
$[(\cdot)\times]$	=	skew symmetric matrix of the vector $(\cdot)$	–

Subscripts and Superscripts

a	=	aerodynamic
B	=	Body frame
c	=	control
d	=	disturbance
g	=	gravity gradient
I	=	inertial reference frame
N	=	local vertical local horizontal (LVLH) frame
$*$	=	linearization operating point

*MSc Student, Control and Simulation Department, Faculty of Aerospace Engineering, Delft University of Technology.
†MSc Student, Airbus Defence and Space GmbH, Friedrichshafen, Germany.

I. Introduction

Attitude Control and Momentum Management (ACMM) remains one of the main challenges in operating large spacecraft, particularly in Low Earth Orbit (LEO) [1]. While accurate attitude pointing is essential for communications, docking, and scientific payloads, momentum management ensures that the available actuators do not saturate and remain within their operational limits [2, 3].

With the planned retirement of the International Space Station (ISS), Starlab is being developed as its successor [4]. While the size of the station – in particular, its large area and moments of inertia – bring about large gravity gradient and aerodynamic torques to act on the spacecraft [5], the modular nature of the station as well as its moving robotic arm cause the system to be subjected to large inertia uncertainties. Additionally, several mission constraints pose a challenge to the ACMM problem. Firstly, it is required that the space station performs nadir pointing throughout its nominal operational mode to ensure communication, while the solar panels are kept pointing towards the Sun [6]. Secondly, due to fuel consumption and the disturbance of the micro-gravity environment for on-board science experiments, thruster use must be minimized, making Momentum Exchange Devices (MEDs) the primary source of actuation for accurate management of the attitude [7, 8]. While precise attitude pointing would cause the persistent external disturbances to quickly saturate the MEDs, eliminating angular momentum accumulation implies that the spacecraft will be oriented such that the total contribution of the external torques are minimized therefore not fulfilling the requirement of nadir pointing. For this reason, the control challenge lies in achieving an acceptable trade-off between attitude and angular momentum errors minimization [9].

Throughout the years, various strategies were used to address the ACMM problem. Early contributions relied on the use and derivation of linear systems for which the Linear Quadratic Regulator (LQR) method was applied. Woo et al. [10] proposed a periodic and continuous momentum management scheme for a space station, using an LQR designed controller for a linearized pitch and roll/yaw decoupled system, limiting its applicability to spacecraft configurations where products of inertia are negligible. Harduvel [11] addressed this gap by designing a frequency-weighted LQR controller for a three-axis coupled system. Similarly to Woo et al. [10], Dang et al. [12] proposed a multistage angular momentum framework, combining open-loop Torque Equilibrium Attitude (TEA) maneuvers, and a feedback stabilization phase using an LQR controller, using the same three-axis coupled linear system as derived in Harduvel [11]. While the LQR offers simplicity in control design, it is not always clear what weightings are most adequate and optimal to address the problem at hand.

More recently, observer-based and adaptive strategies have been investigated [13–16]. Liu et al. [16] demonstrated the possibility of producing an online unified estimation of linearization errors, inertia uncertainties, and the unmodeled aerodynamic torque by including an extended state observer paired with a recursive least squares estimator to separate the estimated quantity into different frequencies. The loop is then closed with an LQR controller. While explicitly considering various sources of uncertainties and disturbances, the inclusion of the observer makes this approach sensitive to sensor noise, and requires careful estimator tuning. The significant amount of tuning parameters make this approach complex to execute, and its adequate performance difficult to guarantee.

Learning-based methods have also been investigated. In 2000, Choi et al. [17] proposed a neural network-based approach. By combining linear controllers parallel to an artificial neural network, the system is able to adapt to unmodeled dynamics and uncertainties, using a Lyapunov based learning law to ensure system stability. Although this approach enhances adaptability, it lacks rigorous robustness guarantees, posing challenges for certification of the space station.

Finally, to guarantee stability under uncertain spacecraft parameters and environmental disturbances, a different research line has explored robust control strategies. Elgersma [18] investigated the application of $\mathcal{H}_\infty$ control to guarantee stability and performance in the presence of disturbances. The work compared an $\mathcal{H}_\infty$ synthesis against classical linear controllers, and it was demonstrated that the former was able to maintain both attitude and angular momentum errors bounded to acceptable ranges, under specific disturbance conditions. While this approach simplifies the specification of control requirements in the frequency domain and provides a more intuitive understanding on how the disturbance interacts with the system, in comparison to LQR tuning, the study relied on a simplified representation of environmental torques.

In fact, all of the above strategies considered that the aerodynamic torque can be approximated by the model provided in Wie et al. [19]. While Harduvel et al. [11] improved this assumption by also including an attitude-dependent contribution of the aerodynamic torque in the linear model, the study still relied on simplified representations of the disturbance acting on the spacecraft. The distinct geometry of Starlab highlights the need for more detailed and realistic disturbance models. The contribution of this paper is to provide an improved aerodynamic torque model, and – by employing this model within the linearized system dynamics – to design a robust $\mathcal{H}_\infty$ controller for ACMM.

This paper is outlined as follows: in section II, the equations of motion of the spacecraft and Control Moment Gyroscope (CMG) dynamics are derived; section III presents the linearization of the equations computed in the previous section; in section IV the aerodynamic torque is analyzed and a linear attitude-dependent contribution is computed; in section V the controller design problem is formulated in the $\mathcal{H}_\infty$ framework; finally, section VI depicts the time-domain simulations for the linear system and the high-fidelity Starlab simulator.

II. Spacecraft Dynamics

In this section, the equations of motion of the spacecraft are derived, starting with the definition of reference frames and kinematic relationships. The rigid-body dynamics are computed from Euler's rotational equations. Finally, the dominant environmental torques acting on the space station are introduced.

A. Reference Frames

To define the equations of motion of the spacecraft and subsequently to design the controller, three main reference frames can be defined as suggested in Figures 1 and 2: the Earth-Centered Inertial (ECI) frame, where the Newtonian laws are valid, the Local Vertical Local Horizontal (LVLH) frame, relative to which the attitude is defined, and finally the Body frame, where mass properties remain approximately constant. The attitude is represented as the Euler angles from the LVLH to the Body frame.

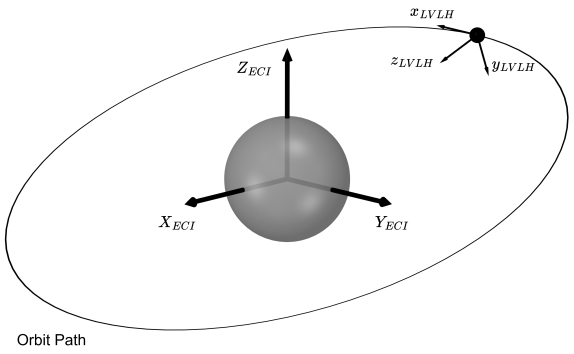

Fig. 1 ECI and LVLH reference frames

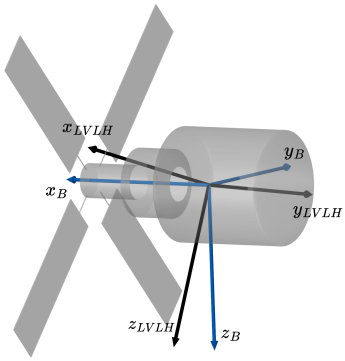

Fig. 2 Body and LVLH reference frames

B. Mission Requirements and Assumptions

In its nominal operational mode, it is required that the space station's body axes remain aligned with the LVLH frame with as little error as possible – within approximately 15°. Secondly, assuming that CMGs will be the actuators utilized to manage this mode, and in order to prevent their saturation, it is required that their angular momentum remains bounded with values in the order of 1000 N m s. An acceptable trade-off between these two opposing constraints needs to be achieved by the controller.

Considering these main mission requirements, some assumptions can be safely made. Firstly, it is assumed that the spacecraft is in a circular orbit with a constant orbital rate ω_0. Secondly, it is considered that there is little deviation of the Body from the LVLH frame. Considering this, the angular rate of the LVLH frame can be given by ${}_N\omega_{N/I} \approx {}_B\omega_{N/I} = \begin{bmatrix} 0 & -\omega_0 & 0 \end{bmatrix}^T$.

C. Rigid Body Dynamics

The equations of motion are derived in the Body frame. As given by Euler's rotational equations, the derivative of the angular momentum of the spacecraft can be given by

$$ {}_B\dot{H} + [{}_B\omega_{B/I}\times] \cdot {}_BH = {}_B\tau \tag{1} $$

Solving the previous equation for ${}_B\dot{H}$ yields

$$ {}_B\dot{H} = -[{}_B\omega_{B/I}\times] \cdot {}_BH + {}_B\tau \tag{2} $$

The previous equation can be rewritten in terms of angular rates as follows:

$$ {}_BJ \cdot {}_B\dot{\omega}_{B/I} = -[{}_B\omega_{B/I}\times] \cdot {}_BJ \cdot {}_B\omega_{B/I} + {}_B\tau \tag{3} $$

In LEO, the main environmental disturbances acting on the spacecraft are the gravity gradient and the aerodynamic torque. This being the case, the total torque acting on the spacecraft is given by

$$ {}_B\tau = {}_B\tau_g + {}_B\tau_a + {}_B\tau_c \tag{4} $$

where ${}_B\tau_g$ and ${}_B\tau_a$ corresponds to the gravity gradient and aerodynamic torques, respectively, and ${}_B\tau_c$ is the control torque imposed by the actuators.

D. Kinematics Equations

The kinematics of the spacecraft are derived by taking the attitude as the integral of:

$$ \dot{T}_{B/N} = [{}_B\omega_{B/N}\times] \cdot T_{B/N} \tag{5} $$

where the angular velocity of the Body frame with respect to the LVLH frame, ${}_B\omega_{B/N}$, is given by:

$$ {}_B\omega_{B/N} = {}_B\omega_{B/I} - {}_B\omega_{N/I} \tag{6} $$

E. CMG Dynamics

The CMG momentum dynamics can be defined as follows:

$$ {}_B\dot{H}_c = -[{}_B\omega_{B/I}\times] \cdot {}_BH_c - {}_B\tau_c \tag{7} $$

where ${}_BH_c$ is the angular momentum of the CMGs.

F. Environmental Torques

As previously mentioned, for a large spacecraft operating in LEO the external disturbance torque acting on the spacecraft can be divided into gravity gradient and the aerodynamic torque.

1. Gravity Gradient Torque

Considering that the space station follows a circular orbit, the gravity gradient torque can be generally approximated by [19]

$$ {}_B\tau_g = 3\omega_0^2 \begin{bmatrix} 0 & -T_{33} & T_{23} \\ T_{33} & 0 & -T_{13} \\ -T_{23} & T_{13} & 0 \end{bmatrix} {}_BJ \begin{bmatrix} T_{13} \\ T_{23} \\ T_{33} \end{bmatrix} \tag{8} $$

where T_{ij} corresponds to the entry in the i-th line and j-th column of the direction cosine matrix from the LVLH to the Body frame, $T_{B/N}$.

2. Aerodynamic Torque

The remaining disturbance torques are dominated by the aerodynamic torque. The aerodynamic torque can be defined as the cross product of the vector defined between the aerodynamic center of pressure and the center of mass of the spacecraft, ${}_Nr_{CoP}$, and the aerodynamic force acting of the center of mass, ${}_NF_a$:

$$ {}_N\tau_a = {}_Nr_{CoP} \times {}_NF_a = {}_Nr_{CoP} \times \left(\frac{1}{2}\rho C_D A V^2 \cdot {}_Nn\right) \tag{9} $$

where ρ represents the atmospheric density, C_D the drag coefficient, A the projected surface normal to the velocity vector, V the norm of the relative velocity of the spacecraft with respect to the atmosphere, and ${}_N n$ is the unitary vector that points in the opposite direction to the velocity. In the LVLH frame the aerodynamic force is approximately aligned with the x-axis, acting in the negative direction. In this way, the disturbance torque caused by the aerodynamic drag in the LVLH frame is

$$ {}_N\tau_a = \begin{bmatrix} 0 \\ -{}_N r_{CoP,z} \cdot \|{}_N F_a\| \\ {}_N r_{CoP,y} \cdot \|{}_N F_a\| \end{bmatrix} \tag{10} $$

Finally, taking the torque in the Body frame yields the following expression:

$$ {}_B\tau_a = T_{B/N} \begin{bmatrix} 0 \\ -{}_N r_{CoP,z} \cdot \|{}_N F_a\| \\ {}_N r_{CoP,y} \cdot \|{}_N F_a\| \end{bmatrix} \tag{11} $$

III. Linear Equations of Motion

The previous system of equations is linearized about the operating point where the Body and LVLH frames are aligned, and $\varphi^*_{B/N} = 0$, ${}_B\omega^*_{B/I} = {}_B\omega_{N/I}$, ${}_B H^*_c = 0$ and $T^*_{B/N} = I$. Assuming little deviation from this operating point, small angle approximations are valid for $\varphi_{B/N} = \begin{bmatrix} \phi & \theta & \psi \end{bmatrix}^T$. This being the case, the following relations can be derived:

A. Linearized Dynamics

To obtain the linearized equations of motion, first, the Jacobian of Equation 3 is computed and evaluated at the operating point:

$$ {}_B\dot{\omega}_{B/N} = [{}_B J]^{-1} \left([({}_B J \cdot {}_B\omega_{N/I})\times] - [{}_B\omega_{N/I}\times] {}_B J \right) {}_B\omega_{B/N} - [{}_B J]^{-1} [({}_B\omega_{N/I})\times] {}_B J {}_B\omega_{N/I} + {}_B\tau_{\text{lin}} \tag{12} $$

Secondly, the total torque needs to be computed as a linear function of the attitude. Firstly, assuming small attitude angles and taking Equation 8, the gravity gradient torque can be rewritten as

$$ {}_B\tau_g = \underbrace{3\omega_0^2 \begin{bmatrix} -{}_B J_{23} \\ {}_B J_{13} \\ 0 \end{bmatrix}}_{{}_B\tau_{g,\text{rest}}} + 3\omega_0^2 \begin{bmatrix} {}_B J_{33} - {}_B J_{22} & {}_B J_{12} & 0 \\ {}_B J_{12} & {}_B J_{33} - {}_B J_{11} & 0 \\ -{}_B J_{13} & -{}_B J_{23} & 0 \end{bmatrix} \begin{bmatrix} \phi \\ \theta \\ \psi \end{bmatrix} \tag{13} $$

The derivation and methodology to obtain a linearized aerodynamic torque contribution will be extensively detailed in section IV, where it is shown that the remaining environmental torque can be represented as the sum of a constant, time-dependent, and attitude-dependent component.

In this way, the rate of change of the angular rate of the spacecraft is given by

$$ \begin{aligned} \dot{\omega}_{B/N} = A_{\omega\varphi}\varphi_{B/N} &+ [{}_B J]^{-1} \left([({}_B J \cdot {}_B\omega_{N/I})\times] - [{}_B\omega_{N/I}\times] {}_B J \right) \omega_{B/N} \\ &+ [{}_B J]^{-1} {}_B\tau_c + [{}_B J]^{-1} \left(-[{}_B\omega_{N/I}\times] {}_B J {}_B\omega_{N/I} + \tau_{g,\text{rest}} + \tau_{a,\text{rest}} \right) \end{aligned} \tag{14} $$

where $\tau_{g,\text{rest}}$ and $\tau_{a,\text{rest}}$ correspond to the attitude-independent contribution of the gravity and aerodynamic torques, and

$$ A_{\omega\varphi} = [{}_B J]^{-1} \left(\frac{\partial \tau_g}{\partial \varphi} + \frac{\partial \tau_a}{\partial \varphi} \right) \tag{15} $$

in which $\frac{\partial \tau_g}{\partial \varphi}$ corresponds to the attitude-dependent component of the gravity gradient from Equation 13 and $\frac{\partial \tau_a}{\partial \varphi}$ to the aerodynamic torque to be derived in the following section.

B. Linearized Kinematics

Assuming small deviations from the nominal attitude, the direction cosine matrix from LVLH to the Body frame can be approximated by $T_{B/N} \approx I - [\varphi_{B/N}\times]$. Therefore, taking Equations (5) and (6) and keeping only first-order terms, the time derivative of the attitude can be given as a linear function of attitude, $\varphi_{B/N}$, and the variation of the angular rate of the spacecraft, ${}_B\omega_{B/N}$:

$$\dot{\varphi}_{B/N} = -[{}_B\omega_{N/I}\times]\varphi_{B/N} + {}_B\omega_{B/N} \tag{16}$$

C. Linearized CMG Dynamics

Considering that, at around the operating point ${}_B\omega_{B/I} \approx {}_B\omega_{N/I}$, the governing equation for the dynamics of the CMGs can be reformulated as

$${}_B\dot{H}_c = -[{}_B\omega_{N/I}\times] \cdot {}_BH_c - {}_B\tau_c \tag{17}$$

D. Linearized System

The previous derivations result in the following linearized plant:

$$\begin{aligned}\begin{bmatrix} \dot{\varphi}_{B/N} \\ {}_B\dot{\omega}_{B/N} \\ {}_B\dot{H}_c \end{bmatrix} &= \begin{bmatrix} -[{}_B\omega_{N/I}\times] & I & 0 \\ A_{\omega\varphi} & [{}_BJ]^{-1}\left([({}_BJ \cdot {}_B\omega_{N/I})\times] - [{}_B\omega_{N/I}\times]{}_BJ\right) & 0 \\ 0 & 0 & -[{}_B\omega_{N/I}\times] \end{bmatrix} \begin{bmatrix} \varphi_{B/N} \\ {}_B\omega_{B/N} \\ {}_BH_c \end{bmatrix} \\ &+ \begin{bmatrix} 0 \\ [{}_BJ]^{-1} \\ -I \end{bmatrix} {}_B\tau_c + \begin{bmatrix} 0 \\ [{}_BJ]^{-1} \\ 0 \end{bmatrix} \underbrace{\left({}_B\tau_{a,rest}(t) + \omega_0^2 \begin{bmatrix} -4 \cdot {}_BJ_{2,3} \\ 3 \cdot {}_BJ_{1,3} \\ {}_BJ_{1,2} \end{bmatrix} \right)}_{{}_B\tau_{d,rest}} \end{aligned} \tag{18}$$

IV. Aerodynamic Torque Modeling

As the most complex external disturbance acting on the spacecraft, a dedicated analysis of the aerodynamic torque is conducted, culminating in a linearized attitude-dependent average torque estimation.

A. Physical Interpretation of Torque Variation

The aerodynamic torque can be divided into two main components: an attitude-dependent part and a periodic part. The latter is induced due to the orbit periodicity and therefore contains most of its power at integer multiples of the orbit rate (Figure 3).

The attitude independent component of the aerodynamic torque is largely driven by atmospheric density variations. One of the contributors to these variations is the diurnal bulge due to the non-uniform solar heating of the atmosphere. This means that over one orbit the spacecraft will pass through a range of atmospheric densities inducing an oscillation of the torque at orbit rate. Additionally, a much slower oscillation is observed in the atmospheric density with a period of 24 hours, which corresponds to a frequency of approximately one sixteenth of the orbit rate. Intuitively, this can be attributed to Earth's rotation which varies the point directly under the Sun throughout the day, inducing the variation of the atmospheric density.

One other quantity that introduces torque variation is the projected area of the spacecraft onto the plane perpendicular to its velocity. Besides attitude, the main contributor to the area variation are the solar arrays. In the nominal operational mode, the latter must be pointed to the Sun, and therefore continuously rotate to perform Sun tracking. It is observed that the variation of the projected area follows the absolute value of a sinusoid at orbit rate. When expressing this relation without the absolute value operator, this oscillation can be represented as sinusoidal terms at twice the orbital rate, since the absolute value operation halves the period of a sinusoidal signal. Another more complex effect of the movement of the solar arrays together with attitude is the shift of the aerodynamic center of pressure.

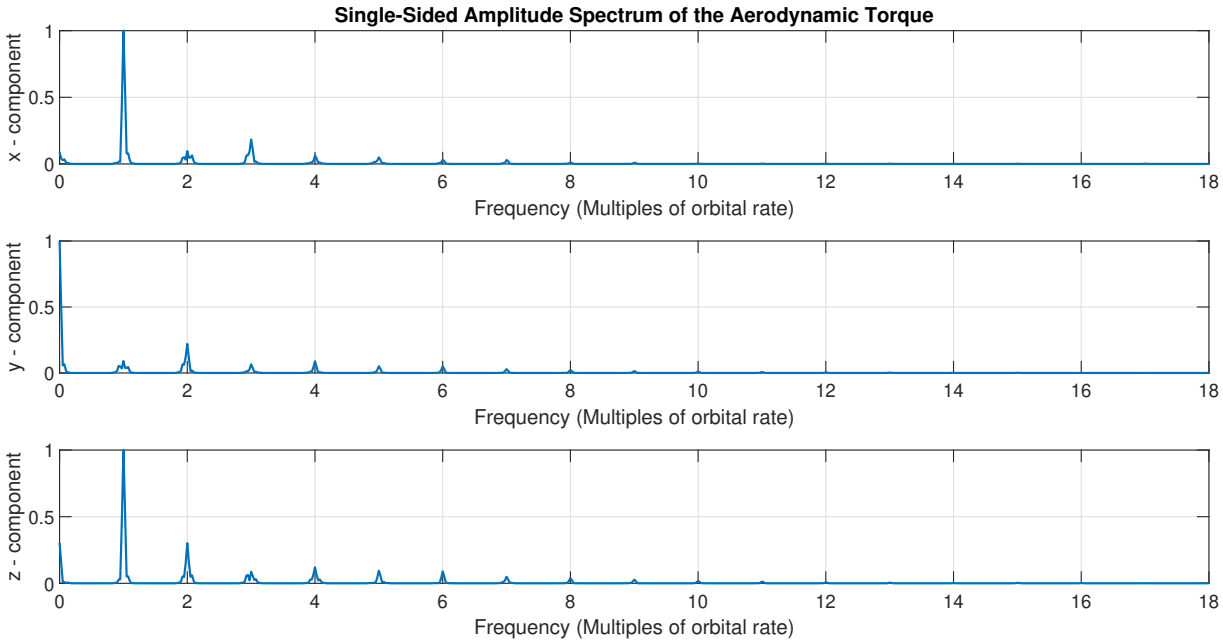

Fig. 3 Normalized single-sided amplitude spectrum of the aerodynamic torque when the body frame is aligned with the LVLH frame

B. Average Torque Estimation Methodology

The above mentioned considerations highlight the complexity of capturing the aerodynamic disturbance in a detailed and accurate manner. While the oscillatory behavior of the torque is important for high-fidelity modeling, for control design purposes it is often more suitable to focus on the average contribution of the disturbance. By considering the mean torque, all of the sinusoidal contributions average out to a bias whose relation to attitude can be more easily identified.

To achieve this, the aerodynamic torque was simulated for an integer number of orbits for constant attitude. A grid of different combinations of attitude was selected based on expected operational conditions of the system, and the average torque over 16 orbits was computed to represent the mean aerodynamic torque corresponding to each attitude configuration. The choice of 16 orbits ensures that the averaging captures at least one full period of all relevant oscillatory components – integer multiples of the orbital rate and at one sixteenth of the orbital rate, which corresponds to Earth's rotation period.

Once this data was obtained, and after observing a linear trend between small attitude angles and the average aerodynamic torque, a linear relationship was identified using the Least Squares (LS) method. Denoting the averaged torque as $\bar{\tau}_a$ and $M_\varphi \in \mathbb{R}^{3\times4}$ as the linear time-invariant matrix to be estimated, a linear model of the following form is assumed:

$$ {}_B\bar{\tau}_a = M_\varphi \begin{bmatrix} 1 \\ \varphi_{B/N} \end{bmatrix} \tag{19} $$

By appending all regression vectors, $\begin{bmatrix} 1 & \varphi_{B/N} \end{bmatrix}^T$, in a matrix $\Theta \in \mathbb{R}^{N\times4}$ and the corresponding average torques in matrix $T \in \mathbb{R}^{N\times3}$, the model can be rewritten as:

$$ T = \Theta M_\varphi^T \tag{20} $$

The least-squares estimate of M_φ is obtained by minimizing the convex cost function [20]:

$$ C = \left(T - \Theta M_\varphi^T\right)^T \left(T - \Theta M_\varphi^T\right) \tag{21} $$

This convex cost function, C, is minimized when

$$M_\varphi = \left(\Theta^T \Theta\right)^{-1} \Theta^T T \tag{22}$$

C. Average Torque Estimation Results and Validation

All the aerodynamic torque results depicted in this section are presented for the nominal configuration of the station in a normalized form: each component is divided by the maximum mean torque magnitude across all datasets, and the Euler angles are normalized to span the range of -1 to 1. In this way the relative magnitude between plots is preserved. Additionally, the torque model identification was performed for a Right Ascension of the Ascending Node (RAAN) of 120°, for which the expected aerodynamic torque magnitude is approximately highest.

The comparison between the averaged aerodynamic torque obtained from the data and the linear approximation shows that the proposed least-squares fit it able to capture the main dependence of the torque on the spacecraft attitude. A coefficient of determination, R^2, of 0.92, 0.99 and 0.91 was obtained for the x, y, and z-axes, respectively. This indicates that a significant portion of the variance in the aerodynamic torque is explained by the linear model, therefore confirming that the underlying trend can be approximated in this form. Further inspection of Figures 4 to 6 reveals that there is a bias of small magnitude – when compared to the norm of the mean aerodynamic torque – between the estimated and real mean torques, particularly for the y-axis component of the torque when $\theta = 0$ and $\psi = 0$ and when $\phi = 0$ and $\theta = 0$. Nevertheless, since the general trend of the variation with attitude seems to be sufficiently accurate, and because the offset does not enter the linear model dynamics, it is considered that the accuracy of the proposed approximation is suitable for controller design.

Additionally, Figure 4 suggests that a pure roll rotation does not contribute as strongly to the variation of the average torque when compared to pitch and yaw. This outcome is expected under the specified operational conditions, as this rotation does not significantly vary the area perpendicular to the velocity vector, and therefore has a smaller effect on the aerodynamic torque.

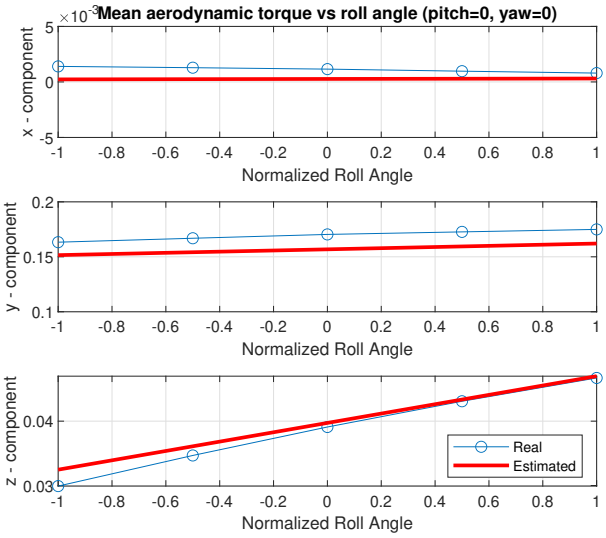

Fig. 4 Normalized real average aerodynamic torque comparison to the estimated torque with respect to roll, for RAAN= 120°

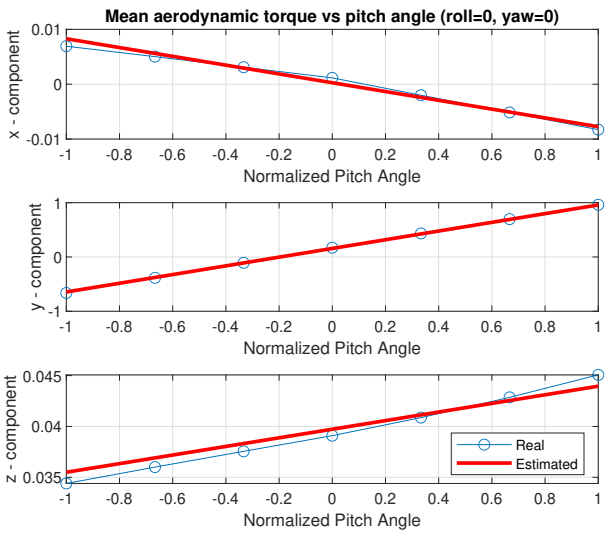

Fig. 5 Normalized real average aerodynamic torque comparison to the estimated torque with respect to pitch, for RAAN= 120°

Further validation of the obtained average aerodynamic torque model was conducted, by comparing the real mean torque with the estimated torque for a combination of different attitudes (Figure 7). While the estimation on the y-axis only slightly deviated from the real mean aerodynamic torque with an error up to approximately 20%, the relative error is greater for the x and z-axes reaching magnitudes as high as 40%. However, it is clear that the magnitude of the torque for the roll and yaw axis is much less significant than the contribution of the torque around the pitch axis by a factor of $10 - 100$. For this reason, it is expected that the performed approximation is sufficiently accurate in representing aerodynamic torque attitude dependency.

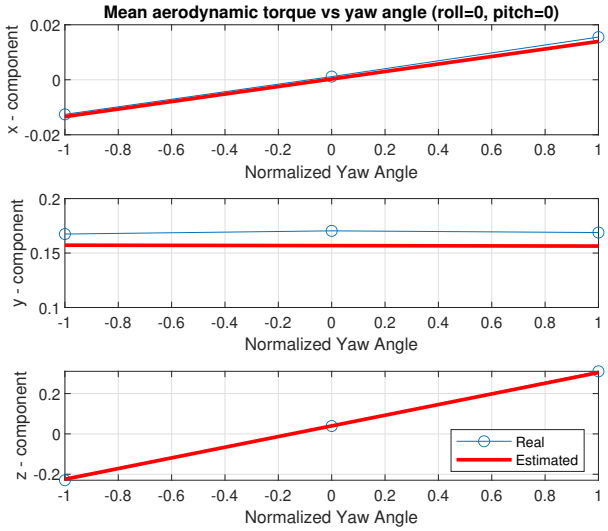

Fig. 6 Normalized real average aerodynamic torque comparison to the estimated torque with respect to yaw, for RAAN= 120°

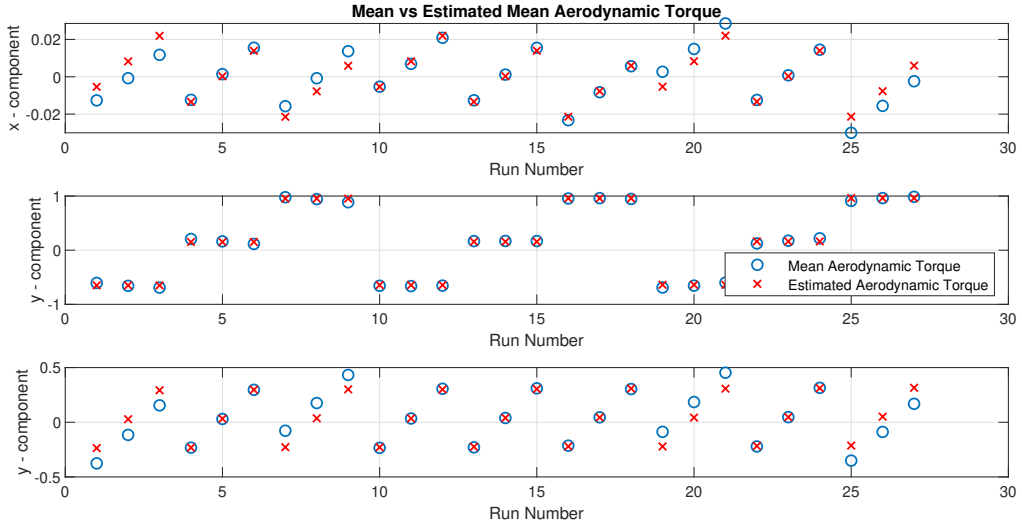

Fig. 7 Normalized real average aerodynamic torque comparison to the estimated torque, for RAAN= 120°

The same procedure should be followed for the identification of an aerodynamic torque model for different RAAN and space station configurations.

V. Controller Design

$\mathcal{H}_\infty$ synthesis is a robust control design method that formulates the minimization of the worst-case amplification from exogenous inputs – references, noise, disturbances – to controlled outputs – tracking error, control effort. The $\mathcal{H}_\infty$-norm of a system $H(s)$ is defined as

$$\|H(s)\|_\infty = \max_{\omega \in \mathbb{R}} \bar{\sigma}(H(j\omega)) \tag{23}$$

where $\bar{\sigma}$ corresponds to the maximum singular value. Minimizing this norm ensures that the largest possible gain from inputs to outputs is bounded across all frequencies, which translates into guaranteed robustness and performance.

In practice, performance specifications are included in the controller synthesis setup by defining weighting filters that shape the closed-loop transfer function. The main challenge in this approach is to select weighting filters that translate the requirements into magnitude bounds over frequency, while trading off system constraints and robustness.

A. Control Requirements

The main performance requirement is that attitude and CMG angular momentum must be kept bounded in the presence of disturbances and modeling uncertainties. To achieve this, several practical constraints must be accounted for in the controller design. Firstly, the spacecraft exhibits flexible structural modes that can be undesirably excited by control actions at high frequencies. These dynamics must be attenuated by minimizing controller action for frequencies where the flexible modes are expected (above 0.05 Hz $\approx$ 0.3 rad/s). Secondly, while the disturbance is expected to range from DC up to eight times the orbit rate, its persistent component is the one responsible for CMG momentum accumulation, making low frequencies the most critical range to ensure that the main performance requirement is achieved. In other words, oscillations in the time response of attitude and CMG angular momentum are permitted as long as they remain within acceptable bounds in the order of 1000 N m s.

B. Problem Formulation

The $\mathcal{H}_\infty$ problem is generally formulated based on the definition of a generalized plant, P, which collects the full spacecraft dynamics from exogenous inputs to performance outputs. In the proposed ACMM problem, the exogenous input, d, corresponds to the non-attitude dependent component of the disturbance torque, and the performance output, p, is chosen to include attitude and CMG angular momentum errors as well as the control torque input. In this way, P can be defined as follows:

$$P = \begin{cases} \dot{x} = Ax + B_1 d + B_2 u \\ p = C_1 x + D_{11} d + D_{12} u \\ y = C_2 x + D_{21} d + D_{22} u \end{cases} \tag{24}$$

where $x = \begin{bmatrix} \varphi_{B/N} & {}_B\omega_{B/N} & {}_BH_c \end{bmatrix}^T$ is the state vector, $d = {}_B\tau_{d,rest}$ is the exogenous input, $u = {}_B\tau_c$ is the control input, $p = \begin{bmatrix} \varphi_{B/N} & {}_BH_c & {}_B\tau_c \end{bmatrix}^T$ is the performance output vector, and $y = \begin{bmatrix} \varphi_{B/N} & {}_B\omega_{B/N} & {}_BH_c \end{bmatrix}^T$ is the measurable output vector. Matrices A, B_1, B_2, C_1, C_2, D_{11}, D_{12}, D_{21}, D_{22} are given by

$$\begin{gathered} A = \begin{bmatrix} -[{}_B\omega_{N/I}\times] & I & 0 \\ A_{\omega\varphi} & [{}_BJ]^{-1}\left([({}_BJ \cdot {}_B\omega_{N/I})\times] - [{}_B\omega_{N/I}\times]{}_BJ\right) & 0 \\ 0 & 0 & -[{}_N\omega_{N/I}\times] \end{bmatrix} \quad B_1 = \begin{bmatrix} 0 \\ [{}_BJ]^{-1} \\ 0 \end{bmatrix} \\ B_2 = \begin{bmatrix} 0 \\ [{}_BJ]^{-1} \\ -I \end{bmatrix} \quad C_1 = \begin{bmatrix} I & 0 & 0 \\ 0 & 0 & I \\ 0 & 0 & 0 \end{bmatrix} \quad C_2 = \begin{bmatrix} I & 0 & 0 \\ 0 & I & 0 \\ 0 & 0 & I \end{bmatrix} \quad D_{11} = \begin{bmatrix} 0 \\ 0 \\ 0 \end{bmatrix} \quad D_{12} = \begin{bmatrix} 0 \\ 0 \\ I \end{bmatrix} \quad D_{21} = \begin{bmatrix} 0 \\ 0 \\ 0 \end{bmatrix} \quad D_{22} = \begin{bmatrix} 0 \\ 0 \\ 0 \end{bmatrix} \end{gathered} \tag{25}$$

The goal is to design K such that $u = Ky$ (Figure 8) and that the disturbance d is rejected across its dominant frequencies. This problem is generally denominated as the 'two-block problem'. Let G be the system from control input, u, to measurable output, y, and G_d the dynamics from the disturbance input d to the measurable output, y. Defining the output sensitivity function as $S = (I + GK)^{-1}$, the closed loop transfer functions of the system can be defined as

$$p = \begin{bmatrix} y \\ u \end{bmatrix} = \begin{bmatrix} SG_d \\ KSG_d \end{bmatrix} d \tag{26}$$

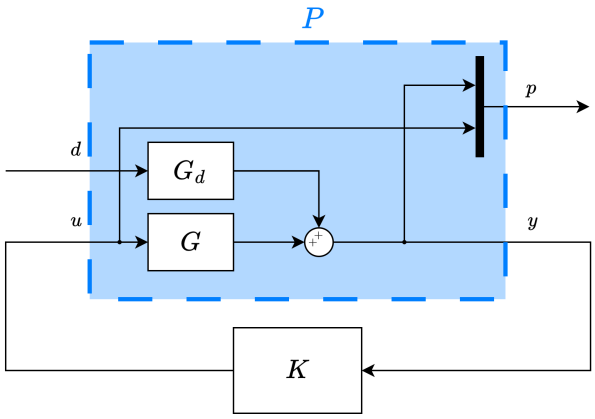

Fig. 8 Generalized plant P with the positive feedback controller K

Before shaping the transfer functions, and because the physical variables have different orders of magnitude, scaling is introduced to normalize the system. This ensures that both attitude and CMG angular momentum deviations can be treated on a comparable basis and weighting filters can be defined in similar magnitude ranges. To achieve this, static gains, V, are introduced and selected as the maximum acceptable values for each variable, as proposed in [21].

The performance requirements are then incorporated by means of weighting filters. In this way, W is defined in the frequency domain, and consists of the upper bound of the transfers from w to z. The overall proposed system for controller synthesis is depicted in Figure 9. The role of the controller is to then minimize the transfer from weighted disturbance input, w, to the weighted performance output, z, therefore ensuring disturbance rejection.

Therefore, the closed-loop transfer functions from w to z can be defined as

$$z = \begin{bmatrix} W_\varphi V_\varphi^{-1} & 0 & 0 \\ 0 & W_H V_H^{-1} & 0 \\ 0 & 0 & W_u V_u^{-1} \end{bmatrix} \begin{bmatrix} SG_d \\ KSG_d \end{bmatrix} V_d w \tag{27}$$

where $W, V \in \mathbb{R}^{3\times3}$ are diagonal matrices, such that the choice of the weighting filters is more easily interpreted from a physical perspective and can be made based on their relative importance rather than on the physical units or absolute magnitudes of the plant variables.

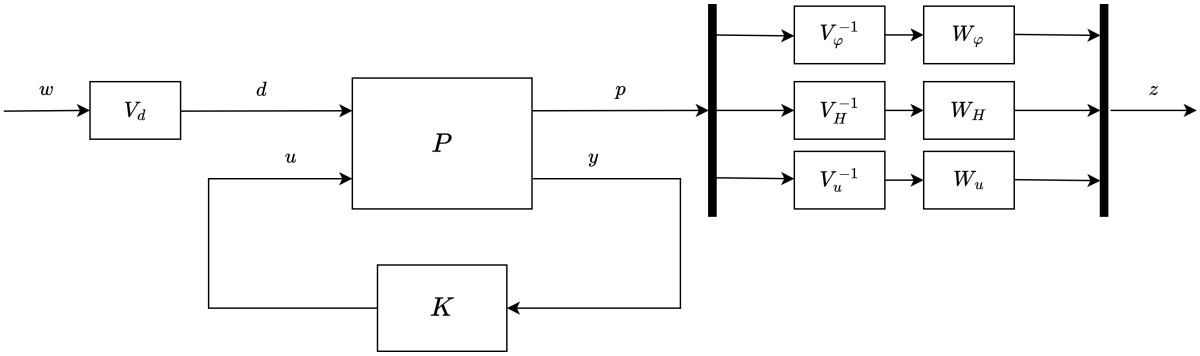

Fig. 9 Closed loop for control design

C. Definition of Weighting Filters

Before defining the weighting filters it is crucial to revisit the disturbance characteristics. As previously mentioned and derived, the non-modeled disturbance effects can be separated into a bias – arising from the gravity gradient and aerodynamic torques offset, and the gyroscopic bias torque – and a time varying component exhibiting a harmonic structure at integer multiples of the orbital frequency and of the Earth's rotation frequency. Considering that these

harmonic terms are most significant up to twice the orbital rate, the goal is to minimize the closed-loop transfer function gain from w to z for DC, ω_0, $2\omega_0$ and at approximately $\omega_0/16$. Additionally, it is necessary to minimize control effort at frequencies where unmodeled flexible modes are expected (above approximately 0.3 rad/s).

Taking these specifications into consideration while also ensuring minimum robustness margins – 3 dB gain margin, 30° phase margin, and 0.5 disk margin – resulted in the definition of the weighting filters specified in the following figures, where their inverses represent an upper bound of the closed-loop transfer function of the scaled system. As an initial approach, the magnitude of the transfer functions was chosen based on the physical expected maximum magnitude of the performance output, p, when considering a worst-case magnitude for the disturbance, d. Design iterations were made on this initial design specification to maximize robustness.

1. Nominal Space Station Configuration

The control design and definition of the weighting filters for $\mathcal{H}_\infty$ synthesis were first carried out for the nominal space station configuration. The closed-loop transfer functions from disturbance to control torque (Figure 12) illustrate the imposed requirements during design, where lower magnitudes are enforced at higher frequencies to limit control effort and avoid excitation of flexible modes. Furthermore, the main physical constraint of the ACMM problem is emphasized by the inability of driving both the attitude and momentum closed-loop transfer functions to zero for low frequencies (Figures 10 and 11). Additionally, during the tuning process, it was observed that the attitude magnitude could not be reduced uniformly over frequency any further, even when placing more emphasis on attitude than on momentum error minimization. This is due to the fact that, regardless of the synthesized controller, the fixed environmental torque coefficients, $A_{\omega\varphi}$ determine the required attitude offset to compensate the DC disturbance torques. For this case in particular, the high magnitude of the maximum singular value of the closed-loop transfer from disturbance to attitude at low frequencies – which corresponds to the dynamics from disturbance to roll – can be attributed to the mass distribution of the station. For this configuration, ${}_BJ_{1,1}/{}_BJ_{3,3} = 0.68$, and ${}_BJ_{2,2}/{}_BJ_{3,3} = 1.00$. Recalling Equation (13), it is possible to infer that, because the difference ${}_BJ_{3,3} - {}_BJ_{2,2}$ is extremely small, the gravity gradient torque acting on the roll axis is practically eliminated. Since the roll motion – which is the one capable of counteracting the aerodynamic torque acting in yaw – cannot generate sufficient restoring torque, there is a loss of control effectiveness for the roll/yaw dynamics.

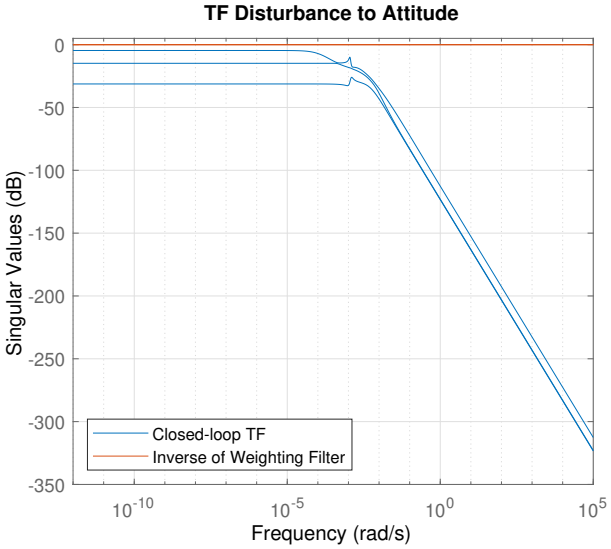

Fig. 10 Closed-loop transfer function from disturbance to attitude

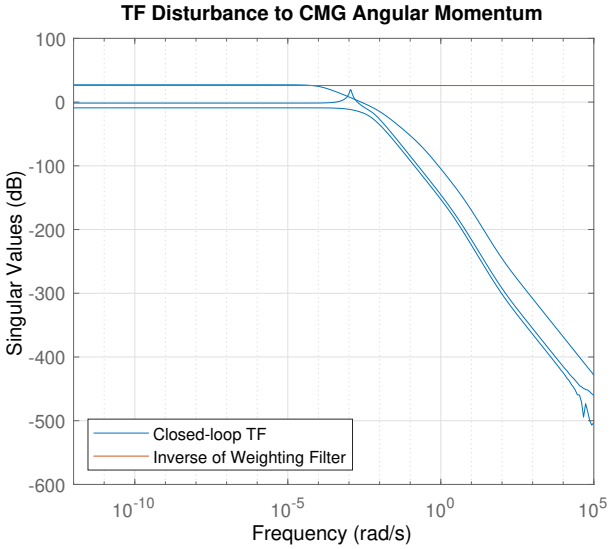

Fig. 11 Closed-loop transfer function from disturbance to CMG angular momentum

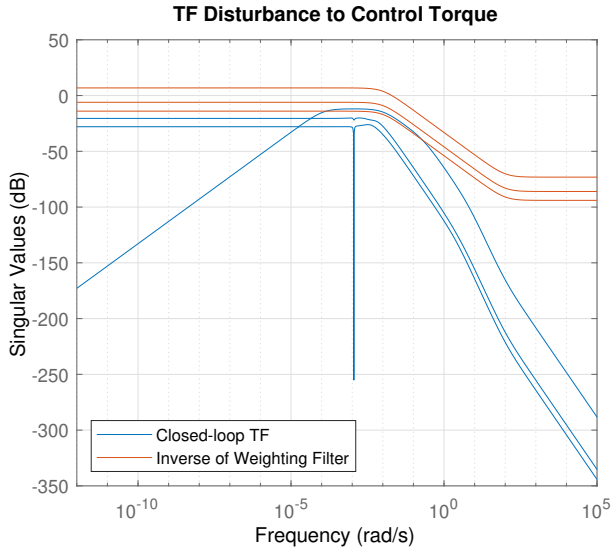

Fig. 12 Closed-loop transfer function from disturbance to control torque

2. Nominal Space Station Configuration with Modified Inertia

To validate the lack of roll/yaw gravity gradient control authority for the nominal space station configuration, ${}_{B}J_{3,3}$ was scaled by a factor of 1.6, such that the ${}_{B}J_{3,3} - {}_{B}J_{2,2}$ term was increased, while preserving the physical consistency of the inertia matrix. Figures 13 to 15 show the closed-loop transfer functions for both the nominal and modified inertia systems when shaped with the same weighting filters. By examining these results, it becomes clear that increasing the gravity gradient allows the controller to achieve lower steady-state levels both in attitude deviation and angular momentum error.

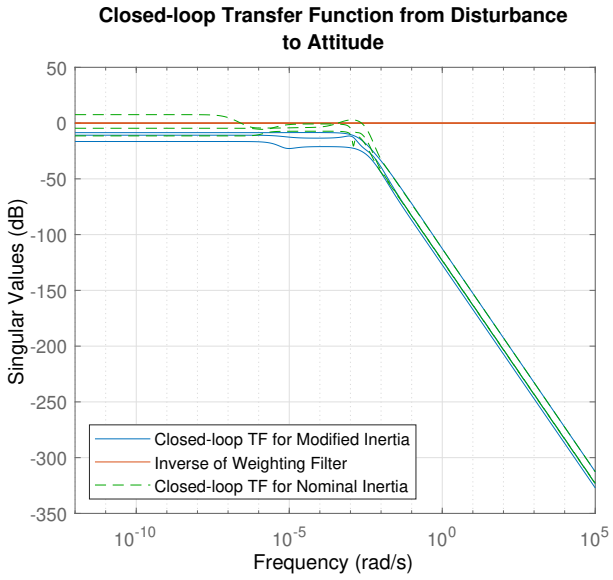

Fig. 13 Closed-loop transfer functions from disturbance to attitude, considering the nominal and modified inertia

Fig. 14 Closed-loop transfer functions from disturbance to CMG angular momentum, considering the nominal and modified inertia

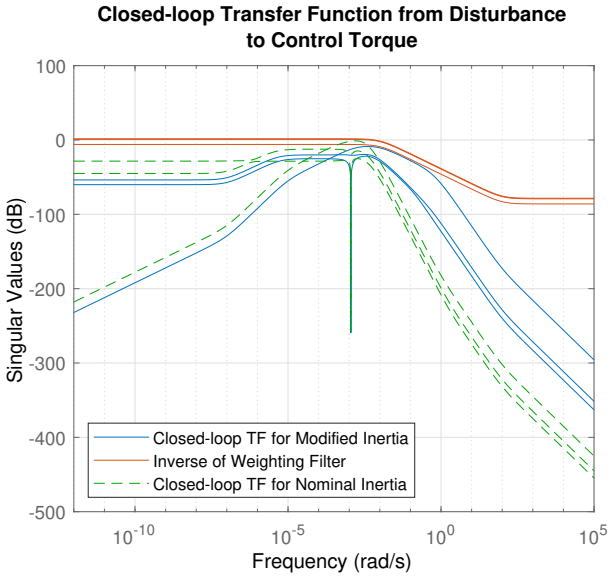

Fig. 15 Closed-loop transfer functions from disturbance to control torque, considering the nominal and modified inertia

3. Space Station Configuration with Docked Vehicle

In addition to the nominal case, a second space station configuration was considered where a vehicle is docked. In this case, ${}_BJ_{1,1}/{}_BJ_{3,3} = 0.79$, and ${}_BJ_{2,2}/{}_BJ_{3,3} = 1.54$, so it is expected that there is enough gravity gradient torque authority. Additionally, because the expected steady-state pitch angle (θ^*) is lower than $-15°$ the system was linearized as defined in the Appendix around an attitude of $\varphi^*_{B/N} = \begin{bmatrix} 0 & \theta^* & 0 \end{bmatrix}^T$. Therefore, the output and state of the linear system now corresponds to the attitude error $\Delta\varphi = \varphi_{B/N} - \varphi^*_{B/N}$.

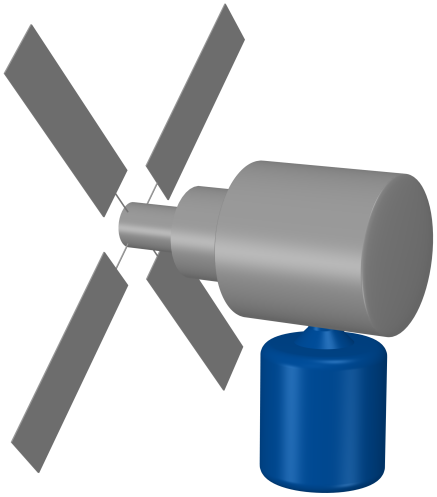

Fig. 16 Starlab configuration with docked vehicle

Figures 17 to 19 show the closed-loop transfer functions from disturbance to attitude, CMG angular momentum and control torque, after weighting filter tuning. It is once again confirmed that, for a sufficient magnitude of ${}_BJ_{3,3} - {}_BJ_{2,2}$, it is possible to drive the attitude and momentum errors to a maximum magnitude of approximately 1 for the scaled system. This means that the design is compliant with the maximum expected/desired magnitudes for each of the performance

variables defined by the static gains, V.

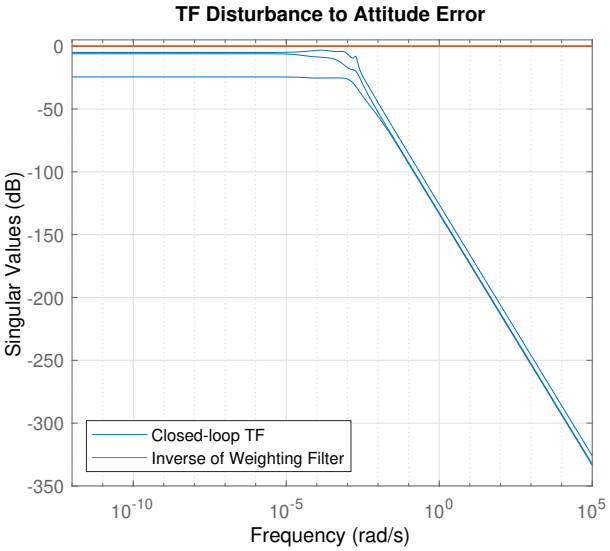

Fig. 17 Scaled closed-loop transfer function from disturbance to the attitude error for the space station configuration with the docked vehicle

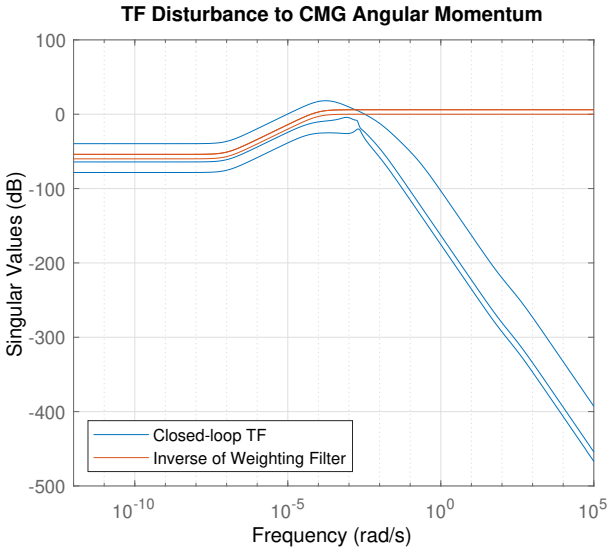

Fig. 18 Scaled closed-loop transfer function from disturbance to the CMG angular momentum for the space station configuration with the docked vehicle

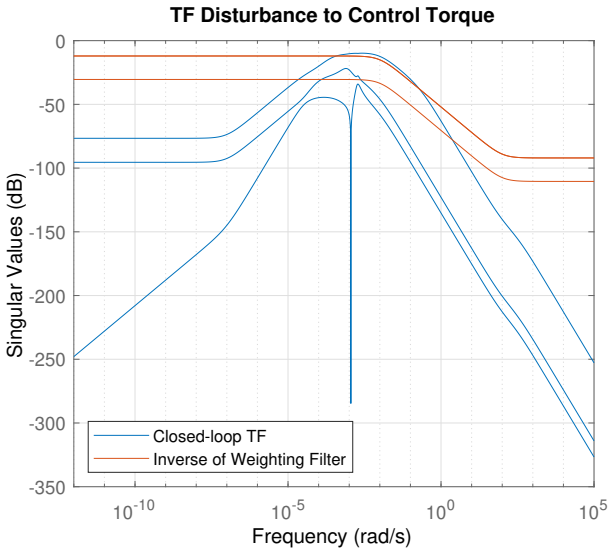

Fig. 19 Scaled closed-loop transfer function from disturbance to the control torque for the space station configuration with the docked vehicle

VI. Simulation Results

This section presents the time-domain simulation results using both the linear model – subjected to a realistic disturbance profile and including the estimated attitude-dependent aerodynamic torque model while assuming constant inertia – and a high-fidelity simulator of the space station that accounts for inertia variations due to solar array motion and includes a more detailed model of the environmental disturbance torques. The goal is to assess whether the control goals – disturbance rejection, bounded momentum buildup, and limited control effort – are achieved under representative operating conditions. The results are shown for the space station configuration with a docked vehicle, and are normalized with respect to the maximum magnitude defined in the static gains, V. Since these gains were established based on the maximum desired steady-state values of the performance outputs, normalized steady-state responses with a magnitude below one indicate that the control requirements are satisfied.

A. Linear Model Simulation Results

Firstly, the response of the linear model is simulated using the constant nominal spacecraft inertia and estimated aerodynamic torque model, when the system is perturbed with the disturbance profile depicted in Figure 20. The disturbance profile was generated from the attitude-independent component of the environmental torques, ${}_B\tau_{d,rest}$, where the aerodynamic contribution was obtained from data corresponding to a fixed attitude equal to the operating point about which the system was linearized.

Figures 21 to 23 showcase the closed-loop time responses of the scaled performance outputs. First, it can be observed that the system produces a stable response when subjected to the given disturbance profile. Secondly, it is shown that the magnitude of all normalized performance outputs mostly remains below an absolute value of 1 for steady-state, confirming that the attitude, angular momentum and control torque requirements are fulfilled. Third, as desired, the angular momentum is successfully driven to oscillate around 0 as enforced by the low frequency weighting filter definition. All in all, the system demonstrates robustness to the imposed disturbance torque.

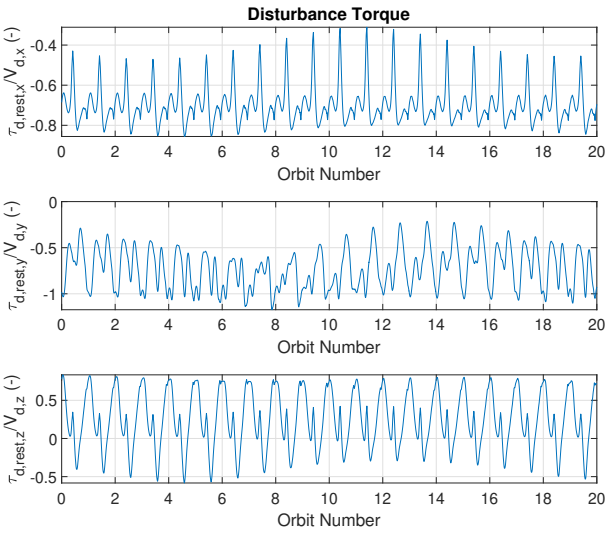

Fig. 20 Normalized attitude independent aerodynamic torque disturbance profile

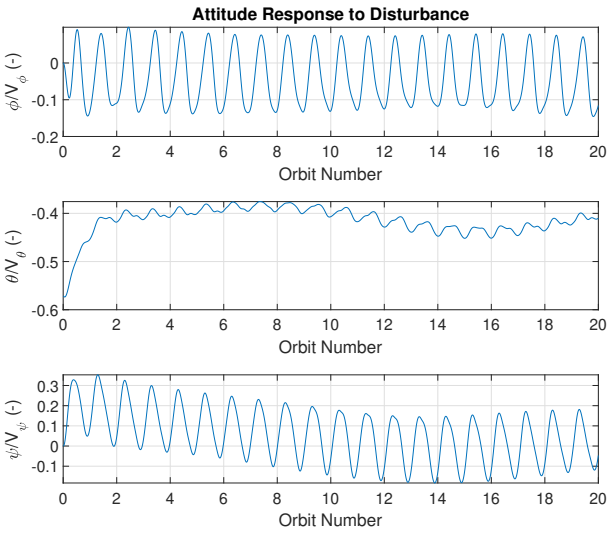

Fig. 21 Time response of the normalized attitude to disturbance for the space station configuration with the docked vehicle

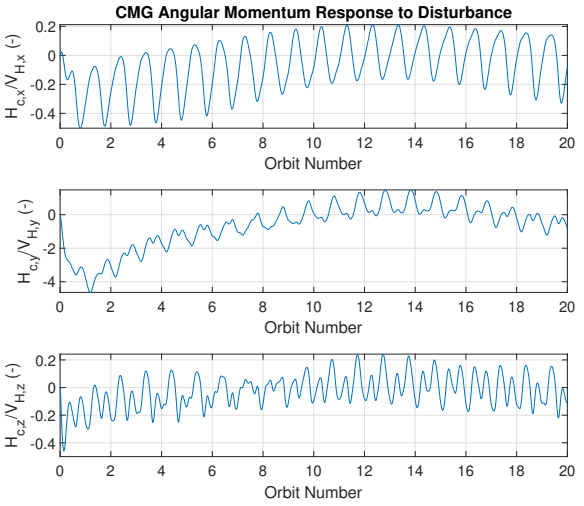

Fig. 22 Time response of the normalized CMG angular momentum to disturbance for the space station configuration with the docked vehicle

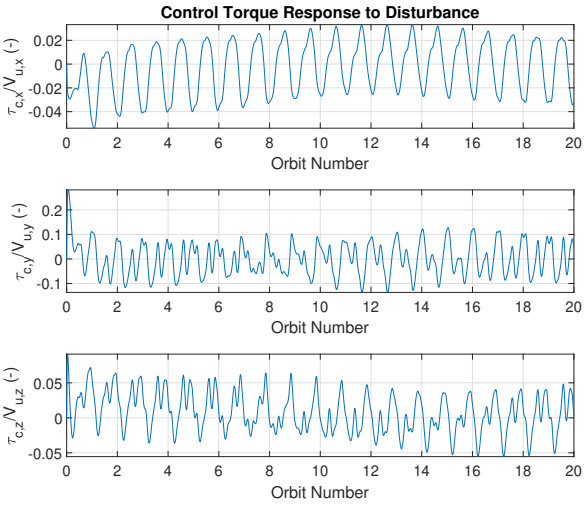

Fig. 23 Time response of the normalized control torque to disturbance for the space station configuration with the docked vehicle

B. High-fidelity Simulator Results

In this section, the time-domain results from the high-fidelity simulator are presented. The simulations consider variations in inertia due to solar array motion and environmental torques, which are computed based on the spacecraft's geometry (attitude and solar arrays), as well as the surrounding orbital environmental (orbit geometry, including the station's relative position to the Sun).

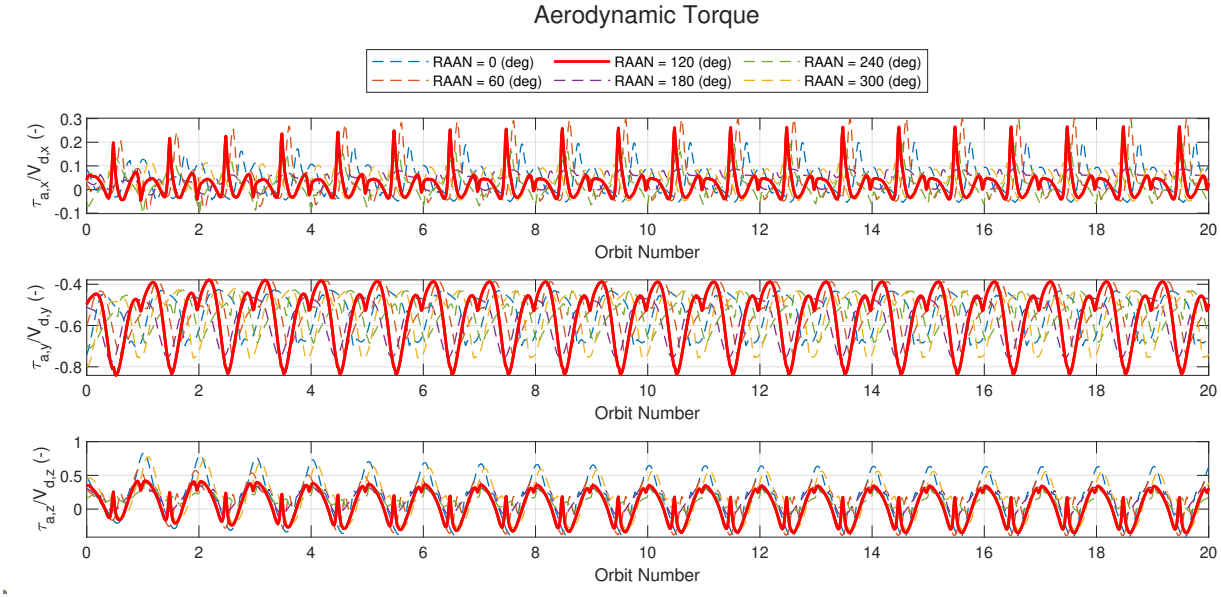

Fig. 24 Simulator-generated aerodynamic torque over time for the space station configuration with the docked vehicle

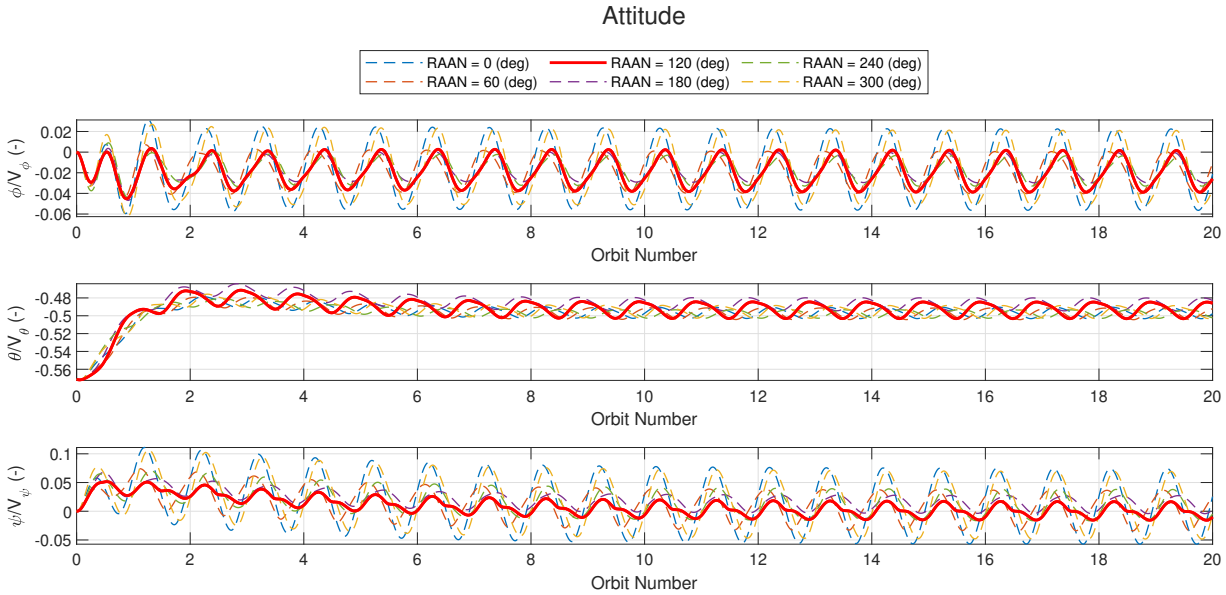

Fig. 25 Simulator-generated time response of the normalized attitude to disturbance for the space station configuration with the docked vehicle

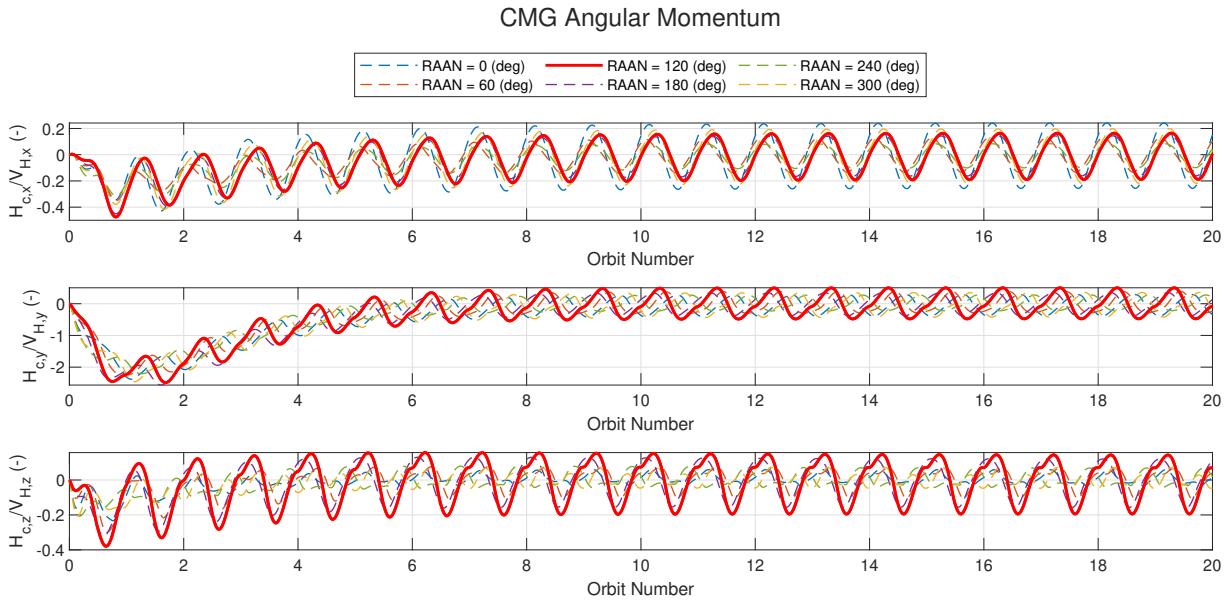

Fig. 26 Simulator-generated time response of the normalized CMG angular momentum to disturbance for the space station configuration with the docked vehicle

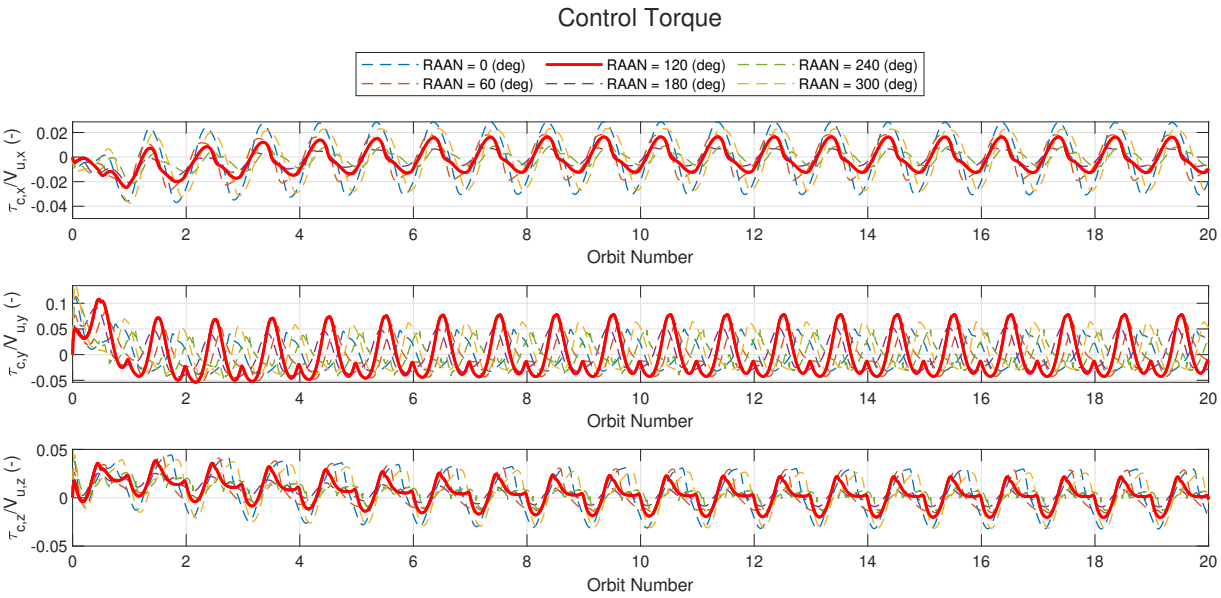

Fig. 27 Simulator-generated time response of the normalized control torque to disturbance for the space station configuration with the docked vehicle

Figures 24 to 27 depict the high-fidelity simulator results throughout time, for a set of RAANs spanning the entire $0° - 360°$ range, sampled at $60°$. The goal was to assess the performance of the controller for the designed RAAN and to establish a range of RAANs for which the controller is valid.

Although the systems were not perturbed with the exact same disturbance torques, the closed-loop performance between the linear system and the high-fidelity simulator can be compared. Firstly, it can be seen that the orders of magnitude of each of the performance outputs match between models, validating the linear model. Additionally, it should be noted that the steady-state offset around which the attitude oscillates is approximately the same between models. The fact that the nonlinear simulation achieves a stable response following that same offset – which is established by minimizing the total contribution of the gravity gradient and aerodynamic torques – validates the aerodynamic torque model.

Furthermore, it was found that the controller was able to stabilize the system for all the considered RAANs, without excitation of the high-frequency structural flexible modes. The performance outputs also remained within suitable bounds, i.e. a normalized magnitude below 1 for steady-state, for all scenarios. This can be explained by the robustness of the designed system that accounts for model mismatch. One other explanation stems from the fact that the RAAN for which the controller was designed for ($120°$) has an overall higher magnitude when compared to other RAANs. This is preferable to underestimating this torque since, in this way, the controller will be designed to handle a worst-case scenario.

VII. Conclusions

The present work addressed the problem of ACMM for Starlab, by modeling the aerodynamic torque and designing a robust disturbance-rejection controller, based on the $\mathcal{H}_\infty$ synthesis framework. The controller was designed to ensure robustness against modeling uncertainties and environmental disturbances, while maintaining acceptable attitude pointing and CMG angular momentum magnitudes.

The analysis showed that, within the operation envelope of the mission, the aerodynamic torque can be accurately approximated as a linear function of the attitude for a given RAAN. It was also found that the nominal space station configuration provides limited gravity-gradient control authority, as the small difference between $J_{3,3}$ and $J_{2,2}$ prevents sufficient compensation of the aerodynamic torque for the roll/yaw motion. This results in reduced controllability and significant attitude and angular momentum errors. A more asymmetric configuration, corresponding to the station with a radially docked vehicle, confirmed this behavior by decreasing these errors for the same disturbance input magnitude.

The controller performance was verified for this last configuration through time-domain simulations using both the

linearized model and a high-fidelity nonlinear simulator. The results confirmed the effectiveness of the proposed $\mathcal{H}_\infty$ controller in rejecting realistic disturbances, and in maintaining satisfactory attitude and momentum levels. Furthermore, the controller did not excite the unmodeled flexible modes, demonstrating adequate robustness to structural dynamics.

To assess robustness with respect to orbital geometry, simulations were also performed for different RAANs around the nominal design point. The results revealed that the controller still performed adequately for the other scenarios, showcasing the robustness of the closed-loop system to model uncertainties. Future work could focus on extending this approach by development of a parameter-dependent representation of the aerodynamic torque – explicitly accounting for its variation with RAAN and including solar array angles measurements – so that the control problem can be reformulated within a linear parameter-varying framework. This would enable the design of a single controller with improved adaptability and robustness across the full range of orbital conditions.

References

[1] Zhu, M., and Xu, S., "Stability-based SDRE controller for spacecraft momentum management," *Acta Astronautica*, Vol. 89, 2013, pp. 71–82. https://doi.org/10.1016/j.actaastro.2013.03.026.

[2] Parlos, A., and Sunkel, J., "Adaptive attitude control and momentum management for large-angle spacecraft maneuvers," *Journal of Guidance, Control, and Dynamics*, Vol. 15, No. 4, 1992, pp. 1018–1028. https://doi.org/10.2514/3.20937.

[3] Funk, G. E., and Stephenson, R. M., "On-Orbit Shuttle/Mir Mated Reaction Control System and Crew Load Analyses," *Journal of Spacecraft and Rockets*, Vol. 37, No. 4, 2000, pp. 515–518. https://doi.org/10.2514/2.3593.

[4] Kehr, J., "The International Starlab Commercial Space Station Concept," *Journal of Space Operations*, 2024. URL https://www.opsjournal.org/DocumentLibrary/Uploads/final_The%20International%20STARLAB%20Space%20Station%20Concept%20(Autosaved).pdf.

[5] Kimoto, Y., Yano, K., Ishizawa, J., Miyazaki, E., and Yamagata, I., "Passive Space-Environment-Effect Measurement on the International Space Station," *Journal of Spacecraft and Rockets*, Vol. 46, No. 1, 2009, pp. 22–27. https://doi.org/10.2514/1.31851.

[6] Wie, B., Byun, K. W., Warren, V. W., Geller, D., Long, D., and Sunkel, J., "New approach to attitude/momentum control for the Space Station," *Journal of Guidance, Control, and Dynamics*, Vol. 12, No. 5, 1989, pp. 714–722. https://doi.org/10.2514/3.20466.

[7] Jules, K., McPherson, K., Hrovat, K., Kelly, E., and Reckart, T., "A status report on the characterization of the microgravity environment of the International Space Station," *Acta Astronautica*, Vol. 55, No. 3, 2004, pp. 335–364. https://doi.org/https://doi.org/10.1016/j.actaastro.2004.05.057.

[8] Newman, D., Amir, A., and Beck, S., "Astronaut-Induced Disturbances to the Microgravity Environment of the Mir Space Station," *Journal of Spacecraft and Rockets*, Vol. 38, No. 4, 2001, pp. 578–583. https://doi.org/10.2514/2.3719.

[9] Sorokin, I., and Markov, A., "Utilization of Space Stations: 1971-2006," *Journal of Spacecraft and Rockets*, Vol. 45, No. 3, 2008, pp. 600–607. https://doi.org/10.2514/1.32772.

[10] Woo, H., Morgan, H., and Falangas, E., "Momentum management and attitude control design for a Space Station," *Journal of Guidance, Control, and Dynamics*, 1988. https://doi.org/10.2514/3.20264.

[11] Harduvel, J., "Continuous momentum management of earth-oriented spacecraft," *Journal of Guidance, Control, and Dynamics*, Vol. 15, No. 6, 1992, pp. 1417–1426. https://doi.org/10.2514/3.11405.

[12] Dang, Q., and Jin, L., "Multistage Angular Momentum Management for Space Station Attitude Control," *IEEE Access*, Vol. 6, 2018, pp. 15075–15086. https://doi.org/10.1109/ACCESS.2018.2811759.

[13] Liu, P., "Partial state based attitude control and momentum management for spacecraft," *2017 Chinese Automation Congress (CAC)*, 2017, pp. 6013–6016. https://doi.org/10.1109/CAC.2017.8243860.

[14] Liu, P., Zheng, Z., Chen, S., Sun, W., and Sun, Z., "Continuous momentum management for space station based on LESO," *Aerospace Science and Technology*, Vol. 72, 2018, pp. 364–370. https://doi.org/10.1016/j.ast.2017.11.022.

[15] Liu, P., Xue, W., Chen, S., Huang, Y., and Sun, Z., "An integrated solution to ACMM problem of spacecraft with inertia uncertainty," *International Journal of Robust and Nonlinear Control*, Vol. 28, No. 17, 2018, pp. 5575–5589. https://doi.org/10.1002/rnc.4332.

[16] Liu, P., Chen, S., Xue, W., and Li, W., "On Hierarchical Compensation Based Active Disturbance Rejection Control for ACMM Problem of Spacecraft," *Journal of Systems Science and Complexity*, Vol. 36, No. 4, 2023, pp. 1480–1497. https://doi.org/10.1007/s11424-023-1399-2.

[17] Choi, M., and Flashner, H., "Neural-network-based spacecraft attitude control and momentum management," *AIAA Guidance, Navigation, and Control Conference and Exhibit*, American Institute of Aeronautics and Astronautics, 2000. https://doi.org/10.2514/6.2000-4455.

[18] Elgersma, M., Stein, G., Jackson, M., and Yeichner, J., "Robust controllers for space station momentum management," *IEEE Control Systems Magazine*, Vol. 12, No. 5, 1992, pp. 14–22. https://doi.org/10.1109/37.158891.

[19] Wie, B., *Space Vehicle Dynamics and Control*, American Institute of Aeronautics and Astronautics, Inc., 2008, Chaps. 6,7.

[20] Montgomery, D., Peck, E., and Vining, G., *Introduction to Linear Regression Analysis*, John Wiley and Sons, Inc., 2012.

[21] Skogestad, S., and Postlethwaite, I., *Multivariable Feedback Control*, John Wiley and Sons, Ltd., 2005, Chap. 1.

Appendix

This appendix presents the linearized system of equations for an operating point of $\varphi^*_{B/N} = \begin{bmatrix} 0 & \theta^* & 0 \end{bmatrix}^T$, ${}_B\omega^*_{B/I} = {}_B\omega_{N/I}$, ${}_BH^*_c = 0$, where θ^* corresponds to an arbitrary pitch angle.

Linearized Dynamics

Solving Equation (3) with respect to the time derivative of the angular rate ${}_B\dot{\omega}_{B/I}$ gives the following relation:

$$ {}_B\dot{\omega}_{B/I} = -[{}_BJ]^{-1}[{}_B\omega_{B/I}\times] \cdot {}_BJ \cdot {}_B\omega_{B/I} + [{}_BJ]^{-1}{}_B\tau \tag{28} $$

Evaluating the expression and corresponding Jacobians at the operating point yields

$$ {}_B\dot{\omega}_{B/I} \mid_{x=x^*} = -[{}_BJ]^{-1}[{}_B\omega_{N/I}\times] \cdot {}_BJ \cdot {}_B\omega_{N/I} + [{}_BJ]^{-1}{}_B\tau|_{x=x^*} \tag{29} $$

$$ \begin{aligned} A_{\omega\varphi} &= \frac{\partial {}_B\dot{\omega}_{B/I}}{\partial \varphi} \mid_{x=x^*} = \frac{\partial {}_B\tau_g}{\partial \varphi} \mid_{x=x^*} + \frac{\partial {}_B\tau_a}{\partial \varphi} \mid_{x=x^*} \\ A_{\omega\omega} &= \frac{\partial {}_B\dot{\omega}_{B/I}}{\partial {}_B\omega_{B/I}} \mid_{x=x^*} = [{}_BJ]^{-1}[({}_BJ \cdot {}_B\omega_{N/I})\times] - [{}_BJ]^{-1}[{}_B\omega_{N/I}\times] \cdot {}_BJ \end{aligned} \tag{30} $$

In this way, the final linearized spacecraft dynamics can be expressed as follows:

$$ \Delta\dot{\omega} = A_{\omega\varphi}\Delta\varphi + A_{\omega\omega}\Delta\omega + [{}_BJ]^{-1}{}_B\tau_c + [{}_BJ]^{-1}{}_B\tau_{g,\text{rest}} + [{}_BJ]^{-1}{}_B\tau_{a,\text{rest}} - [{}_BJ]^{-1}[{}_B\omega_{N/I}\times] \cdot {}_BJ \cdot {}_B\omega_{N/I} \tag{31} $$

where $\Delta\varphi = \varphi_{B/N} - \varphi^*_{B/N}$ and $\Delta\omega = {}_B\omega_{B/I} - {}_B\omega_{N/I} = {}_B\omega_{B/N}$.

Linearized Gravity Gradient Torque

Assuming once again a 1-2-3 rotation, the following linear expression can be obtained for the gravity gradient torque by evaluating Equation (8) and its Jacobians at the operating point:

$$ \begin{aligned} {}_B\tau_g = \frac{\partial {}_B\tau_g}{\partial \varphi} \mid_{x=x^*} \Delta\varphi + {}_B\tau_{g,\text{rest}} &= 3\omega_0^2 \begin{bmatrix} (J_{3,3} - J_{2,2})\cos\theta_0 - J_{3,1}\sin\theta_0 \\ J_{1,2}\cos\theta_0 + J_{3,2}\sin\theta_0 \\ -J_{1,3}\cos\theta_0 + (J_{1,1} - J_{2,2})\sin\theta_0 \end{bmatrix} \Delta\phi \\ &+ 3\omega_0^2 \begin{bmatrix} \sin 2\theta_0 J_{2,3} + \cos 2\theta_0 J_{2,1} \\ -2\sin 2\theta_0 J_{3,1} + \cos 2\theta_0 (J_{3,3} - J_{1,1}) \\ -\cos 2\theta_0 J_{2,3} + \sin 2\theta_0 J_{2,1} \end{bmatrix} \Delta\theta + 3\omega_0^2 \begin{bmatrix} -\sin^2\theta_0 J_{3,1} + \sin\theta_0\cos\theta_0 (J_{3,3} - J_{2,2}) \\ \sin\theta_0\cos\theta_0 J_{1,2} + \sin\theta_0^2 J_{3,2} \\ -\sin\theta_0\cos\theta_0 J_{1,3} + \sin^2\theta_0 (J_{1,1} - J_{2,2}) \end{bmatrix} \Delta\psi \\ &+ \underbrace{3\omega_0^2 \begin{bmatrix} \sin\theta_0\cos\theta_0 J_{2,1} - \cos^2\theta_0 J_{2,3} \\ \sin\theta_0\cos\theta_0 (J_{3,3} - J_{1,1}) + \cos^2\theta_0 J_{1,3} \\ \sin^2\theta_0 J_{2,1} - \sin\theta_0\cos\theta_0 J_{2,3} \end{bmatrix}}_{{}_B\tau_{g,\text{rest}}} \end{aligned} \tag{32} $$

Linearized Aerodynamic Torque

In this derivation, it is assumed that the aerodynamic torque can be approximated by

$$ {}_B\tau_a = \frac{\partial {}_B\tau_a}{\partial \varphi_{B/N}} \mid_{x=x^*} \Delta\varphi + {}_B\tau_{a,\text{rest}} \tag{33} $$

where the terms $\frac{\partial {}_B\tau_a}{\partial \varphi_{B/N}} \mid_{x=x^*}$ and ${}_B\tau_{a,\text{rest}}$ must be identified following the procedure described in section IV.

Linearized Kinematics

For a 1-2-3 rotation, the nonlinear kinematics of the spacecraft (Equation (5)) can be expressed as:

$$\dot{\varphi}_{B/N} = \begin{bmatrix} \frac{\cos\psi}{\cos\theta} & -\frac{\sin\psi}{\cos\theta} & 0 \\ \sin\psi & \cos\psi & 0 \\ -\cos\psi\tan\theta & \sin\psi\tan\theta & 1 \end{bmatrix} {}_B\omega_{B/I} + \omega_0 \begin{bmatrix} \sin\phi\tan\theta \\ \cos\phi \\ -\frac{\sin\phi}{\cos\theta} \end{bmatrix} \tag{34}$$

Evaluating the Jacobians at the operating point yields

$$A_{\varphi\varphi} = \frac{\partial\dot{\varphi}_{B/N}}{\partial\varphi}\,|_{x=x^*} = \omega_0 \begin{bmatrix} \tan\theta^* & 0 & \frac{1}{\cos\theta^*} \\ 0 & 0 & 0 \\ -\frac{1}{\cos\theta^*} & 0 & -\tan\theta^* \end{bmatrix} \quad A_{\varphi\omega} = \frac{\partial\dot{\varphi}_{B/N}}{\partial_B\omega_{B/I}}\,|_{x=x^*} = \begin{bmatrix} \frac{1}{\cos\theta^*} & 0 & 0 \\ 0 & 1 & 0 \\ -\tan\theta^* & 0 & 1 \end{bmatrix} \tag{35}$$

Since $\dot{\varphi}_{B/N}\,|_{x=x^*} = 0$, the linearized kinematic equations become

$$\dot{\varphi}_{B/N} = A_{\varphi\varphi}\Delta\varphi + A_{\varphi\omega}\Delta\omega \tag{36}$$

Linearized CMG Dynamics

The linearization of the CMG dynamic equations is independent of the chosen attitude operating point and therefore follows the same derivation as before:

$${}_B\dot{H}_c = -[{}_B\omega_{N/I}\times]\cdot {}_BH_c - {}_B\tau_c \tag{17}$$

Linearized System

Finally. from the previous derivations, the full linear system for an arbitrary θ^* can be expressed as:

$$\begin{aligned} \begin{bmatrix} \Delta\dot{\varphi} \\ {}_B\dot{\omega}_{B/N} \\ {}_B\dot{H}_c \end{bmatrix} &= \begin{bmatrix} A_{\varphi\varphi} & A_{\varphi\omega} & 0 \\ A_{\omega\varphi} & A_{\omega\omega} & 0 \\ 0 & 0 & -[{}_B\omega_{N/I}\times] \end{bmatrix} \begin{bmatrix} \Delta\varphi \\ {}_B\omega_{B/N} \\ {}_BH_c \end{bmatrix} + \begin{bmatrix} 0 \\ [{}_BJ]^{-1} \\ -I \end{bmatrix} {}_B\tau_c \\ &+ \begin{bmatrix} 0 \\ [{}_BJ]^{-1} \\ 0 \end{bmatrix} \left({}_B\tau_{g,rest} + {}_B\tau_{a,rest}(t) + \omega_0^2 \begin{bmatrix} -{}_BJ_{2,3} \\ 0 \\ {}_BJ_{1,2} \end{bmatrix} \right) \end{aligned} \tag{37}$$

Part III

Additional Results

7

Aerodynamic Torque Model Identification and Validation

This chapter presents an additional set of results related to the identification of an aerodynamic torque model expressed in the LVLH reference frame for the nominal space station configuration. The analysis complements the main body of the thesis but was not used directly in the control design for several reasons. First, the model was identified in the LVLH frame rather than the Body frame in which the control problem was formulated. Second, only the linear attitude-dependent contribution can be incorporated into the linearized system used for $\mathcal{H}_\infty$ synthesis, whereas this model includes nonlinear dependencies on the solar array angles that fall outside that framework. In addition, the model requires real-time knowledge of the atmospheric density to reproduce the torque magnitude accurately, which may not be feasible on board. Despite these limitations, the results presented here offer useful insight into the aerodynamic torque characteristics and can serve as a foundation for higher-fidelity modeling.

7.1. Aerodynamic Torque Model Identification

In this section, model identification will be performed for the aerodynamic torque. In order to achieve this, it is useful to recall the torque's physical definition:

$$\tau_a(t, \varphi_{B/N}, \alpha_{SAW}) = r_{CoP}(\varphi_{B/N}, \alpha_{SAW}) \times \left[-\frac{1}{2}\rho(t) V V^T C_D A(\varphi_{B/N}, \alpha_{SAW}) n\right] \tag{7.1}$$

where r_{CoP} is the center of pressure offset from the center of gravity, ρ is the density of the atmosphere, V is the flight velocity of the spacecraft with respect to the atmosphere, C_D is the drag coefficient, A is the area projected onto the plane normal to the velocity vector, and n is the surface's normal vector.

In Equation (7.1), the dependencies on time, t, attitude, $\varphi_{B/N}$, and solar array angles, α_{SAW}, are made explicit. To simplify the model while preserving its physical relevance, the only time-dependent contribution considered is the atmospheric density, whereas the effects of other periodic variations are averaged out over several orbital periods. Taking this into consideration, it is proposed that the aerodynamic torque in the LVLH frame is expressed as:

$$ {}_N\tau_a \approx \frac{\rho(t)}{\rho_0}\left[{}_N\tau_{a,0} + {}_N\tau_{a,\varphi}(\varphi_{B/N}) + {}_N\tau_{a,\alpha_{SAW}}(\alpha_{SAW})\right] \tag{7.2}$$

where the first term, ${}_N\tau_{a,0}$, represents a constant offset, and the remaining terms, ${}_N\tau_{a,\varphi}$ and ${}_N\tau_{a,\alpha_{SAW}}$, capture the torque dependence on attitude and solar array angles, for a fixed atmospheric density, ρ_0.

The goal is to express ${}_N\tau_{a,\varphi}$ and ${}_N\tau_{a,\alpha_{SAW}}$ as linear functions of suitable transformations of attitude and solar array angles, respectively. To identify each of these terms, a set of simulations was performed in which the relevant variables were varied independently, allowing the separate characterization of the attitude- and solar-array-dependent components. The procedure used to generate the simulation data that serve as input to the estimator is further detailed in the following sections.

7.1.1. Recursive Least Squares

To perform the model identification, the Recursive Least Squares (RLS) method was used. The RLS is one of the most widely used recursive identification methods, and it can be seen as an adaptation of the ordinary least squares approach that allows for efficient updating of an existing model when new data becomes available. Assuming a linear model, the variable for which model identification is going to be performed, y can then be defined as:

$$y = A \cdot \vartheta + \epsilon \tag{7.3}$$

where A is the regression matrix, ϑ corresponds to the parameter vector to be estimated, and ϵ is the model residual vector. Additionally, the following notation simplifications as well as the regression matrix update, a_{k+1}, and the measurement vector update, y_{k+1}, can be introduced:

$$\begin{aligned} A_k &= A(t_k) \\ A_{k+1} &= \begin{bmatrix} A_k \\ a_{k+1} \end{bmatrix} \\ a_{k+1} &= a(t_{k+1}) \end{aligned} \tag{7.4}$$

$$\begin{aligned} Y_k &= \begin{bmatrix} y_1 & y_2 & \dots & y_k \end{bmatrix}^T \\ Y_{k+1} &= \begin{bmatrix} Y_k \\ y_{k+1} \end{bmatrix} \end{aligned} \tag{7.5}$$

The following equation shows the estimation algorithm to be implemented:

$$\begin{cases} K_{k+1} = P_k \cdot a_{k+1}^T \left[1 + a_{k+1} P_k a_{k+1}^T\right]^{-1} \\ P_{k+1} = \left[I - K_{k+1} a_{k+1}\right] P_k \\ \vartheta_{k+1} = \vartheta_k + K_{k+1} \left[y_{k+1} - a_{k+1} \vartheta_k\right] \end{cases} \tag{7.6}$$

where K is the RLS gain and P the parameter covariance matrix. Initial estimates of $\vartheta_0 = 0$ and $P_0 = I$ were considered.

7.1.2. Solar array-dependent contribution to aerodynamic torque

Firstly, the effects of varying the solar array angles of the spacecraft were assessed. To achieve this, the procedure depicted in Figure 7.1 was followed.

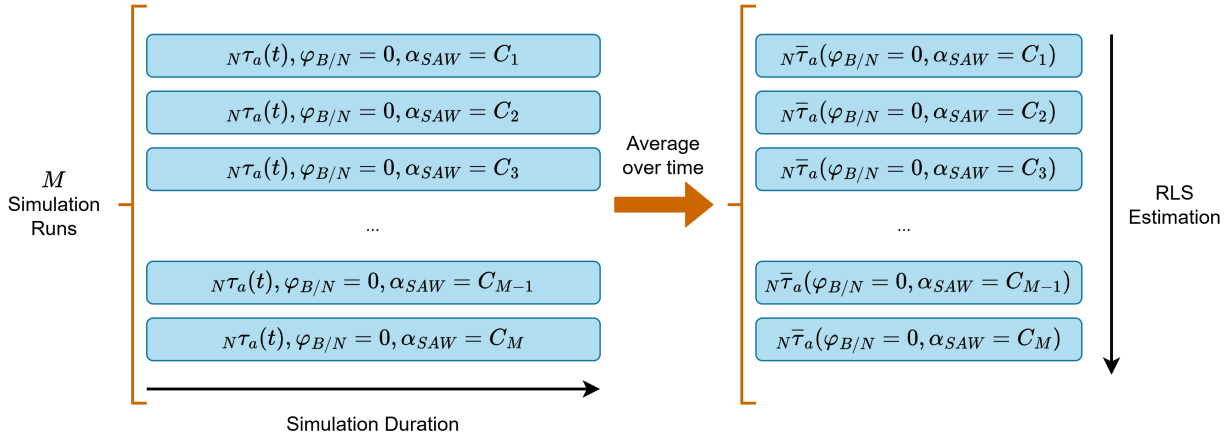

Figure 7.1: Procedure for identification of solar array-dependent component of the aerodynamic torque

For a set of M simulations, the atmospheric density was fixed at ρ_0 and the attitude was kept at $\varphi_{B/N} = 0$, such that the body frame is aligned with the LVLH frame. Within a given simulation, the solar array angles were held constant, but varied between simulations to cover the entire operational range from -180° to 180°. The resulting aerodynamic torque was averaged over 16 orbits for each configuration, ensuring that at least one full period of all dominant sinusoidal components was captured. This averaging yields the following simplified representation:

$$ {}_N\bar{\tau}_a = {}_N\tau_{a,0} + {}_N\tau_{a,\alpha_{SAW}}(\alpha_{SAW}) \tag{7.7} $$

As previously discussed, computing the mean torque averages out the sinusoidal time-dependent components. These effects are therefore embedded in the offset term. When combined with a fixed attitude and the atmospheric density, this approach allows the variation of the aerodynamic torque to be isolated to its solar array contribution.

In the generic RLS formulation of Subsection 7.1.1, the identification problem is written as $y = A \cdot \vartheta + \epsilon$ where each row of the regression matrix, A, is the regressor a_k and ϑ is the parameter vector to be estimated (Equation (7.3)). In this case, the quantity to be identified is the mean aerodynamic torque. For each torque component $i \in \{x, y, z\}$, the scalar output of the RLS problem can be defined as

$$ y_{k,i} = {}_N\bar{\tau}_{a,i}(t_k) \tag{7.8} $$

and the regression row, a_k, as

$$ a_k = \begin{bmatrix} 1 & \sin\big(2\alpha_{SAW,1}(t_k)\big) & \cos\big(2\alpha_{SAW,1}(t_k)\big) & \sin\big(2\alpha_{SAW,2}(t_k)\big) & \cos\big(2\alpha_{SAW,2}(t_k)\big) \end{bmatrix} \tag{7.9} $$

The corresponding parameter vector for axis i is $\vartheta_i \in \mathbb{R}^{5\times 1}$, so that for each axis

$$ y_{k,i} = a_k \cdot \vartheta_i + \epsilon_{k,i} \tag{7.10} $$

Stacking all M samples for a given axis i gives

$$ Y_i = A\,\vartheta_i + \epsilon_i \tag{7.11} $$

with A constructed by stacking the rows a_k. After running the RLS algorithm, the final estimates of ϑ_i are taken for each torque component and then arranged into the following matrix:

$$ M_\alpha = \begin{bmatrix} \vartheta_x^T \\ \vartheta_y^T \\ \vartheta_z^T \end{bmatrix} \in \mathbb{R}^{3\times 5} \tag{7.12} $$

Additionally, the regressor can be written in column form as

$$ \beta(\alpha_{SAW,1}, \alpha_{SAW,2}) = \begin{bmatrix} 1 \\ \sin\big(2\alpha_{SAW,1}\big) \\ \cos\big(2\alpha_{SAW,1}\big) \\ \sin\big(2\alpha_{SAW,2}\big) \\ \cos\big(2\alpha_{SAW,2}\big) \end{bmatrix} \tag{7.13} $$

Finally, the three scalar models can then be written compactly as

$$ {}_N\bar{\tau}_a = M_\alpha \cdot \beta \tag{7.14} $$

The selection of the regression vector, β, was guided by both physical reasoning and empirical analysis, as correlations between the aerodynamic torque and solar array angles revealed dominant second-harmonic dependencies consistent with the geometry of the panels. Therefore, the terms $\sin(2\alpha)$ and $\cos(2\alpha)$ were used as regression variables to capture these effects. The following results were obtained:

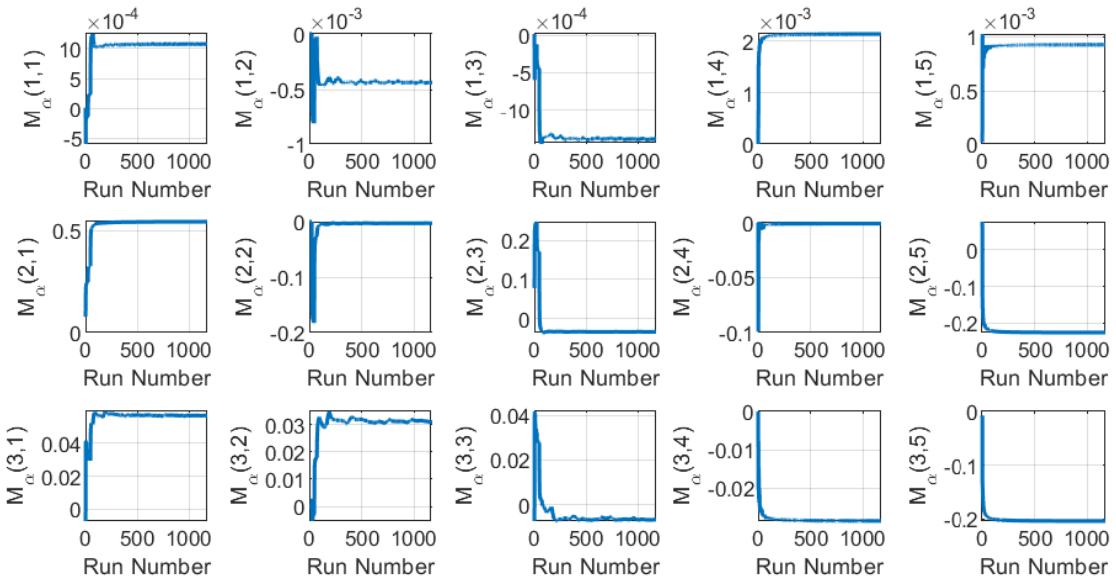

Figure 7.2: Normalized RLS-estimated coefficients of M_α

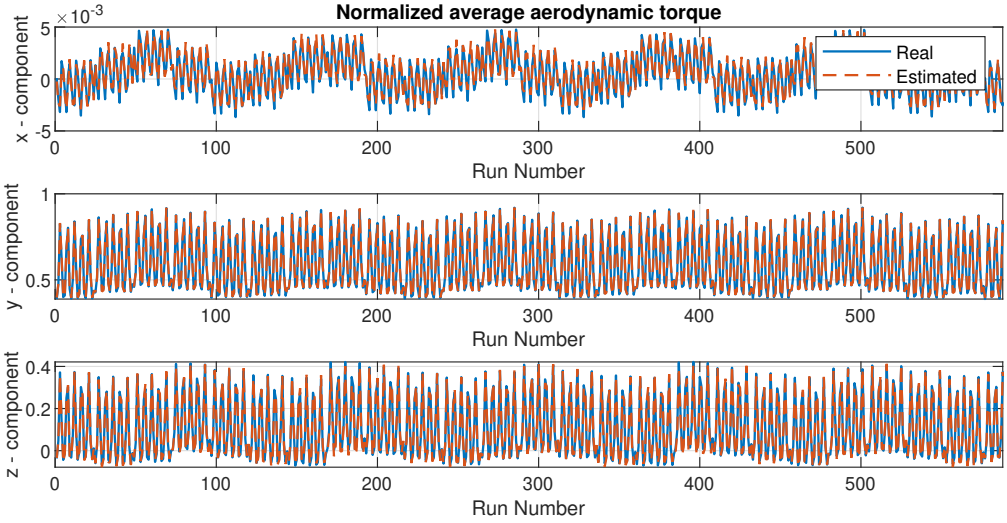

Figure 7.3: Normalized real and RLS-estimated average aerodynamic torque per simulation

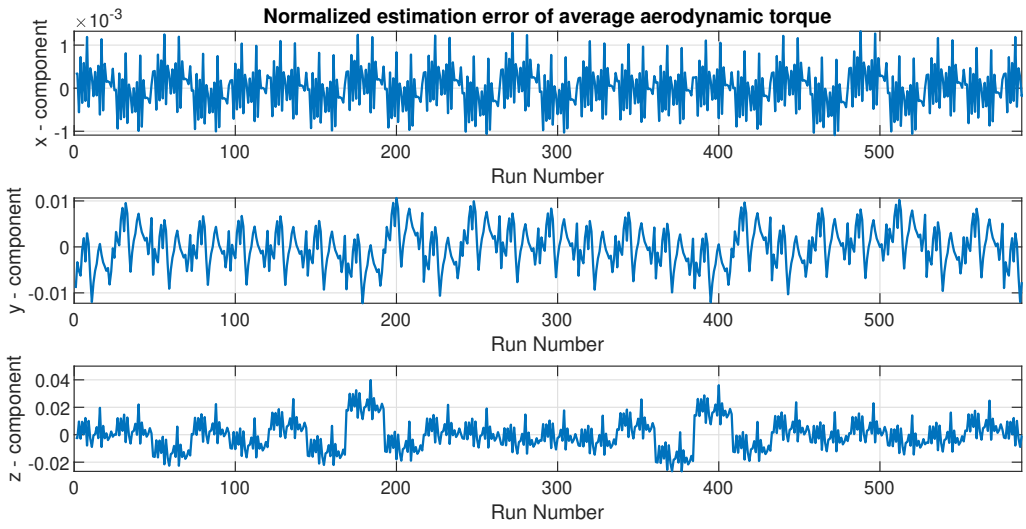

Figure 7.4: Normalized absolute RLS estimation error of average aerodynamic torque per simulation

All torque components shown in Figures 7.2 to 7.4 were normalized by the maximum Euclidean norm of the mean torque, so that each component was divided by this value for consistent visual comparison.

Figure 7.2 confirms the suitability of the selected regression vector for the given dataset, with the parameter estimates converging at approximately data point 500. Furthermore, Figures 7.3 and 7.4 illustrate the correspondence between the simulated aerodynamic torque and the torque reconstructed using the final estimated coefficients from Figure 7.2. For clarity, only a subset of the data points is shown, as the remaining samples exhibit the same behavior. The RLS estimation demonstrates reasonable accuracy, with maximum relative errors of approximately 20%, 10%, and 10% for the x-, y-, and z-components, respectively. Additionally, in absolute terms, these errors are on the order of 10^{-3}–10^{-2} of the torque magnitude, further validating the adequacy of the identified model.

7.1.3. Attitude-dependent contribution to aerodynamic torque

To quantify the effect of varying the attitude on the aerodynamic torque, a similar procedure was followed, as depicted in Figure 7.5.

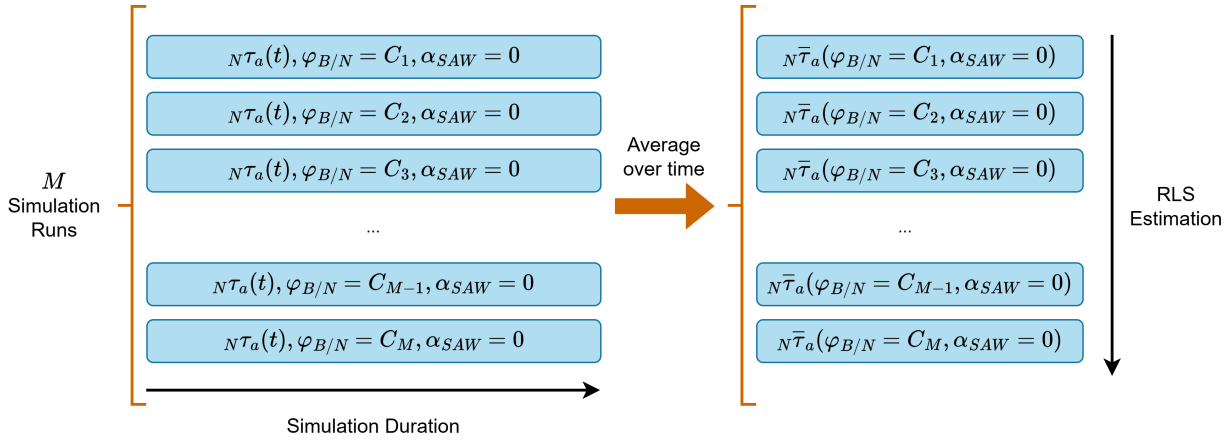

Figure 7.5: Procedure for identification of attitude-dependent component of the aerodynamic torque

For a set of M simulations, the atmospheric density was again fixed at ρ_0 and the solar array angles were kept at $\alpha_{SAW} = 0$. Within the same simulation, attitude was held constant, but varied between

simulations to cover the full operational range, corresponding to the expected small-angle deviations from the nominal orientation.

For the identification of this term, the RLS algorithm was again applied to the set of average torque values. The structure of the regression follows directly from the fact that each torque component depends linearly on the small attitude angles. This being the case, for each axis, the problem can be defined as

$$y_{k,i} = \begin{bmatrix} 1 & \phi(t_k) & \theta(t_k) & \psi(t_k) \end{bmatrix} \cdot \vartheta_i + \epsilon_{k,i}, \tag{7.15}$$

where $\vartheta_i \in \mathbb{R}^{4\times 1}$ contains the coefficients to be identified for torque component i.

After executing the RLS iterations for the three axes, the final parameter estimates are grouped into the coefficient matrix

$$M_\varphi = \begin{bmatrix} \vartheta_x^T \\ \vartheta_y^T \\ \vartheta_z^T \end{bmatrix} \in \mathbb{R}^{3\times 4}. \tag{7.16}$$

Writing the regressor in column form,

$$\beta(\varphi_{B/N}) = \begin{bmatrix} 1 \\ \phi \\ \theta \\ \psi \end{bmatrix}, \tag{7.17}$$

the attitude-dependent aerodynamic torque is compactly expressed as

$$_N\bar{\tau}_a = M_\varphi \cdot \beta \tag{7.18}$$

which corresponds to the regression structure used for the identification of the attitude-dependent torque model. Considering this, the following results were obtained:

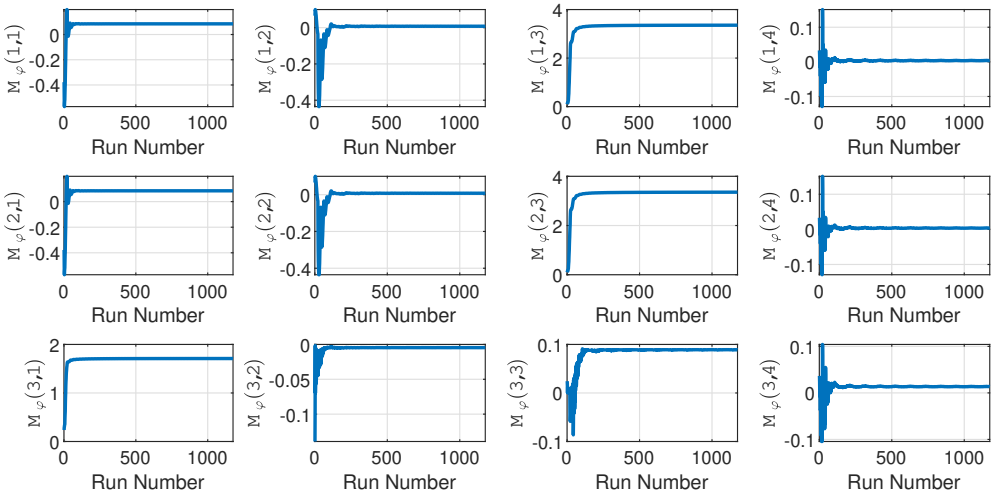

Figure 7.6: Normalized RLS-estimated coefficients of M_φ

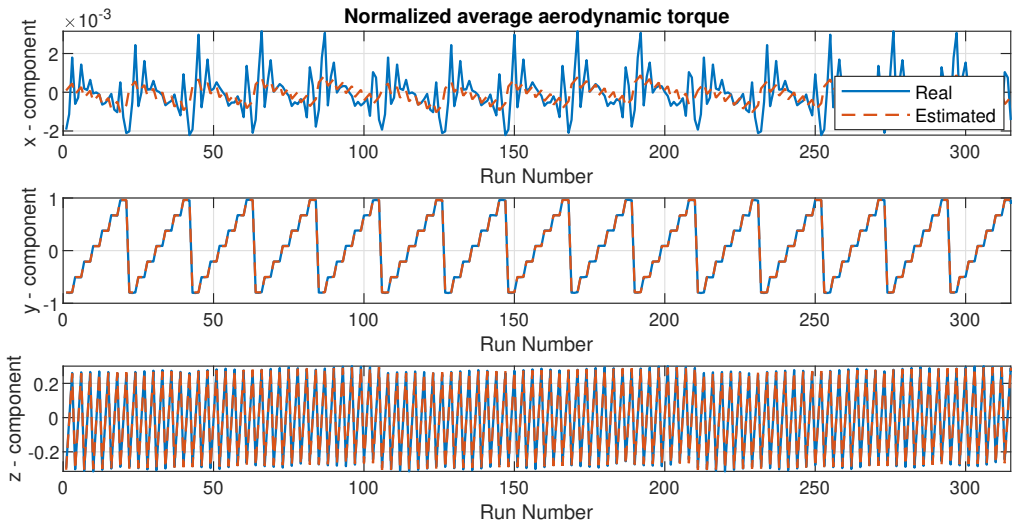

Figure 7.7: Normalized real and RLS-estimated average aerodynamic torque per simulation

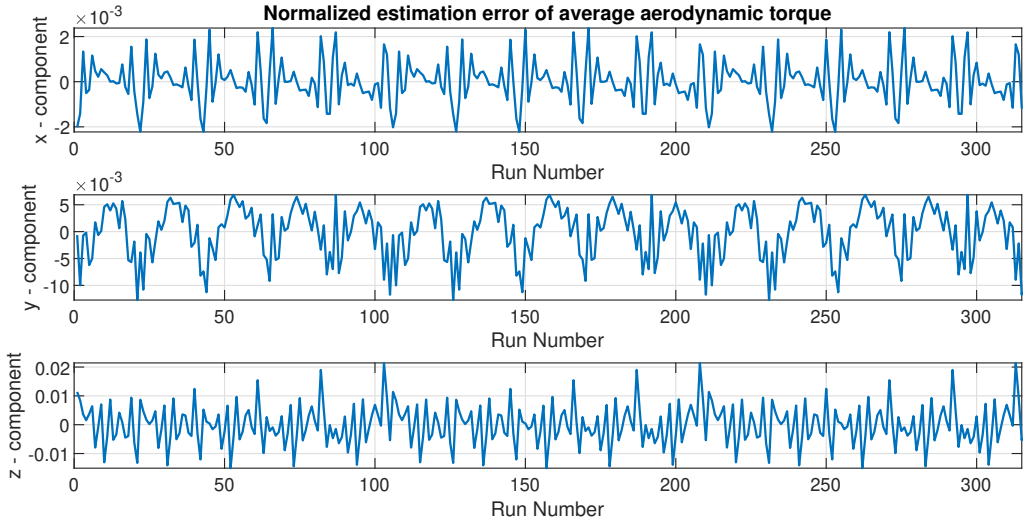

Figure 7.8: Normalized absolute RLS estimation error of average aerodynamic torque per simulation

Similarly to the results shown in the previous section, all torque components shown in Figures 7.6 to 7.8 were normalized by the maximum Euclidean norm of the mean torque.

Figure 7.6 illustrates the evolution of the estimated coefficients across simulations, showing general convergence after approximately 500 runs. The comparison between the estimated and simulated aerodynamic torques in Figures 7.7 and 7.8 indicates good agreement for the y- and z-components, with maximum relative errors of about 1% and 10%, respectively. In contrast, the estimation accuracy for the x-component is considerably lower, with errors reaching up to approximately 80%. Nevertheless, because these errors correspond to normalized absolute magnitudes on the order of 10^{-3} —- at least two orders of magnitude smaller than the total norm of the aerodynamic torque – it is considered that the identified model remains sufficiently accurate for practical purposes.

7.2. Model Validation in Time-Domain Simulation

One of the main simplifications in the identified aerodynamic torque model is that the attitude-dependent component was estimated assuming fixed solar array angles at $\alpha_{SAW} = 0$. In this way, potential coupling effects between attitude and solar array motion are not explicitly captured. To assess the influence of this simplification, a validation simulation was performed in which the spacecraft attitude remained close to zero (Figures 7.10 and 7.11), while the solar arrays oscillated throughout their full operational range, from -180° to 180°. This configuration allows the evaluation of the model's accuracy when the solar array angles vary dynamically.

The simulation was performed throughout five orbits using the high-fidelity Starlab simulator described in Part II. This simulator accounts for nonlinear spacecraft dynamics, inertia variations due to solar array motion, and detailed representations of aerodynamic, gravity-gradient, and solar radiation torques. Additionally, the real-time atmospheric density ratio, ρ/ρ_0, used in the simulation and shown in Figure 7.9, reflects the variations induced by the relative position of the space station to the Sun, and was used to scale the aerodynamic torque estimated from the identified model, following the formulation in Equation (7.2).

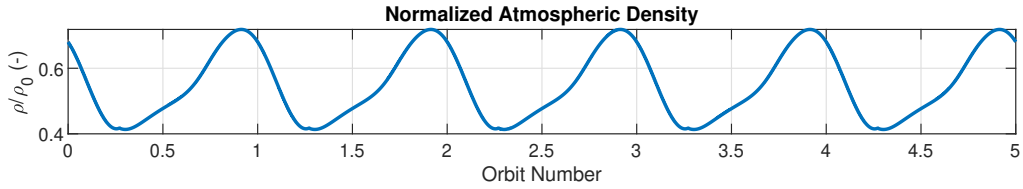

Figure 7.9: Atmospheric density ratio

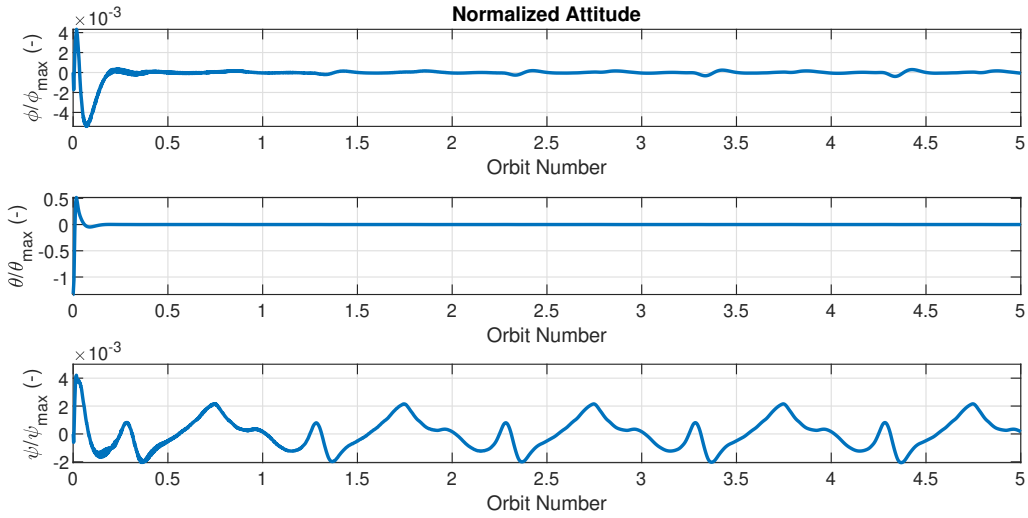

Figure 7.10: Normalized attitude

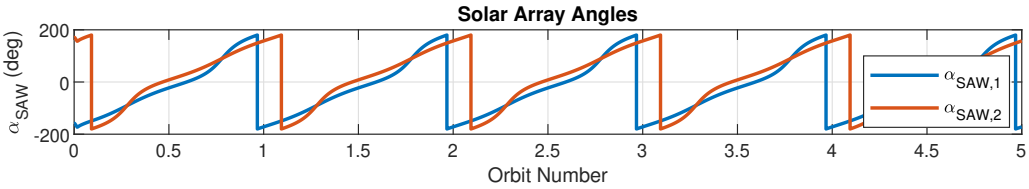

Figure 7.11: Solar array angles

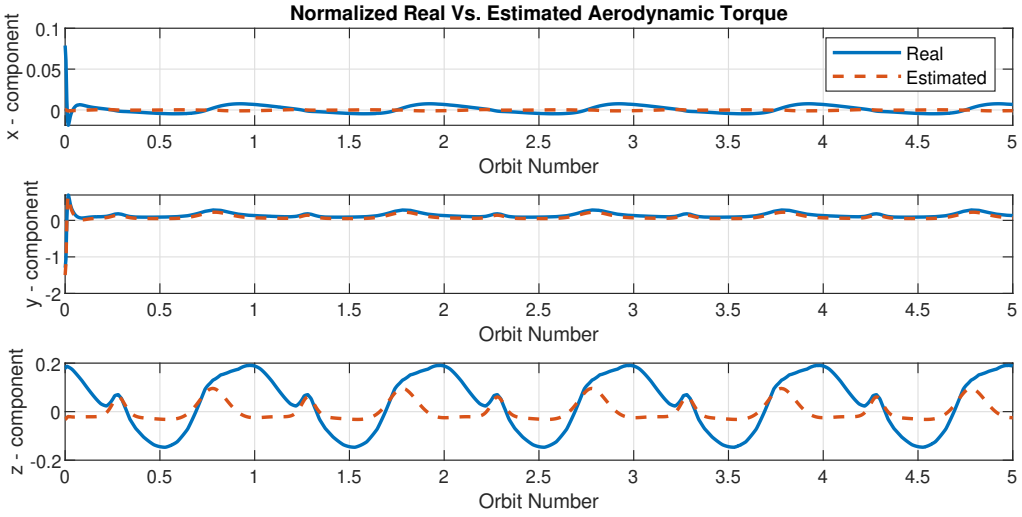

Figure 7.12: Normalized real and estimated aerodynamic torque

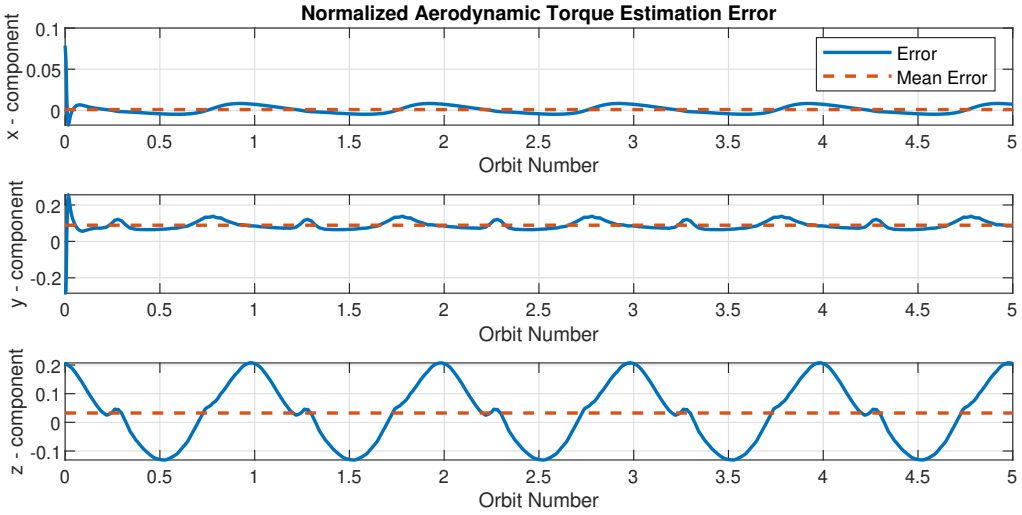

Figure 7.13: Normalized aerodynamic torque estimation error and its mean value

The comparison between the aerodynamic torque obtained from the high-fidelity simulator and the torque estimated using the identified model is presented in Figure 7.12. Overall, the simplified model reproduces the general magnitude of the aerodynamic torque across all components. However, especially for the x- and z-axes, it can be observed that the finer oscillatory behavior is not fully captured. This outcome is consistent with the modeling assumption that all time-dependent oscillations were averaged out, except for the atmospheric density variations. Consequently, the model is primarily intended to represent the mean aerodynamic torque and the dominant effects arising from attitude, solar array motion, and atmospheric density.

To assess whether this objective is achieved, the estimation error and its mean value were computed, as shown in Figure 7.13. The mean error remains at approximately 0.0009, 0.0888, and 0.0325 for the x-, y-, and z-components, respectively, in normalized units. These results indicate that, even though smaller fluctuations are not perfectly reproduced, the average aerodynamic torque is estimated with satisfactory accuracy.

7.3. Discussion

The aerodynamic torque modeling approach developed in this chapter aimed to obtain a more accurate characterization of the aerodynamic disturbance acting on Starlab, while remaining computationally manageable. The model captured the main dependencies of the torque on attitude, solar array angles, and atmospheric density, and its identification and validation results confirmed that it represents the aerodynamic behavior with reasonable accuracy.

However, several limitations can be identified. One of the main disadvantages of the proposed model is its reliance on real-time atmospheric density data. While this information could in principle be obtained from onboard sensors or estimated from environmental models, measurement is not always feasible, and estimation introduces additional errors in the overall torque estimation. Furthermore, the model intentionally neglects every time-dependent oscillation, except for the atmospheric density, by averaging it out. This limitation is particularly evident in the z-component, where some oscillations are not fully captured, even though the average estimation error remains relatively low.

Another contributing factor to the observed mismatch between the real and estimated aerodynamic torque is that the attitude-dependent term was identified assuming fixed solar array angles at $\alpha_{SAW} = 0$. This assumption does not reflect the operational conditions of the space station, in which the solar arrays continuously rotate to track the Sun. Consequently, the coupling between attitude and solar array motion is not explicitly represented in the identified model, leading to additional estimation errors.

Overall, the identified model was successful in quantifying how variations in attitude and solar array motion affect the aerodynamic torque acting on the spacecraft. Although it was ultimately not used for control synthesis, the work presented in this chapter clarified the trade-offs involved in simplifying the torque representation. The results highlight both the potential and the limitations of such an approach, serving as a useful reference for future refinements toward higher-fidelity aerodynamic modeling.

Part IV

Closure

8

Conclusions

This research addressed the problem of ACMM for Starlab, a modular LEO space station, currently under development to succeed the ISS. The need for continuous nadir-pointing, coupled with strict operational limitations, such as on thruster usage and momentum storage, as well as significant environmental disturbances makes the ACMM problem particularly challenging. The large disturbance torques to which large LEO platforms are subjected to – namely gravity gradient and aerodynamic torques – induce long-term momentum accumulation in the Momentum Exchange Devices (MEDs) used for attitude control. This accumulation leads to actuator saturation and therefore loss of control authority if not managed. For this reason, it is essential to develop a control system that is able to limit angular momentum errors, by minimizing the total contribution of the environmental disturbances with an acceptable attitude offset.

The work presented in this report focused on developing a robust control architecture that achieves an adequate attitude/momentum error trade-off, by explicitly accounting for environmental disturbances. Due to its complexity, particular attention was given to the aerodynamic torque contribution. Whereas most existing studies rely on simplified aerodynamic torque expressions, often completely neglecting its dependency on attitude, this research proposed an improved linear model derived from available data on the spacecraft's and orbit geometry. Results showed that this torque can be well approximated as a linear function of attitude for small deviations from the nominal nadir-pointing orientation. Considering this, a mean aerodynamic torque model was identified using the least-squares approach, enabling the representation of the torque as a linear function of attitude for a given Right Ascension of the Ascending Node (RAAN). This formulation bridges the gap between complex nonlinear aerodynamic models and the linear control design framework, providing a more realistic description of the aerodynamic effects acting on the spacecraft.

Building on this model, a robust $\mathcal{H}_\infty$ controller was synthesized to achieve disturbance rejection under modeling uncertainties and flexible-body dynamics. The controller formulation was based on the linearized equations of motion of the spacecraft and dynamics of the CMGs, where attitude, angular momentum and the control torque were treated as performance outputs and the environmental torques as exogenous disturbances. Through appropriate scaling and the definition of frequency-domain weighting filters, the design was able to ensure that the magnitude of the closed-loop transfer functions from disturbance torque to performance outputs remained within acceptable bounds. Additionally, unmodeled structural flexible modes were considered in the design by penalizing control effort for high frequencies. In the weighting filter tuning process, it became evident that the performance constraints were intrinsically linked to the properties of the space station itself. The conducted analysis revealed that the nominal Starlab configuration exhibits limited gravity-gradient control authority, which restricts its capability to counteract the aerodynamic torque acting on the spacecraft. For a modified plant with increased inertia asymmetry, the controller was able to achieve lower steady-state attitude and momentum errors, confirming the importance of mass distribution in enhancing the natural stability of the system.

Considering a less symmetric configuration with a docked vehicle, where satisfactory gravity-gradient torque authority is achieved, time-domain simulations using both the linearized plant and a high-fidelity nonlinear simulator confirmed the effectiveness of the proposed control approach. In both cases, the controller maintained stable behavior and achieved bounded performance outputs under high-fidelity disturbance profiles. The overall closed-loop behavior demonstrated that the designed controller was able

to achieve a suitable and robust trade-off between attitude accuracy and momentum management. Moreover, the same controller was tested for different RAANs than the one for which it was designed. Results showed that for every considered RAAN spanning from $0^\circ - 360^\circ$ the response was still stable and attitude, angular momentum and the control torque remained within acceptable bounds, without any high frequency flexible mode excitation. This not only showcases the robustness of the control system to modeling uncertainties but also validates the proposed mean aerodynamic torque model.

All in all, this thesis contributed to the understanding and control of coupled attitude and angular momentum dynamics for large LEO orbit platforms. By incorporating a data-informed aerodynamic torque model into the control design and validating a robust $\mathcal{H}_\infty$ synthesis approach, the work provided a framework that bridges the gap between theoretical robustness analysis and realistic space station operation.

8.1. Revisiting the Research Questions

In this section, the previously formulated research questions are revisited and answered based on the obtained results and conducted analysis. The research questions posed in Chapter 4 are repeated below for convenience.

1. **How can the mission requirements for Starlab (continuous nadir pointing, minimal thruster usage, and long-term operational efficiency) together with the physical constraints of the ACMM problem (actuator momentum capacity, mass distribution, flexible modes, and environment-induced disturbances) be translated into concrete control-design requirements?**

    - **What are the primary control objectives (performance goals) and how are they prioritized?**
      The starting point in defining the control problem lies in translating mission objectives into measurable control goals. For Starlab, one of the main mission requirements is to maintain a nadir-pointing orientation throughout the nominal operational mode to guarantee continuous communication and proper payload alignment. This defines the attitude control objective, which imposes a constraining bound on pointing errors.
      The second mission constraint concerns the minimization of thruster usage to prevent the disturbance of the microgravity environment, as well as the containment of operational costs and insurance of mission longevity. Consequently, momentum management must rely on attitude control, which in turn makes use of CMGs. This leads to the requirement that CMG angular momentum remains bounded, thereby preventing actuator saturation and limiting the frequency of desaturation maneuvers.
      Finally, long-term operational efficiency implies that the control effort should remain within acceptable bounds, ensuring that the commanded torque does not go over the operational limits of the actuators and that flexible structural modes are not excited. These three goals – attitude accuracy, and momentum and control effort management – establish the core of the ACMM performance requirements.
    - **Which measurable performance metrics represent those objectives?**
      To translate these qualitative goals into control design specifications, quantitative metrics are defined. The attitude pointing requirement is expressed as a maximum steady-state attitude error, that not only fulfills the mission requirements but also ensures that the simplified system used for control design remains valid. The momentum management objective is defined by bounding the total CMG stored momentum below its saturation limit.
      Additionally, the control effort is constrained by the CMG torque capabilities and by frequency-domain limits to prevent excitation of structural modes. The spacecraft's flexible structures impose an upper bound on the control effort in the frequency domain. More specifically, it is desirable that the controller exhibits low gain beyond approximately 0.3 rad/s, where flexible modes are expected.
      The controller must also ensure adequate robustness margins to cope with model uncertainties, such as inertia variations and disturbance modeling inaccuracies. Minimum robustness metrics were established, including a gain and phase margins of at least 3 dB and 30°, respectively, and a disk margin of 0.5.

- **How can the spacecraft's physical constraints be represented in the $\mathcal{H}_\infty$ control design?**
  In addition to the mission requirements, the physical characteristics of the spacecraft establish additional constraints on the ACMM problem. The most significant constraints are the CMG torque and momentum limits, the mass and inertia distribution, and the presence of structural flexibility. The inertia properties of the station not only define the dynamic coupling between axes but also determine the gravity-gradient torque authority. As shown in the analysis, the nominal configuration of Starlab provides limited control authority for the roll/yaw dynamics due to the significant symmetry between the pitch and yaw principal moments of inertia. This directly restricts the attainable performance, by increasing the maximum magnitude of attitude/momentum errors.
  Similarly, the flexible structural dynamics constrain the control bandwidth and shape the required frequency response of the controller. These physically imposed constraints are incorporated into the control problem through the design of weighting filters that penalize control action in frequency ranges associated with structural modes. Through the weighting filter tuning process, it became evident that the achievable performance is intrinsically linked to the physical properties of the space station itself.
- **How should environmental disturbances be characterized for robust control design?**
  A crucial step in accurately defining the control problem is to represent the external disturbances in a way that can be addressed by robust synthesis methods. The environmental torques acting on the spacecraft — primarily gravity-gradient and aerodynamic torques — are modeled as additive disturbance inputs in the plant (Figure 8.1). While the gravity-gradient torque can be accurately represented analytically, the aerodynamic torque exhibits a complex dependence on the spacecraft's attitude, geometry, and orbital parameters.

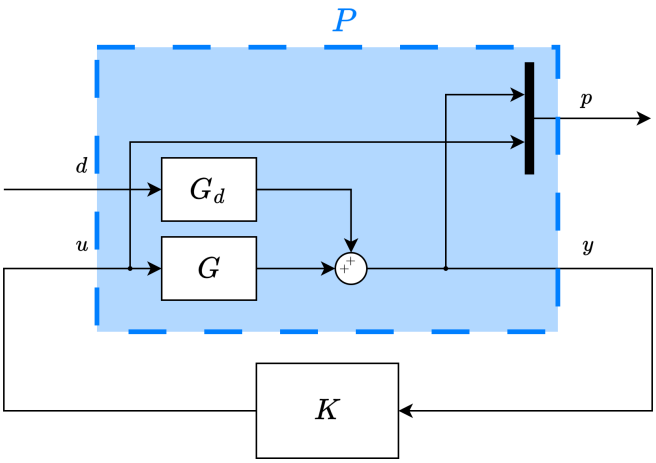

Figure 8.1: Generalized plant P with the positive feedback controller K

To address this, a linear mean aerodynamic torque model was identified through a least-squares fit to high-fidelity aerodynamic data. This model captures the mean dependence of the torque on the spacecraft attitude for a given RAAN. In this way, it is possible to include this torque's attitude-dependent contribution in the linear control framework. The residual time-varying component of the aerodynamic torque is treated as an external disturbance with dominant frequency content at the orbital rate and its harmonics. This characterization allows the definition of disturbance weighting filters that enforce rejection in these specific frequency ranges.

- **Which control architecture best incorporates these requirements and constraints?**
  This question was mainly addressed in Chapters 3 and 4, where a detailed assessment of the advantages and limitations of various state-of-the-art approaches to ACMM was conducted. After establishing the mission objectives, constraints, and disturbance models, it became clear

that a control architecture capable of achieving robustness and performance simultaneously was required. The $\mathcal{H}_\infty$ synthesis framework provides an intuitive way to integrate the ACMM requirements, since these are mainly described in the frequency domain. In this framework, the attitude deviation, CMG angular momentum, and control torque are defined as the performance outputs to be minimized, while the external torques are treated as exogenous disturbances. The design process is achieved by weighting filters that shape the closed-loop behavior: low-frequency filters enforce disturbance rejection and limit steady-state attitude and momentum errors, whereas high-frequency filters restrict control effort to prevent flexible-mode excitation. The resulting control law achieves a trade-off between accuracy, efficiency, and robustness, reflecting the inherent trade-offs of the ACMM problem. The analysis showed that increasing gravity-gradient authority — either by modifying the mass distribution or by considering a configuration with a docked vehicle — improves control performance, emphasizing the coupling between spacecraft design and control feasibility.

2. **How do modeling assumptions affect the fidelity and validity of the spacecraft model used for $\mathcal{H}_\infty$ control design?**

   - **What are the main simplifying assumptions adopted to formulate a model of the spacecraft for $\mathcal{H}_\infty$ control design?**
     To make the spacecraft dynamics suitable for robust control synthesis, several simplifications were introduced. Firstly, the model assumes rigid-body motion, constant mass and inertia properties, circular orbital motion, and small attitude deviations between the Body and LVLH frames. These assumptions allow for simplified environmental torque representation, and overall equations of motion such that a linear, time-invariant representation of the ACMM problem, suitable for $\mathcal{H}_\infty$ synthesis, is obtained. They enable analytical derivation of the system equations while still retaining the key physical mechanisms governing attitude and momentum dynamics. Known and unmodeled effects such as the flexible modes are accounted for by closed-loop transfer function shaping.
   - **How do these assumptions influence the accuracy and applicability of the model in nominal conditions?**
     Each simplification introduces a trade-off between modeling accuracy and analytical simplicity. The rigid-body assumption neglects structural flexibility, ignoring possible interactions between the attitude dynamics and low-frequency flexible modes of the solar arrays. This exclusion limits the achievable control bandwidth and requires conservative shaping of the controller to prevent excitation of unmodeled flexible modes. The assumption of constant inertia properties overlook the mass distribution variation due to solar array Sun tracking, further contributing to model mismatch. Although these effects are small in steady operations, they represent parametric uncertainties that can shift the system's natural dynamics. Similarly, the circular orbit assumption neglects small variations in gravity-gradient torque due to eccentricity and orbital perturbations. All in all, it was shown that these approximations provide a sufficiently accurate model within nominal orbital and structural conditions, provided that robustness margins are guaranteed.

   - **Within which operational boundaries does the linearized model remain valid for robust control design?**
     The small-angle and circular-orbit assumptions define the local validity region of the linearized model. The attitude kinematics are linearized by assuming small deviations from the nominal nadir-pointing orientation, which is accurate as long as angular deviations are limited up to $30°$. The linear model is therefore valid for near-equilibrium operations, but not for large reorientations or slew maneuvers. Similarly, the circular-orbit assumption constrains the model to low-eccentricity orbits, where orbital angular velocity and gravity-gradient force can be considered constant. Within these boundaries, the linear model captures the dominant system behavior, allowing the $\mathcal{H}_\infty$ controller to ensure robust performance. Outside this range, a higher-fidelity or gain-scheduled model would be required to maintain accuracy and stability.

3. **How can the robustness and performance of the synthesized control system be validated across different configurations, orbital conditions, and environmental variations?**

- **How can the controller's performance be evaluated under nominal conditions?**
  The $\mathcal{H}_\infty$ controller was validated in the configuration of Starlab with a docked vehicle using the linear model, where the inertia properties, aerodynamic environment, and orbit parameters correspond to the design model. Time-domain simulations confirmed that the controller maintained stable nadir-pointing with small steady-state errors and smooth transient responses. The control torque remained within actuator limits, and the CMG angular momentum oscillated around zero, demonstrating effective momentum management. The performance metrics observed in simulation matched the design specifications derived from the weighting filters, confirming that the controller achieved the expected disturbance rejection.
- **How can the controller's performance be validated across different orbital conditions?**
  The orbital dependence of the aerodynamic torque was analyzed by evaluating the controller performance for multiple values of the RAAN. Although the linear mean aerodynamic model was derived for a specific orbital condition, simulations confirmed that the controller maintained satisfactory performance for the full RAAN range considered. The attitude tracking accuracy and CMG momentum levels showed limited sensitivity to RAAN variation, validating the robustness of the control design against environmental changes. This outcome suggests that the linear model captures the essential aerodynamic behavior across realistic orbital conditions and that the controller's stability margins compensate for residual modeling errors.
- **How can the overall robustness envelope be established and verified?**
  Results demonstrated that the linear controller remains effective across variations in inertia, orbital parameters, and aerodynamic conditions, for an operational region near the operating point around which the system was linearized. Performance remained acceptable for every RAAN for which the controller was tested. These findings validate the design approach and confirm that the modeling assumptions and weighting filter structure is adequate and robust.

8.2. Concluding Remarks

To conclude, a discussion on the extent to which the research objectives have been met is performed. Once again, for convenience the research objectives from Chapter 4 are restated below.

Research Objective 1

To characterize the dominant environmental disturbances – gravity gradient and aerodynamic torque – such that they can be integrated into the $\mathcal{H}_\infty$ controller synthesis framework.

Research Objective 2

To design and implement an $\mathcal{H}_\infty$-based control strategy, focusing on disturbance rejection, for spacecraft Attitude Control and Momentum Management (ACMM) in the context of the Starlab space station's nominal mode.

Research Objective 3

To evaluate the robustness, performance, and limitations of the $\mathcal{H}_\infty$ controller using a high-fidelity Starlab simulator.

The three research objectives defined at the beginning of this work were addressed within the limits of the adopted modeling assumptions. The first objective, to characterize the dominant environmental disturbances for inclusion in the $\mathcal{H}_\infty$ control framework, was met by developing simplified but representative models of the gravity-gradient and aerodynamic torques. These models captured the main disturbance behavior relevant to the station's nominal operational conditions and were suitable for integration into the linear control formulation.

The second objective, to design and implement an $\mathcal{H}_\infty$-based control strategy for Starlab's nominal

mode, was achieved through the synthesis of a controller that balances attitude accuracy, disturbance rejection, and momentum management. The resulting control law performed as expected in the nominal configuration, maintaining pointing stability and bounded CMG momentum levels.

The third objective, to evaluate robustness and performance using a high-fidelity simulator, was met by testing the controller under variations in inertia, orbital parameters, and aerodynamic conditions. The results showed that performance remained acceptable across all tested cases. Overall, the research objectives were met to the extent required to validate the proposed control approach for Starlab's nominal operational mode with a docked vehicle, and to highlight the ACMM constraints for the nominal configuration of the space station.

8.3. Future Outlook

The findings presented in this thesis extend beyond the immediate application to Starlab by offering insights on the design and operation of any future large-scale spacecraft operating in LEO. With the expected and continued evolution of space stations, the coupled nature of attitude control and momentum management will remain a fundamental challenge that constrains both spacecraft design and operational strategy.

This work demonstrates that the achievable performance in ACMM is not only determined by the developed control algorithm, but also constrained by the physical properties of the spacecraft itself. The observation that gravity-gradient control authority directly influences the achievable trade-off between attitude deviation minimization and momentum accumulation suggests that mass distribution should be considered as a primary design variable in early mission phases, rather than a constraint to be managed through control. Future space station architectures could benefit from asymmetry in their mass distribution, to compensate for the significant aerodynamic disturbances. This represents a shift from viewing ACMM as a problem to be solved purely through control design, towards an approach where structural and control design are simultaneously contemplated from the outset.

The improved aerodynamic torque characterization developed in this research highlights the value of high-fidelity environmental modeling for control design. Additionally, the methodology presented here bridges the gap between complex nonlinear disturbance models and linear control frameworks through data-driven identification. This approach is particularly relevant in balancing sufficient model accuracy and computational constraints in on-board software.

Looking further ahead, the modular nature of space stations introduces time-varying inertial properties that extend beyond what can be addressed through fixed-gain robust control. The $\mathcal{H}_\infty$ framework used in this work provides a foundation upon which parameter-varying or gain-scheduled extensions could be built, enabling a single control architecture to adapt across different operational configurations.

Lastly, this research underscores the following principle: effective control system design for large space structures requires not only robust algorithms but also accurate models of the environment in which they operate. The success of Starlab and other future space stations will depend on the refinement of both aspects – developing control methods that provide formal guarantees of performance and robustness, while improving the estimation of the environmental disturbances. The framework established in this thesis demonstrated that when environmental disturbances are properly characterized and incorporated into the design process, robust control synthesis can achieve reliable performance even under model uncertainties.

9

Recommendations

The conducted research demonstrated the applicability of $\mathcal{H}_\infty$ control synthesis to the ACMM problem of Starlab. While the proposed controller achieved the expected performance within the nominal operational mode, several aspects of the modeling and control design can be further developed.

9.1. Controller Order Reduction

A practical limitation of the present design lies in the high order of the controller resulting from the $\mathcal{H}_\infty$ synthesis process. The inclusion of several weighting filters in the generalized plant leads to a controller with a large number of internal states, potentially increasing computational load which is undesirable for on-board implementation. Future work should therefore focus on controller order reduction techniques that preserve the main closed-loop characteristics while simplifying the structure. A reduced-order controller would facilitate real-time implementation and make the proposed approach more suitable for flight software integration.

9.2. Aerodynamic Torque Refinement & Parameter-Varying Model

A possible extension of the current work is to improve the representation of the aerodynamic torque by introducing parameter dependencies that reflect measurable variations in the spacecraft configuration and orbital environment. In the present study, the mean aerodynamic torque contribution was identified for a given orbital condition. However, a higher fidelity model of the aerodynamic torque could be achieved by identifying a linear model dependent on known solar array angle measurements. This improves the model proposed in this work in the sense that instead of performing a mean estimation, the model would integrate a more detailed aerodynamic torque model including the variation induced by solar array rotation, which is in itself intrinsically related to the orbital geometry.

Building on this aerodynamic model, the problem could be formulated as a Linear Parameter-Varying (LPV) system. In such an approach, parameters such as solar array angles or orbital elements could serve as scheduling variables. This would make it possible to preserve the robustness and disturbance rejection properties of the $\mathcal{H}_\infty$ design. Overall, a parameter-varying formulation would increase the consistency between the control model and the real system behavior, potentially leading to improved performance.

9.3. Numerical Implementation and Real-Time Considerations

Although the high-fidelity simulator used in this work allowed for detailed validation of the control performance, further investigations are required to assess the numerical aspects associated with real-time implementation. This includes evaluating the computational load of the synthesized controller, the effects of discretization, and sensitivity to sampling frequency. This analyses would provide some insights into computational requirements and numerical stability margins, helping to define appropriate discretization for on-board applications.

References

[1] NASA. *50 Years Ago: Launch of Salyut, the World's First Space Station*. https://www.nasa.gov/missions/station/50-years-ago-launch-of-salyut-the-worlds-first-space-station/. Accessed: 2025-10-20. 2021.

[2] NASA. *Skylab: America's First Space Station*. https://www.nasa.gov/history/50-years-ago-the-launch-of-skylab-americas-first-space-station/. Accessed: 2025-10-20. 2023.

[3] Portree, D. *Mir Hardware Heritage*. NASA SP-4225. NASA Johnson Space Center, 1995. Chap. 1.

[4] NASA. *International Space Station*. https://www.nasa.gov/reference/international-space-station/. Accessed: 2025-10-20. 2025.

[5] Starlab. *Our Mission*. URL: https://starlab-space.com/ (visited on 03/25/2025).

[6] Thompson, R. "Torque equilibrium attitudes for the Space Station". In: Nov. 1993. URL: https://ntrs.nasa.gov/citations/19940019976.

[7] Raigoza, K., and Sands, T. "Autonomous Trajectory Generation Comparison for De-Orbiting with Multiple Collision Avoidance". In: *Sensors* 22.18 (Jan. 2022), p. 7066. DOI: 10.3390/s22187066. URL: https://www.mdpi.com/1424-8220/22/18/7066 (visited on 03/26/2025).

[8] Voyager Space / Airbus. *Starlab – Next Generation Space Station*. https://www.airbus.com/en/products-services/space/space-exploration/starlab. Accessed: 2025-10-20. 2024.

[9] Foust, J. *Airbus and Voyager finalize Starlab joint venture*. URL: https://spacenews.com/airbus-and-voyager-finalize-starlab-joint-venture/ (visited on 03/25/2025).

[10] Wie, B. *Space Vehicle Dynamics and Control*. American Institute of Aeronautics and Astronautics, Inc., 2008.

[11] Woo, H., Morgan, H., and Falangas, E. "Momentum management and attitude control design for a Space Station". en. In: *Journal of Guidance, Control, and Dynamics* (May 1988). DOI: 10.2514/3.20264. URL: https://arc.aiaa.org/doi/10.2514/3.20264.

[12] Harduvel, J. "Continuous momentum management of earth-oriented spacecraft". In: *Journal of Guidance, Control, and Dynamics* 15.6 (1992), pp. 1417–1426. DOI: 10.2514/3.11405. URL: https://doi.org/10.2514/3.11405.

[13] Dang, Q., and Jin, L. "Multistage Angular Momentum Management for Space Station Attitude Control". In: *IEEE Access* 6 (2018), pp. 15075–15086. DOI: 10.1109/ACCESS.2018.2811759. URL: https://ieeexplore.ieee.org/abstract/document/8306382.

[14] Elgersma, M., Stein, G., Jackson, M., and Yeichner, J. "Robust controllers for space station momentum management". In: *IEEE Control Systems Magazine* 12.5 (Oct. 1992), pp. 14–22. DOI: 10.1109/37.158891. URL: https://ieeexplore.ieee.org/abstract/document/158891.

[15] Byun, K., Subramaniam, M., Hua, T., and Sunkel, J. "Robust attitude control design for a spacecraft with articulating appendages". In: *Guidance, Navigation, and Control Conference*. American Institute of Aeronautics and Astronautics, 1997. DOI: 10.2514/6.1997-3756. URL: https://arc.aiaa.org/doi/abs/10.2514/6.1997-3756.

[16] Wang, X., Yao, Y., Guo, J., Liu, K., and Guo, Y. "Attitude control and momentum management of space station via weighted-state H∞ method". In: *Proceedings of the 33rd Chinese Control Conference*. July 2014, pp. 1001–1006. DOI: 10.1109/ChiCC.2014.6896764. URL: https://ieeexplore.ieee.org/abstract/document/6896764?casa_token=9kMM4DnIYMQAAAAA:OLItovmGjZwyujs5eMHPDlzI6PX0YDpbQDGnom-yrl3JOaGG5RFaOaTIaR_yd6Wo-wbNueAt.

[17] Han, B., and Huo, W. “Robust Approach to Attitude Control and Momentum Management for Space Station”. In: *Applied Mechanics and Materials* 644-650 (2014), pp. 578–585. DOI: 10.4028/www.scientific.net/AMM.644-650.578. URL: https://www.scientific.net/AMM.644-650.578.

[18] Paynter, S., and Bishop, R. “Adaptive Nonlinear Attitude Control and Momentum Management of Spacecraft”. In: *Journal of Guidance, Control, and Dynamics* 20.5 (1997), pp. 1025–1032. DOI: 10.2514/2.4150. URL: https://doi.org/10.2514/2.4150.

[19] Zhu, M., and Xu, S. “Stability-based SDRE controller for spacecraft momentum management”. In: *Acta Astronautica* 89 (Aug. 2013), pp. 71–82. DOI: 10.1016/j.actaastro.2013.03.026. URL: https://www.sciencedirect.com/science/article/pii/S0094576513001094.

[20] Sainudeen, S., Soumya, N., and Sreeja, S. “Integrated Adaptive Control of Attitude and Momentum for Space Station”. In: *IFAC-PapersOnLine*. 6th Conference on Advances in Control and Optimization of Dynamical Systems ACODS 2020 53.1 (Jan. 2020), pp. 561–566. DOI: 10.1016/j.ifacol.2020.06.094. URL: https://www.sciencedirect.com/science/article/pii/S2405896320301130.

[21] Liu, P. “Partial state based attitude control and momentum management for spacecraft”. In: *2017 Chinese Automation Congress (CAC)*. Oct. 2017, pp. 6013–6016. DOI: 10.1109/CAC.2017.8243860. URL: https://ieeexplore.ieee.org/abstract/document/8243860?casa_token=XRRKg73AwywAAAAA:ei_i2FFqX2yTfSTjqsL25JhZ_2fGsNgLM3N128ZajsvT3dsaTwCcYWZKjyAohv7DHtvAABH2.

[22] Liu, P., Zheng, Z., Chen, S., Sun, W., and Sun, Z. “Continuous momentum management for space station based on LESO”. In: *Aerospace Science and Technology* 72 (Jan. 2018), pp. 364–370. DOI: 10.1016/j.ast.2017.11.022. URL: https://www.sciencedirect.com/science/article/pii/S1270963817320850.

[23] Liu, P., Chen, S., Xue, W., and Li, W. “On Hierarchical Compensation Based Active Disturbance Rejection Control for ACMM Problem of Spacecraft”. In: *Journal of Systems Science and Complexity* 36.4 (Aug. 2023), pp. 1480–1497. DOI: 10.1007/s11424-023-1399-2. URL: https://doi.org/10.1007/s11424-023-1399-2.

[24] Choi, M., and Flashner, H. “Neural-network-based spacecraft attitude control and momentum management”. In: *AIAA Guidance, Navigation, and Control Conference and Exhibit*. American Institute of Aeronautics and Astronautics, 2000. DOI: 10.2514/6.2000-4455. URL: https://arc.aiaa.org/doi/abs/10.2514/6.2000-4455.

[25] Strang, G. *Introduction to Linear Algebra*. 5th. Wellesley–Cambridge Press, 2016. Chap. 6.

[26] Zames, G. “Feedback and Optimal Sensitivity: Model Reference Transformations, Multiplicative Seminorms, and Approximate Inverses”. In: *IEEE Transactions on Automatic Control* 26.2 (1981), pp. 301–320. DOI: 10.1109/TAC.1981.1102566.

[27] Doyle, J., Glover, K., Khargonekar, P., and Francis, B. “State-Space Solutions to Standard H_2 and H_∞ Control Problems”. In: *IEEE Transactions on Automatic Control* 34.8 (1989), pp. 831–847. DOI: 10.1109/9.29425.

[28] Skogestad, S., and Postlethwaite, I. “Multivariable Feedback Control”. In: John Wiley and Sons, Ltd., 2005. Chap. 1,2,3,9.

[29] Seiler, P., Packard, A., and Gahinet, P. “An Introduction to Disk Margins [Lecture Notes]”. In: *IEEE Control Systems* 40.5 (Oct. 2020), pp. 78–95. DOI: 10.1109/mcs.2020.3005277.

A

Project Plan

The following Gannt chart summarizes the planning of the work conducted during the thesis as mentioned in Chapter 4. The chart outlines the main work packages of the project, from the literature review and assessment of the feasibility of different control strategies for Starlab to the aerodynamic model identification, $\mathcal{H}_\infty$ control design, and final evaluation. It gives a clear time frame for completion of the proposed research activities while giving their relative duration.

Task Name:		Literature Study					Research Phase I													Research Phase II																	Finalization Phase			
	Project Week Number:	1	2	3	4	5	6	7	8	9	10	11	12	13	14	15	16	17	18	19	20	21	22	23	24	25	26	27	28	29	30	31	32	33	34	35	36	37	38	39
	Month:	March					April				May				June						July			August				September					October				November			
	Day of the Month:	3	10	17	24	31	7	14	21	28	5	12	19	26	2	9	16	23	30	7	14	21	28	4	11	18	25	1	8	15	22	29	6	13	20	27	3	10	17	24
Literature Review	1. Topic Definition	☑	☐	☐	☐	☐	☐	☐	☐	☐	☐	☐	☐	☐	☐	☐	☐	☐	☐	Mid-term Review	☐	☐	☐	☐	☐	☐	☐	☐	☐	☐	☐	☐	☐	☐	☐	Green Light Review	☐	☐	☐	End of Thesis Project
	2. Spacecraft Dynamics and Kinematics	☑	☑	☑	☐	☐	☐	☐	☐	☐	☐	☐	☐	☐	☐	☐	☐	☐	☐		☐	☐	☐	☐	☐	☐	☐	☐	☐	☐	☐	☐	☐	☐	☐		☐	☐	☐	
	3. Literature Study on the ACMM Problem for Space Stations	☑	☑	☑	☑	☑	☐	☐	☐	☐	☐	☐	☐	☐	☐	☐	☐	☐	☐		☐	☐	☐	☐	☐	☐	☐	☐	☐	☐	☐	☐	☐	☐	☐		☐	☐	☐	
	4. Review of ESO + RLS + LQR (Hierarchical ADRC)	☐	☐	☐	☑	☑	☑	☐	☐	☐	☐	☐	☐	☐	☐	☐	☐	☐	☐		☐	☐	☐	☐	☐	☐	☐	☐	☐	☐	☐	☐	☐	☐	☐		☐	☐	☐	
	5. Review of Neural Network–based Control	☐	☐	☐	☑	☑	☑	☐	☐	☐	☐	☐	☐	☐	☐	☐	☐	☐	☐		☐	☐	☐	☐	☐	☐	☐	☐	☐	☐	☐	☐	☐	☐	☐		☐	☐	☐	
	6. Writing of Literature Review Report	☐	☐	☐	☐	☑	☑	☐	☐	☐	☐	☐	☐	☐	☐	☐	☐	☐	☐		☐	☐	☐	☐	☐	☐	☐	☐	☐	☐	☐	☐	☐	☐	☐		☐	☐	☐	
	7. Research Proposal Submission & Feedback Integration	☐	☐	☐	☐	☐	☑	☐	☐	☐	☐	☐	☐	☐	☐	☐	☐	☐	☐		☐	☐	☐	☐	☐	☐	☐	☐	☐	☐	☐	☐	☐	☐	☐		☐	☐	☐	
Analysis of State-of-the-art Control Strategies	1. Study of the ISS ACMM Strategy (Harduvel 1992)	☐	☐	☐	☐	☐	☐	☑	☑	☐	☐	☐	☐	☐	☐	☐	☐	☐	☐		☐	☐	☐	☐	☐	☐	☐	☐	☐	☐	☐	☐	☐	☐	☐		☐	☐	☐	
	2. Implementation and Evaluation of Observer-based Control	☐	☐	☐	☐	☐	☐	☑	☑	☑	☑	☑	☐	☐	☐	☐	☐	☐	☐		☐	☐	☐	☐	☐	☐	☐	☐	☐	☐	☐	☐	☐	☐	☐		☐	☐	☐	
	3. Preliminary Investigation of Learning-based Control Approaches	☐	☐	☐	☐	☐	☐	☐	☐	☐	☑	☑	☐	☐	☐	☐	☐	☐	☐		☐	☐	☐	☐	☐	☐	☐	☐	☐	☐	☐	☐	☐	☐	☐		☐	☐	☐	
	4. Comparative Assessment of Strengths and Limitations	☐	☐	☐	☐	☐	☐	☐	☐	☐	☑	☑	☑	☑	☐	☐	☐	☐	☐		☐	☐	☐	☐	☐	☐	☐	☐	☐	☐	☐	☐	☐	☐	☐		☐	☐	☐	
	5. Identification of Requirements for the Chosen Control Framework	☐	☐	☐	☐	☐	☐	☐	☐	☐	☑	☑	☑	☑	☐	☐	☐	☐	☐		☐	☐	☐	☐	☐	☐	☐	☐	☐	☐	☐	☐	☐	☐	☐		☐	☐	☐	
Aerodynamic Torque Modeling and System Identification	1. Definition of Aerodynamic Torque Model	☐	☐	☐	☐	☐	☐	☐	☐	☐	☑	☑	☑	☑	☐	☐	☐	☐	☐		☐	☐	☐	☐	☐	☐	☐	☐	☐	☐	☐	☐	☐	☐	☐		☐	☐	☐	
	2. Data Generation and Preprocessing	☐	☐	☐	☐	☐	☐	☐	☐	☐	☐	☐	☐	☑	☑	☑	☑	☑	☑		☑	☑	☑	☑	☐	☐	☐	☐	☐	☐	☐	☐	☐	☐	☐		☐	☐	☐	
	3. Parameter Estimation of Aerodynamic Coefficients	☐	☐	☐	☐	☐	☐	☐	☐	☐	☐	☐	☐	☑	☑	☑	☑	☑	☑		☑	☑	☑	☑	☐	☐	☐	☐	☐	☐	☐	☐	☐	☐	☐		☐	☐	☐	
	4. Validation and Refinement of the Model for Control Synthesis	☐	☐	☐	☐	☐	☐	☐	☐	☐	☐	☐	☐	☑	☑	☑	☑	☑	☑		☑	☑	☑	☑	☐	☐	☐	☐	☐	☐	☐	☐	☐	☐	☐		☐	☐	☐	
	5. Reporting	☐	☐	☐	☐	☐	☐	☐	☐	☐	☐	☐	☐	☐	☐	☐	☐	☑	☑		☐	☐	☐	☐	☐	☐	☐	☐	☐	☐	☐	☐	☐	☐	☐		☐	☐	☐	
H_∞ Control Formulation and Design	1. Definition of Control Objectives in the Frequency Domain	☐	☐	☐	☐	☐	☐	☐	☐	☐	☐	☐	☐	☐	☐	☐	☐	☐	☐		☐	☐	☑	☑	☐	☐	☐	☐	☐	☐	☐	☐	☐	☐	☐		☐	☐	☐	
	2. Formulation of the Mixed-Sensitivity Problem	☐	☐	☐	☐	☐	☐	☐	☐	☐	☐	☐	☐	☐	☐	☐	☐	☐	☐		☐	☐	☐	☑	☑	☑	☑	☑	☑	☑	☑	☑	☐	☐	☐		☐	☐	☐	
	3. Weighting Filter Design and Tuning	☐	☐	☐	☐	☐	☐	☐	☐	☐	☐	☐	☐	☐	☐	☐	☐	☐	☐		☐	☐	☐	☑	☑	☑	☑	☑	☑	☑	☑	☑	☐	☐	☐		☐	☐	☐	
	4. H∞ Controller Synthesis and Performance Evaluation	☐	☐	☐	☐	☐	☐	☐	☐	☐	☐	☐	☐	☐	☐	☐	☐	☐	☐		☐	☐	☐	☐	☐	☐	☑	☑	☑	☑	☑	☑	☐	☐	☐		☐	☐	☐	
	5. Analysis of Controller Robustness, and Trade-offs	☐	☐	☐	☐	☐	☐	☐	☐	☐	☐	☐	☐	☐	☐	☐	☐	☐	☐		☐	☐	☐	☐	☐	☐	☐	☑	☑	☑	☑	☑	☐	☐	☐		☐	☐	☐	
Evaluation and Results	1. Definition of Evaluation Scenarios and Metrics	☐	☐	☐	☐	☐	☐	☐	☐	☐	☐	☐	☐	☐	☐	☐	☐	☐	☐		☐	☐	☐	☐	☐	☐	☐	☐	☐	☐	☑	☑	☑	☐	☐		☐	☐	☐	
	2. Execution of Test Campaign	☐	☐	☐	☐	☐	☐	☐	☐	☐	☐	☐	☐	☐	☐	☐	☐	☐	☐		☐	☐	☐	☐	☐	☐	☐	☐	☐	☐	☐	☑	☑	☐	☐		☐	☐	☐	
	3. Accuracy, Robustness, and Stability Evaluation	☐	☐	☐	☐	☐	☐	☐	☐	☐	☐	☐	☐	☐	☐	☐	☐	☐	☐		☐	☐	☐	☐	☐	☐	☐	☐	☐	☐	☐	☑	☑	☐	☐		☐	☐	☐	
	4. Interpretation of Results	☐	☐	☐	☐	☐	☐	☐	☐	☐	☐	☐	☐	☐	☐	☐	☐	☐	☐		☐	☐	☐	☐	☐	☐	☐	☐	☐	☐	☐	☑	☑	☐	☐		☐	☐	☐	
	5. Reporting: Drafting of Results and Discussion Chapter	☐	☐	☐	☐	☐	☐	☐	☐	☐	☐	☐	☐	☐	☐	☐	☐	☐	☐		☐	☐	☐	☐	☐	☐	☐	☐	☐	☐	☐	☑	☑	☐	☐		☐	☐	☐	
Final Report and Thesis Writing	1. Integration of All Chapters	☐	☐	☐	☐	☐	☐	☐	☐	☐	☐	☐	☐	☐	☐	☐	☐	☐	☐		☐	☐	☐	☐	☐	☐	☐	☐	☐	☐	☐	☐	☐	☑	☐		☐	☐	☐	
	2. Review and Editing	☐	☐	☐	☐	☐	☐	☐	☐	☐	☐	☐	☐	☐	☐	☐	☐	☐	☐		☐	☐	☐	☐	☐	☐	☐	☐	☐	☐	☐	☐	☐	☑	☐		☑	☑	☑	
	3. Formatting and Compliance Checks	☐	☐	☐	☐	☐	☐	☐	☐	☐	☐	☐	☐	☐	☐	☐	☐	☐	☐		☐	☐	☐	☐	☐	☐	☐	☐	☐	☐	☐	☐	☐	☐	☐		☑	☑	☑	
	4. Final Submission	☐	☐	☐	☐	☐	☐	☐	☐	☐	☐	☐	☐	☐	☐	☐	☐	☐	☐		☐	☐	☐	☐	☐	☐	☐	☐	☐	☐	☐	☐	☐	☐	☐		☐	☐	☑	
	5. Presentation Preparation	☐	☐	☐	☐	☐	☐	☐	☐	☐	☐	☐	☐	☐	☐	☐	☐	☐	☐		☐	☐	☐	☐	☐	☐	☐	☐	☐	☐	☐	☐	☐	☐	☐		☑	☑	☑	
		6 weeks					13 weeks														16 weeks															4 weeks			

Holidays:

- 18th, 21st of April 2025
- 1st, 2nd, 29th, 30th of May 2025
- 9th, 19th, 20th of June 2025
- 3rd of October 2025